Surface Photovoltage Studies on Gallium Phosphide and Carbon Nitride for Photoelectrochemical and Photocatalytic Solar Energy Conversion

By

KATHLEEN BECKER
DISSERTATION

Submitted in partial satisfaction of the requirements for the degree of

DOCTOR OF PHILOSOPHY

in

CHEMISTRY

in the

OFFICE OF GRADUATE STUDIES

of the

UNIVERSITY OF CALIFORNIA

DAVIS

Approved:

Frank E. Osterloh, Chair

Susan M. Kauzlarich

Jesús M. Velázquez

Committee in Charge

2024

Acknowledgments

The research contained within this dissertation was supported by the U.S. Department of Energy, Office of Science, Basic Energy Sciences under grant number DE-SC0015329.

First and foremost, I would like to express my deepest gratitude to my research group. Professor Frank Osterloh for his guidance and encouragement during my time at UC Davis. I am grateful for the experience that I gained because I was in his lab. To all of my lab mates, past and present. I especially would like to thank Dr. Samutr Assavachin, Anna Kundmann, Chengcan Xiao, and Dr. Sahar Daemi for their helpful discussion, beneficial collaboration, and support on our coauthored works. I am also grateful to our research collaborators at Ben Gurion University in Israel for preparing the carbon nitride films investigated in Chapter 4. I would also like to thank Professor Susan Kauzlarich and Professor Jesús Velázquez for their helpful advice during my PhD studies and for their services in my dissertation committee. My acknowledgments would not be complete without thanking all of my friends and mentors at UC Davis. Special thanks to Dr. Bryan Enderle, Dr. Laci Gerhart, Dr. Sarah Lievens, Dr. Eddie Kim, Dr. Hannah Soukey, Nathan Yoshino, Dr. Rachel Doughty, Dr. Daniel Gruber, and Meghan Becker for encouraging and guiding me in the classroom.

I would like to thank my family for supporting me in my decision to move across the country to continue my education. The occasional visits and frequent video calls made it feel like I wasn't so far away. Finally, my husband, Brandon Harris, and our beautiful dogs, without your love and support to come home to each day, I could not have done it.

Surface Photovoltage Studies on Gallium Phosphide and Carbon Nitride for Photoelectrochemical and Photocatalytic Solar Energy Conversion

Abstract

Solar energy conversion offers a carbon free and renewable alternative to fossil fuel consumption. Current materials still fall short of the target solar-to-hydrogen efficiency needed to make the technology economically viable. In order to increase the efficiencies, a deeper understanding of charge generation, transfer and recombination, to further improve their photocatalytic activities. Within this dissertation n-type gallium phosphide is investigated for photocatalytic hydrogen production. P-type gallium phosphide and carbon nitride are investigated for photoelectrochemical solar energy conversion. Characterization of these materials consists of surface photovoltage spectroscopy, optical spectroscopy, electron microscopy, X-ray diffraction, and X-ray photoelectron spectroscopy.

Chapter 1 provides an introduction to the topic and important measurements. Chapter 2 investigates n-type gallium phosphide as a photocatalyst for hydrogen production, looking at defect states, space charge layer effects on the charge generation, cocatalyst effect on charge transfer and recombination processes to optimize activity for solar water splitting. A quantum efficiency of 14.8 % was achieved by 4 % (w/w) dinickel phosphide nanoparticles loaded onto gallium phosphide microparticles in an aqueous solution of 0.3 M sodium sulfide and 0.3 M sodium sulfite under 525 nm LED illumination. Chapter 3 reveals how the photovoltage and

photocurrent of p-type gallium phosphide photoelectrodes is affected by a cadmium sulfide passivation layer, added platinum cocatalyst, altered electrolyte composition, and added hydrogen or oxygen. The champion photocathode drives hydrogen evolution with a quantum efficiency of 62 % at 0.0 V RHE and an open circuit photovoltage of 0.43 V at 250 mW/cm^2 (400 nm). Finally, Chapter 4 explores the photovoltage of carbon nitride films prepared using different fabrication techniques and in different electrolytes. The best performance was achieved by a photoanode prepared via doctor blading in 0.1 M KOH with O_2 purging. This film reached 200 μA/cm^2 photocurrent at 1.23 V vs RHE and 1 sun illumination and a photovoltage of 1.1 V under 79 mW/cm^2 illumination (405 nm).

Table of Contents

List of Abbreviations

3.5CE	3.5 M calomel electrode
AQE	apparent quantum efficiency
CN	carbon nitride
CPD	contact potential difference
e^-	electron
EDX	energy dispersive X-ray spectroscopy
E_F	Fermi energy
$E_{F,n}$	quasi-Fermi energy of electrons
$E_{F,p}$	quasi-Fermi energy of holes
E_g	bandgap energy
GO	graphene oxide
h^+	hole
HER	hydrogen evolution reaction
IPCE	incident photon to current efficiency
n-GaP	n-type gallium phosphide
NHE	normal hydrogen electrode
OCP	open circuit potential
OER	oxygen evolution reaction
OWS	overall water splitting
PEC	photoelectrochemical

p-GaP	p-type gallium phosphide
QE	quantum efficiency
QFLS	quasi-Fermi lever splitting
rGO	reduced graphene oxide
SCR	space charge region
SEM	scanning electron microscopy
SPV	surface photovoltage
STH	solar-to-hydrogen
TEM	transmission electron microscopy
TEOA	triethanolamine
UV	ultraviolet
V_{bi}	built-in potential
V_{ph}	photovoltage
XPS	X-ray photoelectron spectroscopy
XRD	X-ray diffraction

Chapter 1 - Introduction

1.1 Solar Energy Conversion

As population growth worldwide and economic growth in developing countries increase, energy consumption across the globe will continue to rise. By 2050, 27 TW of energy is needed to meet the predicted demand.[1,2] The continued reliance on fossil fuels has led to an increase in CO_2 concentration in the atmosphere with 425 ppm monthly average reported at Mauna Loa Observatory in March of 2024. CO_2 traps heat leading to an increase in global temperature, ocean acidification, sea-level rise, and extreme weather events.[3–8] Global leaders have recognized the need for change; to meet the Paris Agreement, an aggressive transition to renewable energy is needed immediately. The Sun provides the Earth's surface with enough energy in just one hour to meet a year's worth of energy demand.[9] Despite the conversion efficiency of commercial monocrystalline silicon photovoltaic (PV) panels reaching above 22% and multi-junction cells reaching 47.6%, PV devices alone cannot meet global energy demand.[10] Peak energy demand and solar energy production times do not align and battery storage technology lags behind in terms of capacity, scaling, and cost.[11] Solar water splitting through electrolysis with PV devices or direct splitting via catalysis emerge as an efficient and cost effective way to produce green hydrogen fuel.

1.2 Overall Water Splitting

One of the biggest challenge facing scientists today, is how to efficiently harvest and store solar energy in order to break the reliance on fossil fuels that generate harmful CO_2.[12] A promising way to achieve solar energy conversion in a cost-effective way is overall water splitting (OWS), in

which solar energy is stored as chemical energy, in the bond rearrangement of water, as shown in Eq. 1.1. Hydrogen fuel has a large energy density by mass of 143 MJ/kg , which is comparable to conventional fossil fuels and significantly higher than batteries.[13] When energy is needed, it can be mixed with natural gas at existing power plants (Eq. 1.2) or used in a hydrogen fuel cell. Industrial application of green hydrogen includes, large scale transportation, oil refining, ammonia synthesis, and methanol production.[14] OWS using visible light activated catalysts has potential for large scale hydrogen fuel production and has the potential to utilize up to 35% of the energy reaching the device.[15–18]

$$\mathrm{H_2O\ (l)} \xrightarrow{\mathrm{h\nu}} \mathrm{H_2\ (g)} + \frac{1}{2}\ \mathrm{O_2\ (g)} \qquad \Delta G° = +237\ \mathrm{kJ/mol} \qquad \text{(Equation 1.1)}$$

$$\mathrm{H_2\ (g)} + \frac{1}{2}\ \mathrm{O_2\ (g)} \xrightarrow{\Delta} \mathrm{H_2O\ (l)} \qquad \Delta G° = -237\ \mathrm{kJ/mol} \qquad \text{(Equation 1.2)}$$

Under super-band gap illumination, a semiconductor will produce an electron/hole pair as shown in Eq. 1.3. From there, the photogenerated charge carriers can recombine or go on to do reduction or oxidation reactions. Two electrons are required to accomplish the proton reduction reaction (Eq. 1.4), whereas four holes are required for the water oxidation reaction (Eq. 1.5). H_2 and O_2 generation can be studied using photoelectrochemical (PEC) measurements and gas chromatography (GC). The generation and movement of charge carriers cand be analysed using surface photovoltage (SPV).

$$h\nu \rightarrow \mathrm{h^+ + e^-} \qquad \text{(Equation 1.3)}$$

$$\mathrm{2H^+ + 2e^- \rightarrow H_2} \qquad \text{(Equation 1.4)}$$

$$\mathrm{2H_2O \rightarrow O_2 + 4H^+ + 4e^-} \qquad \text{(Equation 1.5)}$$

OWS from a photocatalyst was first reported in 1972 by Fujishima and Honda using a TiO_2 light absorber and OER catalyst and a Pt HER catalyst.[19] In addition to TiO_2 (E_g = 3.2 eV), $SrTiO_3$ (E_g = 3.4 eV), SiC (E_g < 3.3 eV), and $NaTaO_3$ (E_g > 2.4 eV) among others are capable of OWS.[20–22] The largest downside of single absorber materials is the requirement of UV light input since it is only 6% of the solar spectrum. In Fig. 1.1a, an illustration of a wide band gap semiconductor is shown, where the valence band is more oxidizing than the oxygen evolution reaction (OER) potential and the conduction band is more reducing than the hydrogen evolution reaction (HER) potential. In this case, four UV photons are able to produce four electron-hole pairs to do the redox chemistry. To enhance the process, an OER and/or HER cocatalyst can be anchored to the absorber to act as an active site for gas evolution.

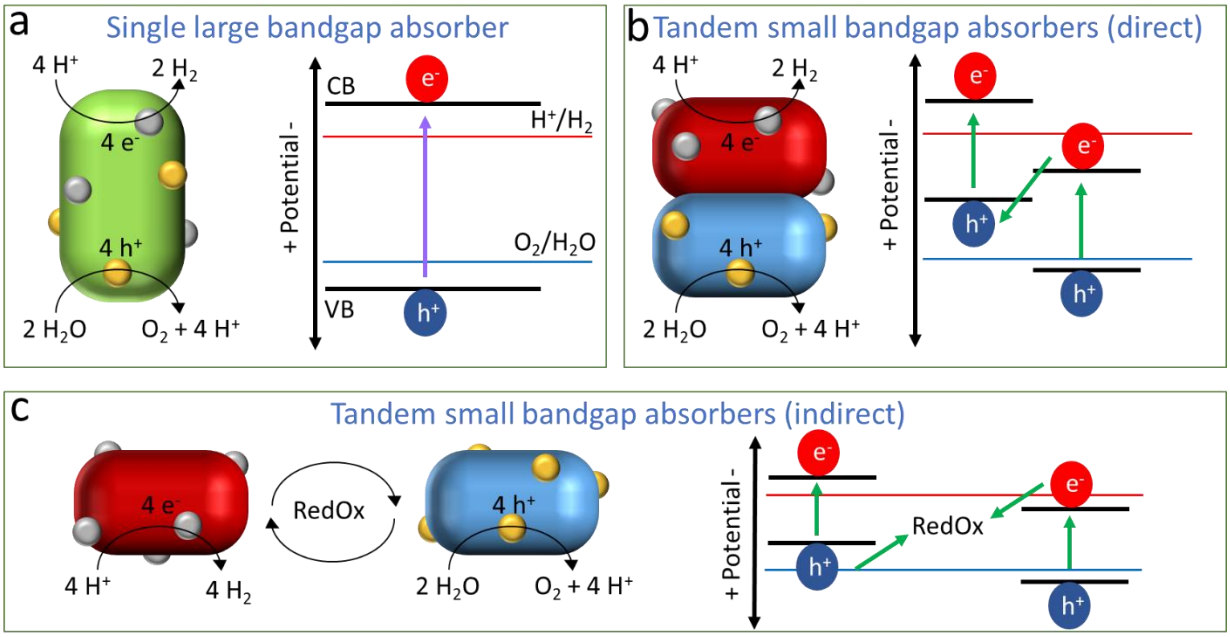

Figure 1.1 schematic of (a) wide band gap, (b) direct tandem, and (c) indirect tandem semiconductor absorbers with ability to oxidize water and reduce protons and generic band positions relative to the HER (red) and OER (blue) reactions.

In order to utilize more of the solar spectrum, semiconductors with smaller band gaps need to be used. Now, two materials are needed to satisfy both the OER and HER. In Fig. 1.1b, an illustration of a direct contact tandem photocatalysis system is shown. In this case, one absorber material is in red and acts as the HER photocatalyst, meanwhile, the OER is in blue. Because the photocatalysts are in direct contact, holes and electrons can move to maintain charge balance. These tandem systems are often called Z-scheme because of the movement of charge carriers between the semiconductors.[23] Martials that are used for the photoanode to facilitate the OER include bismuth vanadate (E_g = 2.4 eV), tungsten oxide (E_g = 3.1 eV), and hematite (E_g = 2.2 eV).[24–26] Materials that are used for the photocathode to facilitate the HER include cuprous oxide (E_g = 2.0 eV), $Cu(In_xGa_{1-x})Se_2$ ($1 < E_g < 1.7$ eV), and gallium phosphide (E_g = 2.2 eV).[27–29] A second option for tandem systems is to use an indirect contact method. Here a redox couple is used to shuttle the excess charge carriers to maintain charge balance rather than flowing directly between the materials. An illustration of this is shown in Fig 1.1c including a band diagram. Possible molecular redox shuttles include Fe^{3+}/Fe^{2+} or IO_3^-/I^-.[30]

The tandem absorbers can be thin films submerged in water or a particle suspension. Fig. 1.2a depicts two geometries where thin films can be oriented, in front of or next to each other. If one semiconductor has a larger band gap, it can be placed in front of the smaller band gap absorber so that the lower energy photons can pass through the front absorber and interact with the back. This geometry saves space while utilizing more of the solar spectrum. However, if the materials have similar band gaps, the back absorber will get few photons. In this case, the absorbers should be placed next to each other, however, this doubles the area needed for the device. A particle suspension (Fig. 1.1b) is advantageous because it requires less material and no

need for a substrate. In this case, the particles will randomly orient themselves in the solution. This causes a decrease in performance because the smaller band gap material can be in front casting shade on the larger band gap absorber. Lastly, Fig. 1.2c shows nanoparticles of the large band gap absorber anchored on microparticle of the smaller band gap absorber in direct contact.

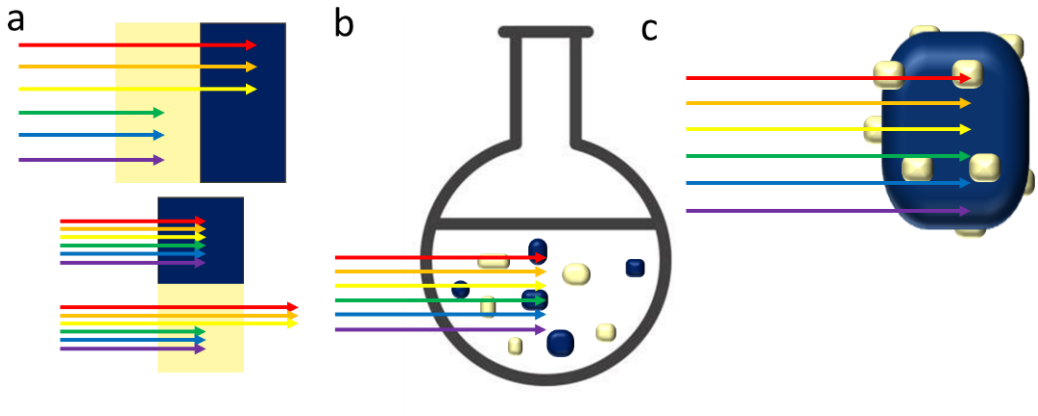

Figure 1.2 (a) Thin film configuration of dual absorbers, where yellow represents the larger band gap material and navy represents the smaller band gap material. (b) particle suspension indirect tandem absorbers with redox shuttle, and (c) nanoparticle anchored on microparticles or thin film direct tandem.[15]

Recombination of charge carriers remains one of the largest challenges for creating efficient OWS devices.[31] This occurs in the bulk or on the surface of semiconductors. These charge carriers are no longer available to drive redox reactions to produce O_2 and H_2.[32] To split water effectively, charges must be separated to increase their lifetimes and to drive the slow surface redox reactions.[33] Making modifications to surface cocatalysts and removing defect trap sites are crucial for this purpose.[33] An example is $SrTiO_3$, a well-known large band gap photocatalyst. Oxygen vacancies within $SrTiO_3$ generate free electrons, reducing Ti^{4+} and forming Ti^{3+} mid-band

gap states, which causes electron – hole recombination. [34] Aliovalent doping drastically enhances photocatalytic activity by suppressing these Ti^{3+} states.[20,35]

As mentioned previously, smaller band gaps will result in higher efficiency caused by the increase in available photons from the sun. In addition to the size of the band gap, in a tandem system the positions relative to each other is also important. Fig. 1.3 shows possible combinations of band alignments for two semiconductor absorbers. Type I and type III are not favourable for OWS. In the case of type I, both electrons and holes from absorber a can transfer to absorber b causing an increase in charge recombination. Additionally, if absorber a already fulfils the redox conditions for both OER and HER, absorber b is not needed. Type III, on the other hand, will not be able to maintain charge balance because the conduction band of absorber a is below the valence band of absorber b. Type II is the band alignment desired for tandem systems. In this case, absorber a has a conduction band more reducing and would be the HER catalyst whereas absorber b has a valence band that is more oxidizing and is the OER catalyst.

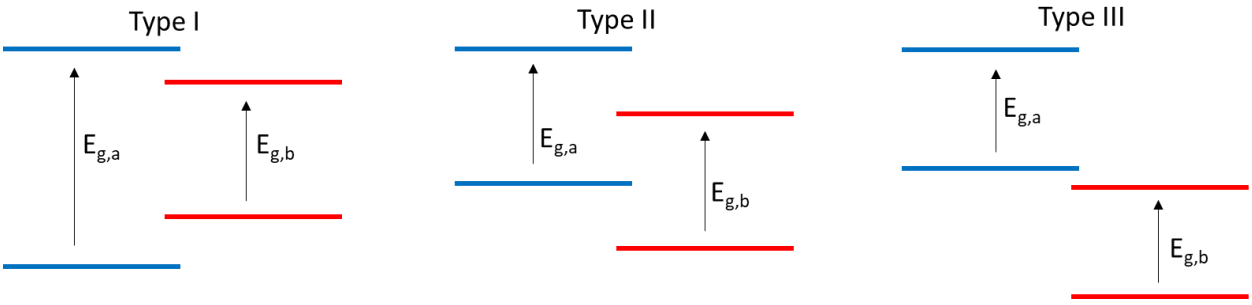

Figure 1.3 Band alignments for the three types of semiconductor heterojunctions.

When two semiconductors interface, electrons will flow until the Fermi levels reach an equilibrium, creating a p-n junction. In Fig. 1.4a the larger band gap absorber is in front of the smaller band gap absorber. In this case, the front absorber is an n-type semiconductor for HER,

and the bottom absorber is a p-type semiconductor for OER, creating a type II heterojunction. This allows good charge separation. Charge recombination is common at interfaces and is depicted using dashed arrows. When a semiconductor is submerged in solution, the flat band diagrams above will bend such that the Fermi levels of the absorbers match the redox potential of the solution. The downward band bending of a n-type/liquid interface is depicted in Fig. 1.4b. This promotes the OER as holes can reach the liquid, but electrons are repelled by the band bending.

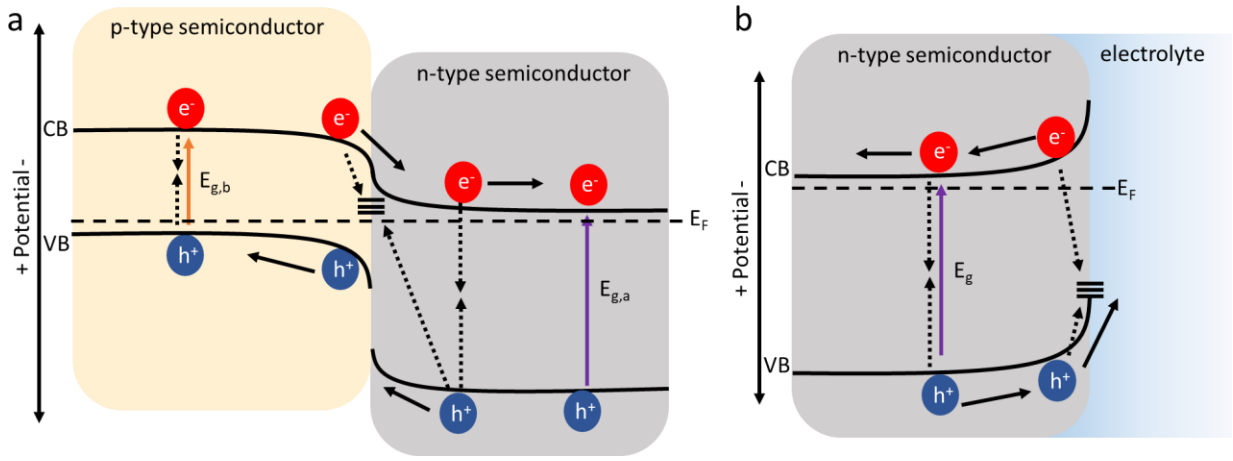

Figure 1.4 band diagrams of (a) p-n junction and (b) semiconductor-electrolyte interface showing band edges, Fermi levels, band bending, surface defects, excitation, charge transfer, and charge recombination.

1.3 Surface Photovoltage Spectroscopy (SPV)

In order to probe the photophysics of semiconductors, SPV is used. SPV signals originate from the separation of photogenerated charge carriers within a photoactive material.[36] When a material is excited with photons of energy greater than the material's band gap, a mobile

electron/hole pair is created that can drift and diffuse through the material. Charge generation, transport, transfer, and recombination are all mechanisms that can lead to an SPV signal.[37] Fig. 1.5a depicts the SPV scheme where the contact potential difference change (ΔCPD) of a sample on top of a conductive substrate is measured as a function of the incident photon energy using a gold Kelvin probe.[38] For a stand-alone semiconductor sample, the direction of the charge separation under illumination corresponds to the majority carrier type in the semiconductor.[39] Additional information can be obtained from the spectrum including the effective band gap, midgap and surface state energies, and depletion layer width.[36,40] An n-type semiconductor is shown in Fig. 1.5a, therefore a negative ΔCPD would be expected as electrons are injected into the FTO substrate for the particle film (blue curve in Fig. 1.5c). The SPV signal will peak when the light penetration depth $1/\alpha$ is the same size as the space charge region for the material or when the photon flux begins to decrease from the light source.

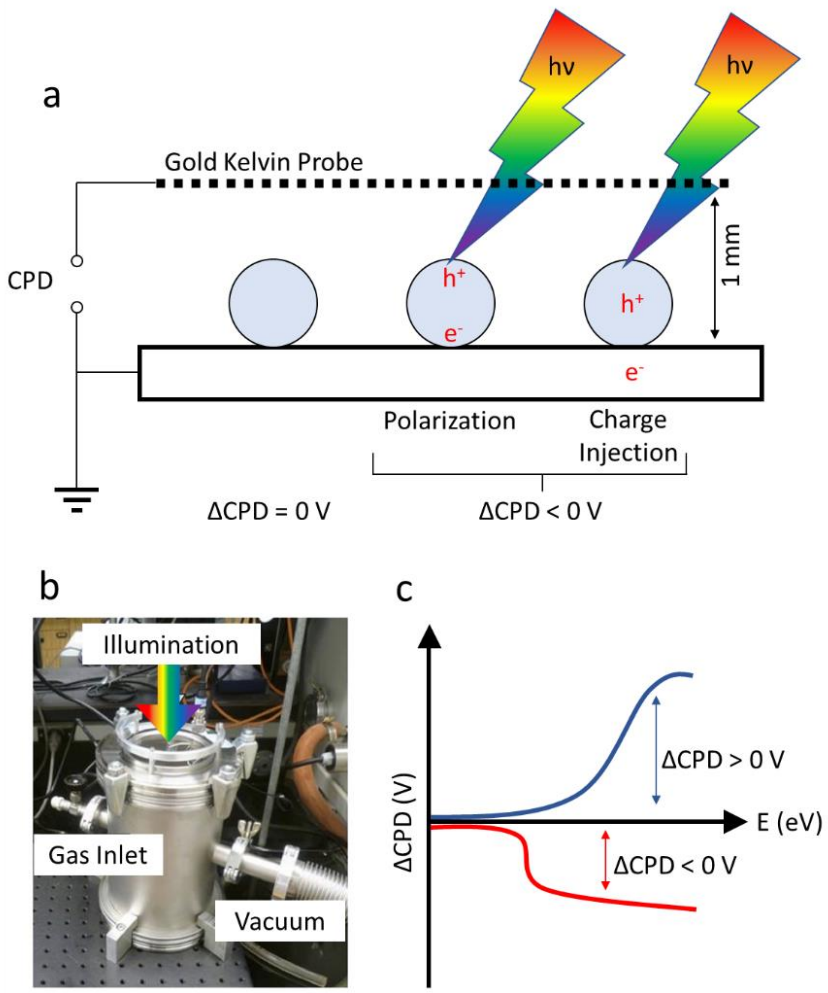

Figure 1.5 (a) Schematic of an n-type material SPV measurement and charge separation. Changes in CPD are generated by film polarization or majority charge carrier transferring to the substrate. (b) SPV chamber setup. (c) Example SPV spectra of a positive signal indicating a p-type semiconductor and a negative signal indicating a n-type semiconductor.

The energy scheme for the contact potential difference (CPD) measurement is shown in Fig. 1.6.[37] Once in electrical contact, the sample and reference equilibrate by the movement of electrons from the material with the more reducing work function (W) to the other material. An applied bias (V_b) can be used to undo the electrostatic potential.

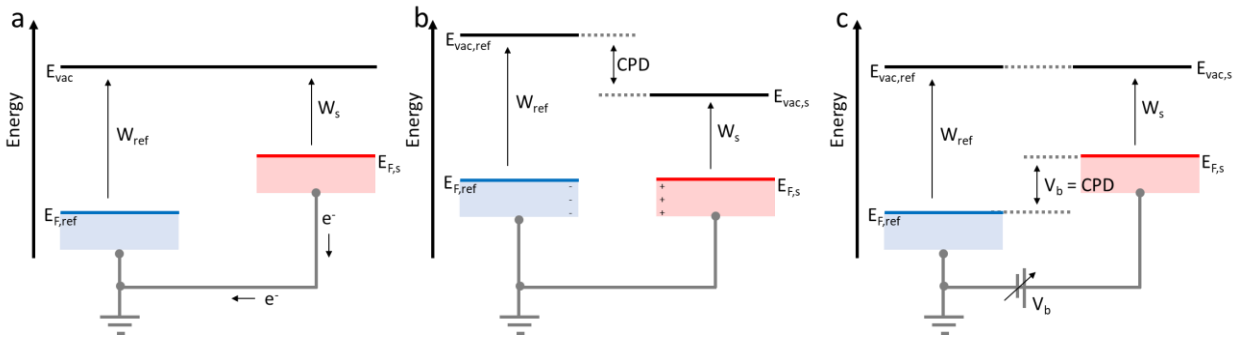

Figure 1.6 Schematic energy diagram of parallel plate capacitor formed by two different materials at (a) non-equilibrium when first contacting, (b) equilibrium reached, and (c) with an applied bias to offset the CPD. $E_{F,ref}$, W_{ref}, $E_{F,s}$, and W_s are the Fermi levels and work functions for the reference and sample materials respectively. The local vacuum potential is denoted as E_{vac} for both the reference and sample material. V_b is the required applied potential to offset the CPD between the two materials.[36]

Recently, our lab has been able to conduct *in situ* SPV measurements, where a small aliquot of electrolyte is placed on the surface of $BiVO_4$ and $CuGa_3Se_5$ films.[41,42] The measurement configuration is very similar to the above SPV configuration, except for the addition of the solution and a piece of microscope glass shown in Fig. 1.7. Because the semiconductor is in contact with the electrolyte, the SPV signal probes the semiconductor/liquid junction.[36,37] The Fermi level of the sample at the semiconductor/liquid interface changes due to the adaptive junction properties. Under illumination, polarization within the sample will cause a ΔCPD. Separation can be from majority carriers being injected into the substrate and/or minority carriers reacting with the electrolyte.

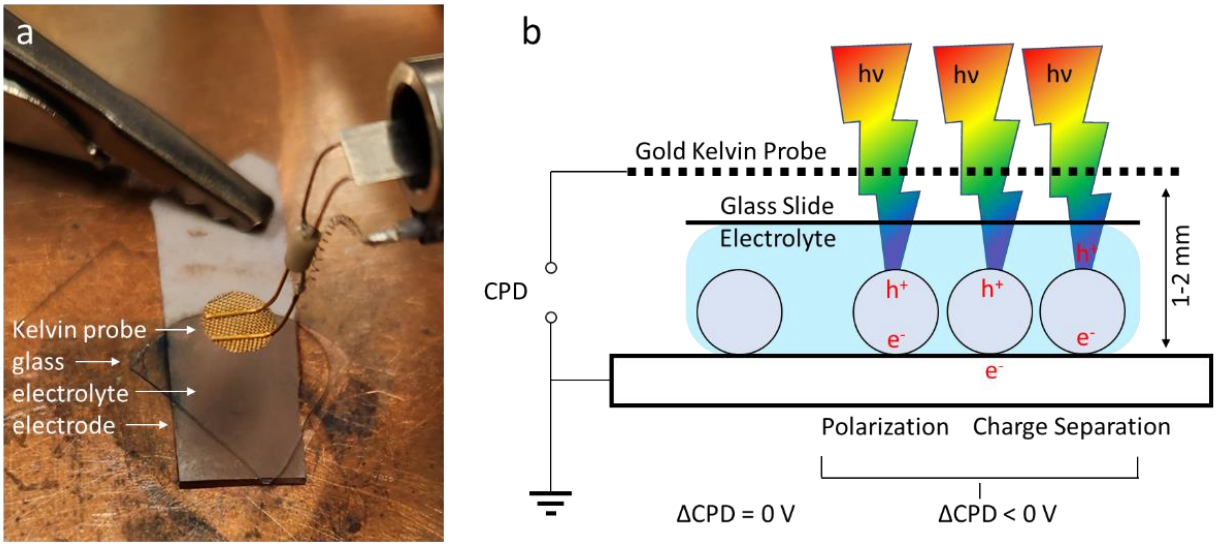

Figure 1.7 (a) Photo of GaP electrode configuration for liquid SPV measurements. (b) Schematic of liquid SPV measurement and charge separation. Changes in CPD are generated by film polarization or majority/minority charge carrier transferring to the substrate/electrolyte.

1.4 Relevant Calculations

From Fig. 1.6b, the CPD between two materials in electrical contact can be understood through Eq. 1.6, where W_{ref} and W_s are the work function of the reference material and sample, respectively, and q is the elementary charge, 1.602×10^{-19} C. Under super-band gap illumination, W_s will shift as photogenerated charge carriers are produced and separated resulting in a photovoltage as seen in Eq. 1.7. The ΔCPD upon illumination can then be calculated by combining Eq. 1.6 and 1.7 resulting in Eq. 1.8.

$$CPD = \frac{W_{ref} - W_s}{q} \qquad \text{(Equation 1.6)}$$

$$V_{ph} = \frac{W_{s,light} - W_{s,dark}}{q} \qquad \text{(Equation 1.7)}$$

$$V_{ph} = -\Delta CPD \qquad \text{(Equation 1.8)}$$

The quasi-Fermi level splitting (QFLS) is the maximum electric potential that the electrode can produce under illumination[36,43] (Eq. 1.9), but cannot be directly measured from liquid SPV measurements due to voltage loss at both the front and back contacts as shown in Fig. 1.8.[36,43,44] Rather, the SPV will have the two components SPV_b and SPV_f for the back and front contacts, respectively.[41] Each SPV component (SPV_b and SPV_f) is calculated similarly to the vacuum measurement in Eq. 1.7 and when combined result in the photovoltage as seen in Eq. 1.12. Because of the voltage loss, the V_{ph} from liquid SPV is always an underestimate of the QFLS energy of the device.

$$QFLS = E_{F,n} - E_{F,p} \qquad \text{(Equation 1.9)}$$

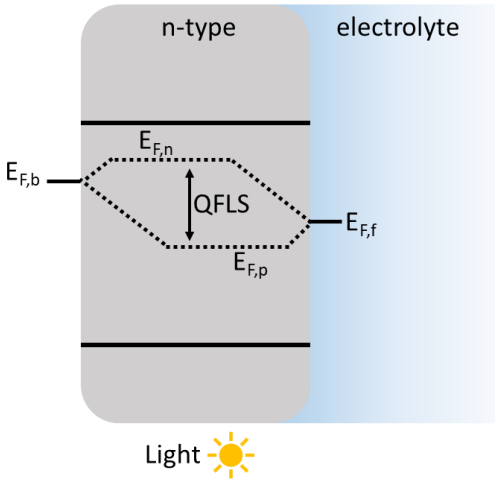

Figure 1.8 Band diagrams of n-type semiconductor-electrolyte interface under illumination showing QFLS energy and voltage loss at the front and back contacts. Where $E_{F,p}$ and $E_{F,n}$ are the quasi-Fermi levels of the holes and electrons, respectively. $E_{F,f}$ and $E_{F,b}$ represents the voltage measured at the front and back contacts, respectively.

$$SPV_b = -\left(CPD_{b,light} - CPD_{b,dark}\right) = -\left(\frac{E_{F,b}-E_F}{q}\right) \quad \text{(Equation 1.10)}$$

$$SPV_f = -\left(CPD_{f,light} - CPD_{f,dark}\right) = \frac{E_{F,f}-E_F}{q} \quad \text{(Equation 1.11)}$$

$$V_{ph} = SPV_b + SPV_f = \frac{E_{F,f}-E_{F,b}}{q} \quad \text{(Equation 1.12)}$$

Solar-to-hydrogen (STH) efficiency (η_{STH}) can be calculated using empirical PEC data and Eq. 1.13.[45] The operating voltage (J_{op}) between the two absorbing materials is measured. The Gibbs free energy ($\Delta G°_{H2O}$) of the reaction, faradaic efficiency (η_{farad}), elementary charge (q), and the power flux (E_s) of the sun are all constant. The equation can be simplified further into Eq. 1.14.[46] Theoretical maximum efficiency of dual absorber systems was calculated by Fountaine et al. The best-case scenario of 40% efficiency can be reached with band gaps of 0.52 eV and 1.40 eV for the two absorbers.[47] Using known high-performance materials, the maximum efficiency drops to 28.3% and using only earth abundant materials, 16.2% is the best theoretical efficiency.[47]

$$\eta_{STH} = \frac{J_{op}\Delta G^{\circ}_{H_2O}\eta_{farad}}{2qE_s} \quad \text{(Equation 1.13)}$$

$$\eta_{STH} = \frac{1.23(V)\times J_{op}(mA/cm^2)}{S\,(mW/cm^2)} \quad \text{(Equation 1.14)}$$

Another commonly used figure of merit for photocatalytic devices is the quantum efficiency (QE), which is a measure of the percentage of photons that result in an extracted electron/hole pair and can be calculated from PEC or GC measurements. There are several ways of counting the photons and charges. Apparent QE for the HER is defined by Eq. 1.15, where n_{H_2} is the amount of H_2 generated and ϕ_p is the number of incident photons. External QE, also called incident photon to current efficiency (IPCE), is used to characterize and understand materials

performance.[48] IPCE is an intuitive electrons out per photons in. Lastly, internal QE, or absorbed photon to current efficiency (APCE), considers how many of the incident photons are absorbed. This allows for losses from transmitted or reflected photons to be accounted for, and is typically used for thin film absorber materials.[48] EQE and IQE are important for optimizing performance; however, a high EQE/IQE does not always correspond to a high STH or AQE value.

$$\mathrm{AQE} = \frac{2n_{H_2}}{\phi_p} \qquad \text{(Equation 1.15)}$$

$$\mathrm{EQE} = \mathrm{IPCE} = \frac{n_{e^-}}{\phi_p} \qquad \text{(Equation 1.16)}$$

$$\mathrm{IQE} = \mathrm{APCE} = \frac{EQE}{\eta_{E_g}} \qquad \text{(Equation 1.17)}$$

1.5 Objective

The purpose of this work is to investigate the factors that control the activity of solar fuel photoelectrodes and photocatalysts through a combination of surface photovoltage spectroscopy, photoelectrochemical measurements, and photocatalytic gas evolution experiments. By integrating these methods, the study aims to elucidate the material properties, charge dynamics, and catalytic performance, ultimately contributing to the design of more efficient and sustainable solar energy conversion systems.

In Chapter 2, a particle suspension of n-type gallium phosphide (n-GaP) is investigated to learn about the optimization of HER. HER kinetics is dependent on the active site for catalysis.[49] This Goldilocks region is often depicted by a volcano plot where precious metals such as Pt, Ir, Rh sit at the top.[50] Finding alternative cocatalysts to replace these expensive metals is critical for low cost green H_2 production.[51] We also wonder why there are more n-type materials for HER when

p-type has the correct polarity to move electrons to the surface. This drives our investigation of the interplay between the SCR and the sacrificial electron donor in solution [52] The SCR within the semiconductor is important for efficient HER, as a larger SCR will be able to separate more e^-/h^+ pairs. As previously mentioned, the sacrificial electron donor in solution is hypothesized to control the Fermi level, another variable that can be manipulated. What are the states that lead to sub-band gap excitation and how do they affect efficiency? Which can be studied using SPV and XPS and once identified, determining how to remove these defects is another way to improve efficiency.

Looking now at p-type gallium phosphide (p-GaP), Chapter 3 investigates using surface photovoltage spectroscopy, open circuit potential measurements, and photoelectrochemical experiments to evaluate the kinetic and thermodynamic factors that control energy conversion for HER.[41] Questions center on how p-GaP can be stabilized in solution and whether internal photovoltage is a good metric for PEC performance. To probe the first question, a thin n-type cadmium sulfide (n-CdS) buffer layer and Pt cocatalyst were added. Then, *in situ* SPV measurements were taken to confirm internal photovoltage of the electrode and compared with the photovoltage values obtained from PEC and OCP measurements.

A collaboration on carbon nitride (CN) with the Shalom Lab at Ben-Gurion University of the Negev in Israel will be discussed in Chapter 4. CN is an n-type semiconductor that can be used for the OER. Similar to Chapter 3, we employ SPV measurements in combination with photoelectrochemical scans to characterize these films and identify the factors limiting their efficiency.[53] Specifically, we will use SPV to observe defects in CN, understand the effect of

sacrificial electron donors (TEAO) and acceptors (NaClO), and understand the effect of the electrolyte Fermi level on the ability of CN to form a semiconductor-liquid junction.

1.6 References

(1) Hisatomi, T.; Kubota, J.; Domen, K. Recent Advances in Semiconductors for Photocatalytic and Photoelectrochemical Water Splitting. *Chem. Soc. Rev.* **2014**, *43* (22), 7520–7535. https://doi.org/10.1039/c3cs60378d.

(2) Barber, J. Photosynthetic Energy Conversion: Natural and Artificial. *Chem. Soc. Rev.* **2009**, *38* (1), 185–196. https://doi.org/10.1039/b802262n.

(3) Watts, R. G. Climate Models and CO_2-Induced Climatic Changes. *Clim. Change* **1980**, *2* (4), 387–408. https://doi.org/10.1007/BF00137207.

(4) Voss, R.; Mikolajewicz, U. Long-Term Climate Changes Due to Increased CO_2 Concentration in the Coupled Atmosphere-Ocean General Circulation Model ECHAM3/LSG. *Clim. Dyn.* **2001**, *17* (1), 45–60. https://doi.org/10.1007/PL00007925.

(5) Kabir, M.; Habiba, U. E.; Khan, W.; Shah, A.; Rahim, S.; Rios-Escalante, P. R. D. los; Farooqi, Z. U. R.; Ali, L. Climate Change Due to Increasing Concentration of Carbon Dioxide and Its Impacts on Environment in 21st Century; a Mini Review. *J. King Saud Univ. - Sci.* **2023**, *35* (5), 102693. https://doi.org/10.1016/j.jksus.2023.102693.

(6) Melzner, F.; Mark, F. C.; Seibel, B. A.; Tomanek, L. Ocean Acidification and Coastal Marine Invertebrates: Tracking CO_2 Effects from Seawater to the Cell. *Ann. Rev. Mar. Sci.* **2020**, *12*, 499–523. https://doi.org/10.1146/annurev-marine-010419-010658.

(7) Ouyang, Z.; Qi, D.; Chen, L.; Takahashi, T.; Zhong, W.; DeGrandpre, M. D.; Chen, B.; Gao, Z.; Nishino, S.; Murata, A.; Sun, H.; Robbins, L. L.; Jin, M.; Cai, W. J. Sea-Ice Loss Amplifies Summertime Decadal CO_2 Increase in the Western Arctic Ocean. *Nat. Clim. Chang.* **2020**, *10* (7), 678–684. https://doi.org/10.1038/s41558-020-0784-2.

(8) Halofsky, J. E.; Peterson, D. L.; Harvey, B. J. Changing Wildfire, Changing Forests: The Effects of Climate Change on Fire Regimes and Vegetation in the Pacific Northwest, USA. *Fire Ecol.* **2020**, *16* (1). https://doi.org/10.1186/s42408-019-0062-8.

(9) Lewis, N. S.; Nocera, D. G. Powering the Planet: Chemical Challenges in Solar Energy Utilization. *Proc. Natl. Acad. Sci. U. S. A.* **2006**, *103* (43), 15729–15735. https://doi.org/10.1073/pnas.0603395103.

(10) NREL. Best Research-Cell Efficiencies. *Natl. Renew. Energy Lab.* **2024**.

(11) Kannan, N.; Vakeesan, D. Solar Energy for Future World: - A Review. *Renew. Sustain. Energy Rev.* **2016**, *62*, 1092–1105. https://doi.org/10.1016/j.rser.2016.05.022.

(12) Wang, Q.; Hisatomi, T.; Suzuki, Y.; Pan, Z.; Seo, J.; Katayama, M.; Minegishi, T.; Nishiyama, H.; Takata, T.; Seki, K.; Kudo, A.; Yamada, T.; Domen, K. Particulate Photocatalyst Sheets Based on Carbon Conductor Layer for Efficient Z-Scheme Pure-Water Splitting at Ambient Pressure. *J. Am. Chem. Soc.* **2017**, *139* (4), 1675–1683. https://doi.org/10.1021/jacs.6b12164.

(13) Cook, T. R.; Dogutan, D. K.; Reece, S. Y.; Surendranath, Y.; Teets, T. S.; Nocera, D. G. Solar Energy Supply and Storage for the Legacy and Nonlegacy Worlds. *Chem. Rev.* **2010**, *110*

(11), 6474–6502. https://doi.org/10.1021/cr100246c.

(14) Oliveira, A. M.; Beswick, R. R.; Yan, Y. A Green Hydrogen Economy for a Renewable Energy Society. *Curr. Opin. Chem. Eng.* **2021**, *33*, 100701. https://doi.org/10.1016/j.coche.2021.100701.

(15) Osterloh, F. E. Artificial Photosynthesis with Inorganic Particles. In *Intergrated Solar Fuel Generators*; The Royal Society of Chemistry, 2019; pp 214–280. https://doi.org/10.1039/9781788010313-00214.

(16) Fabian, D. M.; Hu, S.; Singh, N.; Houle, F. A.; Hisatomi, T.; Domen, K.; Osterloh, F. E.; Ardo, S. Particle Suspension Reactors and Materials for Solar-Driven Water Splitting. *Energy Environ. Sci.* **2015**, *8* (10), 2825–2850. https://doi.org/10.1039/c5ee01434d.

(17) Nielander, A. C.; Shaner, M. R.; Papadantonakis, K. M.; Francis, S. A.; Lewis, N. S. A Taxonomy for Solar Fuels Generators. *Energy Environ. Sci.* **2015**, *8* (1), 16–25. https://doi.org/10.1039/c4ee02251c.

(18) Herron, J. A.; Kim, J.; Upadhye, A. A.; Huber, G. W.; Maravelias, C. T. A General Framework for the Assessment of Solar Fuel Technologies. *Energy Environ. Sci.* **2015**, *8* (1), 126–157. https://doi.org/10.1039/c4ee01958j.

(19) Fujishima, A.; Honda, K. Electrochemical Photolysis of Water at a Semiconductor Electrode. *Nature* **1972**, *238* (5358), 37–38.

(20) Iwashina, K.; Kudo, A. Rh-Doped $SrTiO_3$ Photocatalyst Electrode Showing Cathodic Photocurrent for Water Splitting under Visible-Light Irradiation. *J. Am. Chem. Soc.* **2011**,

133 (34), 13272–13275. https://doi.org/10.1021/ja2050315.

(21) Akikusa, J.; Khan, S. U. M. Photoelectrolysis of Water to Hydrogen in P-SiC/Pt and p-SiC/n-TiO_2 Cells. *Int. J. Hydrogen Energy* **2002**, *27* (9), 863–870. https://doi.org/10.1016/S0360-3199(01)00191-4.

(22) Iwase, A.; Kato, H.; Kudo, A. The Effect of Au Cocatalyst Loaded on La-Doped $NaTaO_3$ on Photocatalytic Water Splitting and O_2 Photoreduction. *Appl. Catal. B Environ.* **2013**, *136–137*, 89–93. https://doi.org/10.1016/j.apcatb.2013.02.006.

(23) Wang, Q.; Hisatomi, T.; Katayama, M.; Takata, T.; Minegishi, T.; Kudo, A.; Yamada, T.; Domen, K. Particulate Photocatalyst Sheets for Z-Scheme Water Splitting: Advantages over Powder Suspension and Photoelectrochemical Systems and Future Challenges. *Faraday Discuss.* **2017**, *197*, 491–504. https://doi.org/10.1039/c6fd00184j.

(24) Guijarro, N.; Prévot, M. S.; Yu, X.; Jeanbourquin, X. A.; Bornoz, P.; Bourée, W.; Johnson, M.; Le Formal, F.; Sivula, K. A Bottom-Up Approach toward All-Solution-Processed High-Efficiency Cu(In,Ga)S_2 Photocathodes for Solar Water Splitting. *Adv. Energy Mater.* **2016**, *6* (7), 1–13. https://doi.org/10.1002/aenm.201501949.

(25) Santato, C.; Ulmann, M.; Àugustynski, J. Photoelectrochemical Properties of Nanostructured Tungsten Trioxide Films. *J. Phys. Chem. B* **2001**, *105* (5), 936–940. https://doi.org/10.1021/jp002232q.

(26) Townsend, T. K.; Sabio, E. M.; Browning, N. D.; Osterloh, F. E. Photocatalytic Water Oxidation with Suspended Alpha-Fe_2O_3 Particles-Effects of Nanoscaling. *Energy Environ.*

Sci. **2011**, *4* (10), 4270–4275. https://doi.org/10.1039/c1ee02110a.

(27) Maijenburg, A. W.; Zoontjes, M. G. C.; Mul, G. Insight into the Origin of the Limited Activity and Stability of P-Cu_2O Films in Photoelectrochemical Proton Reduction. *Electrochim. Acta* **2017**, *245*, 259–267. https://doi.org/10.1016/j.electacta.2017.05.114.

(28) Kumagai, H.; Minegishi, T.; Sato, N.; Yamada, T.; Kubota, J.; Domen, K. Efficient Solar Hydrogen Production from Neutral Electrolytes Using Surface-Modified Cu(In,Ga)Se_2 Photocathodes. *J. Mater. Chem. A* **2015**, *3* (16), 8300–8307. https://doi.org/10.1039/c5ta01058f.

(29) Standing, A.; Assali, S.; Gao, L.; Verheijen, M. A.; Van Dam, D.; Cui, Y.; Notten, P. H. L.; Haverkort, J. E. M.; Bakkers, E. P. A. M. Efficient Water Reduction with Gallium Phosphide Nanowires. *Nat. Commun.* **2015**, *6* (May), 1–7. https://doi.org/10.1038/ncomms8824.

(30) Ng, B. J.; Putri, L. K.; Kong, X. Y.; Teh, Y. W.; Pasbakhsh, P.; Chai, S. P. Z-Scheme Photocatalytic Systems for Solar Water Splitting. *Adv. Sci.* **2020**, *7* (7). https://doi.org/10.1002/advs.201903171.

(31) Takata, T.; Jiang, J.; Sakata, Y.; Nakabayashi, M.; Shibata, N.; Nandal, V.; Seki, K.; Hisatomi, T.; Domen, K. Photocatalytic Water Splitting with a Quantum Efficiency of Almost Unity. *Nature* **2020**, *581* (7809), 411–414. https://doi.org/10.1038/s41586-020-2278-9.

(32) Maeda, K.Z., Scheme Water Splitting Using Two Different Semiconductor Photocatalysts. **2013**, *2*. https://doi.org/10.1021/cs4002089

(33) Hisatomi, T.; Kubota, J.; Domen, K. Recent Advances in Semiconductors for Photocatalytic and Photoelectrochemical Water Splitting. *Chem. Soc. Rev.* **2014**, *43* (22), 7520–7535. https://doi.org/10.1039/c3cs60378d.

(34) Ma, X.; Wu, Z.; Roberts, E. J.; Han, R.; Rao, G.; Zhao, Z.; Lamoth, M.; Cui, X.; Britt, R. D.; Osterloh, F. E. Surface Photovoltage Spectroscopy Observes Sub-Band-Gap Defects in Hydrothermally Synthesized $SrTiO_3$ Nanocrystals. *J. Phys. Chem. C* **2019**, *123* (41), 25081–25090. https://doi.org/10.1021/acs.jpcc.9b06727.

(35) Zhao, Z.; Goncalves, R. V.; Barman, S. K.; Willard, E. J.; Byle, E.; Perry, R.; Wu, Z.; Huda, M. N.; Moulé, A. J.; Osterloh, F. E. Electronic Structure Basis for Enhanced Overall Water Splitting Photocatalysis with Aluminum Doped $SrTiO_3$ in Natural Sunlight. *Energy Environ. Sci.* **2019**, *12* (4), 1385–1395. https://doi.org/10.1039/c9ee00310j.

(36) Kronik, L.; Shapira, Y. Surface Photovoltage Phenomena: Theory, Experimental and Application. *Surf. Sci. Rep.* **1999**, *37*, 1–206. https://doi.org/10.1016/S0167-5729(99)00002-3.

(37) Dittrich, T.; Fengler, S. *Surface Photovoltage Analysis of Photoactive Materials*; World Scientific: London, 2020. https://doi.org/10.1142/q0227.

(38) Kronik, L.; Shapira, Y. Surface Photovoltage Spectroscopy of Semiconductor Structures: At the Crossroads of Physics, Chemistry and Electrical Engineering. *Surf. Interface Anal.* **2001**, *31* (10), 954–965. https://doi.org/10.1002/sia.1132.

(39) Sharma, G.; Zhao, Z.; Sarker, P.; Nail, B. A.; Wang, J.; Huda, M. N.; Osterloh, F. E.

Electronic Structure, Photovoltage, and Photocatalytic Hydrogen Evolution with p-$CuBi_2O_4$ Nanocrystals. *J. Mater. Chem. A* **2016**, *4* (8), 2936–2942. https://doi.org/10.1039/c5ta07040f.

(40) Zhao, J.; Holmes, M. A.; Osterloh, F. E. Quantum Confinement Controls Photocatalysis: A Free Energy Analysis for Photocatalytic Proton Reduction at CdSe Nanocrystals. *ACS Nano* **2013**, *7* (5), 4316–4325. https://doi.org/10.1021/nn400826h.

(41) Daemi, S.; Kundmann, A.; Becker, K.; Cendula, P.; Osterloh, F. E. Contactless Measurement of the Photovoltage in $BiVO_4$ Photoelectrodes. *Energy Environ. Sci.* **2023**, *16* (10), 4530–4538. https://doi.org/10.1039/d3ee02087h.

(42) Cheng, Y.; Xiao, C.; Mahmoudi, B.; Scheer, R.; Maijenburg, A. W.; Osterloh, F. E. Effect of Charge Selective Contacts on the Quasi Fermi Level Splitting of $CuGa_3Se_5$ Thin Film Photocathodes for Hydrogen Evolution and Methylviologen Reduction . *EES Catal.* **2023**, *1* (1), 74–83. https://doi.org/10.1039/d2ey00062h.

(43) Iqbal, A.; Yuan, S.; Wang, Z.; Bevan, K. H. Impact of Bulk Trapping Phenomena on the Maximum Attainable Photovoltage of Semiconductor-Liquid Interfaces. *J. Phys. Chem. C* **2018**, *122* (42), 23878–23889. https://doi.org/10.1021/acs.jpcc.8b06854.

(44) Memming, R. *Semiconductor Electrochemistry*; 2015. https://doi.org/10.1002/9783527688685.ch7.

(45) Prévot, M. S.; Sivula, K. Photoelectrochemical Tandem Cells for Solar Water Splitting. *J. Phys. Chem. C* **2013**, *117* (35), 17879–17893. https://doi.org/10.1021/jp405291g.

(46) Hu, S.; Xiang, C.; Haussener, S.; Berger, A. D.; Lewis, N. S. An Analysis of the Optimal Band Gaps of Light Absorbers in Integrated Tandem Photoelectrochemical Water-Splitting Systems. *Energy Environ. Sci.* **2013**, *6* (10), 2984–2993. https://doi.org/10.1039/c3ee40453f.

(47) Fountaine, K. T.; Lewerenz, H. J.; Atwater, H. A. Efficiency Limits for Photoelectrochemical Water-Splitting. *Nat. Commun.* **2016**, *7*, 1–9. https://doi.org/10.1038/ncomms13706.

(48) Chen, Z.; Dinh, H.; Miller, E. *Photoelectrochemical Water Splitting Standards, Experimental Methods, and Protocols*; Springer, 2013. https://doi.org/10.1007/978-1-4614-8298-7_2.

(49) Dubouis, N.; Grimaud, A. The Hydrogen Evolution Reaction: From Material to Interfacial Descriptors. *Chem. Sci.* **2019**, *10* (40), 9165–9181. https://doi.org/10.1039/c9sc03831k.

(50) Durst, J.; Simon, C.; Siebel, A.; Rheinländer, P. J.; Schuler, T.; Hanzlik, M.; Herranz, J.; Hasché, F.; Gasteiger, H. A. (Invited) Hydrogen Oxidation and Evolution Reaction (HOR/HER) on Pt Electrodes in Acid vs. Alkaline Electrolytes: Mechanism, Activity and Particle Size Effects. *ECS Trans.* **2014**, *64* (3), 1069–1080. https://doi.org/10.1149/06403.1069ecst.

(51) Sun, M.; Li, Y.; Wang, S.; Wang, Z.; Lia, Z.; Zhang, T. Non-Precious Metal-Based Heterostructure Catalysts for Hydrogen Evolution Reaction: Mechanisms, Design Principles, and Future Prospects. *Nanoscale* **2023**, No. 33. https://doi.org/10.1039/D3NR01836A.

(52) Zhao, Z.; Willard, E. J.; Dominguez, J. R.; Wu, Z.; Osterloh, F. E. Depletion Layer Controls Photocatalytic Hydrogen Evolution with P-Type Gallium Phosphide Particles. *J. Mater. Chem. A* **2019**, *7* (30), 18020–18029. https://doi.org/10.1039/c9ta05879f.

(53) Wu, P.; Wang, J.; Zhao, J.; Guo, L.; Osterloh, F. E. Structure Defects in G-C_3N_4 Limit Visible Light Driven Hydrogen Evolution and Photovoltage. *J. Mater. Chem. A* **2014**, *2* (47), 20338–20344. https://doi.org/10.1039/c4ta04100c.

Chapter 2 - 14.8% Quantum Efficient Gallium Phosphide (GaP) Photocatalyst for Hydrogen Evolution

Reproduced from J. Am. Chem. Soc. 2024, 146, 7723−7733.

2.1 Abstract

Gallium phosphide is an established photoelectrode material for H_2 or O_2 evolution from water, but particle-based GaP photocatalysts for H_2 evolution are very rare. To understand the reasons, we investigated the photocatalytic H_2 evolution reaction (HER) of suspended n-type GaP particles with iodide, sulfite, ferricyanide, ferrous ion, and hydrosulfide as sacrificial electron donors, and using Pt, $Rh_yCr_{2-y}O_3$, and Ni_2P HER cocatalysts. A record apparent quantum efficiency of 14.8% at 525 nm was achieved after removing gallium and oxide charge trapping states from the GaP surface, adding a Ni_2P cocatalyst to reduce the proton reduction overpotential, lowering the Schottky-barrier at the GaP-cocatalyst interface, adjusting the polarity of the depletion layer at the GaP-liquid interface, and after optimizing the electrochemical potential of the electron donor. The work not only showcases the main factors that control charge separation in suspended photocatalysts, but it also explains why most known HER photocatalysts in the literature are based on n-type and not p-type semiconductors.

2.2 Introduction

Photocatalytic overall water splitting is a promising pathway to solar hydrogen fuel.[1-6] The best known single-absorber photocatalyst based on $SrTiO_3$ reaches nearly 100% quantum

efficiency at 350-360 nm, [7] and the best known tandem, $Rh_yCr_{2-y}O_3$-Rh,La:$SrTiO_3$/Mo:$BiVO_4$, achieves a quantum efficiency of 30% at 419 nm.[8] However, the solar-to-hydrogen (STH) efficiencies of both photocatalysts are still low (0.65-1.1 %) and fundamentally limited by the large band gaps of the absorbers (3.2 eV for $SrTiO_3$ and 2.3 eV for Rh,La:$SrTiO_3$), and by their low absorptivity in the visible region of the solar spectrum.[9] Because STH efficiency is controlled mainly by the light harvesting ability of the light absorber,[10] improved photocatalysts require semiconductors with smaller band gaps.[11-12] Main group element compounds are the most promising candidates for such photocatalysts because of their superior electronic properties and because their conduction band edges are sufficiently reducing for protons.[13] However, for reasons not entirely clear, the number of main group element photocatalysts for the hydrogen evolution reaction (HER), is very small compared to many transition metal based photocatalysts that have been discovered over the years.[14-16] Examples of main group element photocatalysts for HER include C_3N_4,[17] GaN,[18] InGaN [19] SnS,[20] Si,[21] Ge_3N_4,[22-23] black phosphorus,[24] InP,[25] and Bi_2S_3.[26]

GaP is a main group element semiconductor with a zinc-blend crystal structure and a conduction band edge approximately -1.25 V relative to the proton reduction potential.[27-28] Based on its 2.3 eV band gap,[27] a theoretical STH of 12% is possible with this material. Indeed, high-performing GaP photoelectrodes[29] have been described for many reactions, including chalcogenide oxidation,[30] water oxidation (with TiO_2 protection layer),[31-32] hydrogen evolution,[33-37] CO_2 reduction,[38-39] methyl viologen [40] and ferrocene reduction.[41] In contrast, demonstrations of GaP particle photocatalysts for HER are rare and riddled with low activity. In their 2011 paper, Sun et al confirmed sub-micromolar but steady H_2 evolution from an irradiated suspension of Pt

decorated GaP nanowires under visible light illumination, and using methanol as electron donor.[42] In 2019, we reported photocatalytic HER with GaP particles obtained from a p-GaP wafer. Using iodide as electron donor, the Ni_2P-modified GaP particles achieved a H_2 evolution activity of 13.5 mmol/h[1] under visible light illumination.[43] Among other causes, the low activity was attributed to the inverted polarity of the p-GaP space charge region at the solid-liquid interface (Fig. 2.1a).

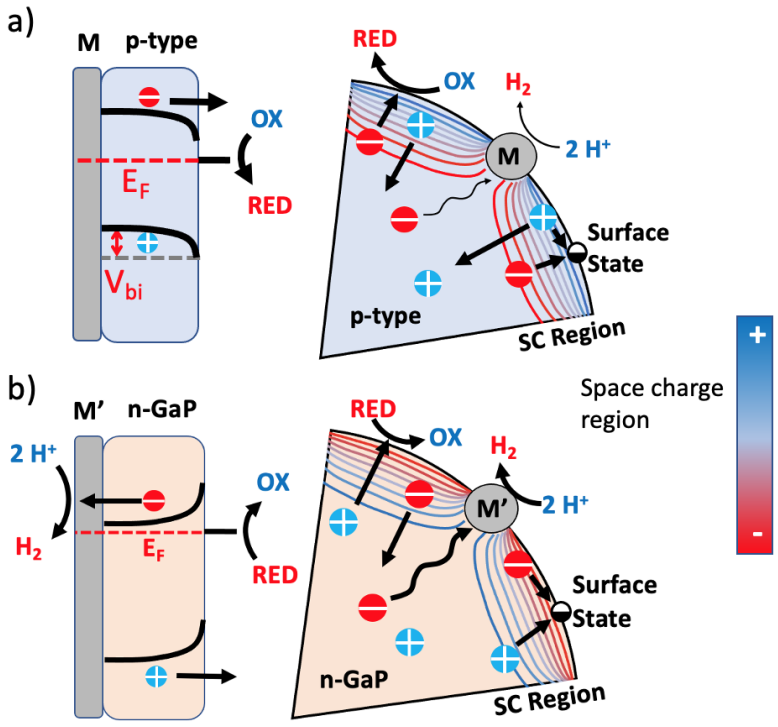

Figure 2.1 Band bending, charge separation, and surface recombination in illuminated a) p-type and b) n-type GaP/M photocatalysts in contact with a sacrificial electron donor (M, M': HER cocatalysts). Ohmic contacts are assumed at the GaP/ metal contacts and band bending is controlled by the built-in potential at the GaP-liquid contacts. Shown also are Fermi level (E_F), built-in potential (V_{bi}), and the space charge region (SCR).

Because the electric field associated with the built-in potential V_{bi} guides photoholes away from the GaP-liquid interface, oxidation of the redox couple in the electrolyte becomes difficult. Based on this model, we hypothesize here that greatly improved HER activity should occur with n-GaP particles. The electric field in the depletion layer at the n-GaP/liquid interface has a reversed polarity (Fig. 2.1b), and therefore should function as a photoanode for oxidation of the sacrificial donor. The electrons generated by the process can reach the cocatalyst by diffusion, allowing the HER to occur.

In this work, we confirm this hypothesis with n-GaP particles derived from a commercial S:GaP wafer. The optimized photocatalyst evolves H_2 at 14.8% apparent quantum efficiency (AQE) at 525 nm. This record performance is possible after removal of charge trapping defects at the n-GaP surface, after identification of a suitable HER cocatalyst, and after selecting $NaSH/Na_2SO_3$ as sacrificial electron donor. We also find that the HER rate depends strongly on the electronic properties of the SCR-cocatalyst contact and on the reducing power of the hole scavengers. These observations improve our understanding of how Schottky junctions control charge separation and how the overall reaction energetics drive H_2 evolution. Importantly, the findings explain why most HER photocatalysts in the literature are based on n-type semiconductors, rather than p-type materials. This will aid the search for new small band gap photocatalysts for the hydrogen evolution reaction.

2.3 Results and Discussion

Gallium phosphide particles were obtained as brown or orange powders by mechanical grinding of a commercial n-type sulfur-doped GaP wafer (Fig. 2.2a and b). Based on SEM (Fig. 2.2c and 2.S1), the particles are shaped irregularly without distinguishable facets, and polydisperse with an average size of 550 nm. The powder X-ray diffraction pattern (Fig. 2.2d) of the GaP powder matches the zinc blende GaP standard (PDF #00-12-0191) with no impurity phases present. While mechanical grinding of semiconductor wafers is rarely used to obtain photocatalyst particles,[43] previous works have demonstrated wafer etching as a pathway to achieve high surface area photoelectrodes.[40, 44]

Diffuse reflectance optical absorption spectra of the two sides of the GaP wafer and of the derived powder are shown in Fig. 2.3. For the wafer, the spectra reveal an optical absorption onset at 2.16 eV, in the range of the reported optical band gaps (2.1-2.3 eV) for the material.[27, 30, 45-46] Here, the weaker diffuse reflectance signal for the polished side is due to specular reflection. The spectra also show a very broad absorption at 1.2 eV, which can be attributed to excitation of free conduction band electrons.[46] The free carriers result from ionization of S/S^{2-} donor states located 0.107 eV below the GaP conduction band.[27]

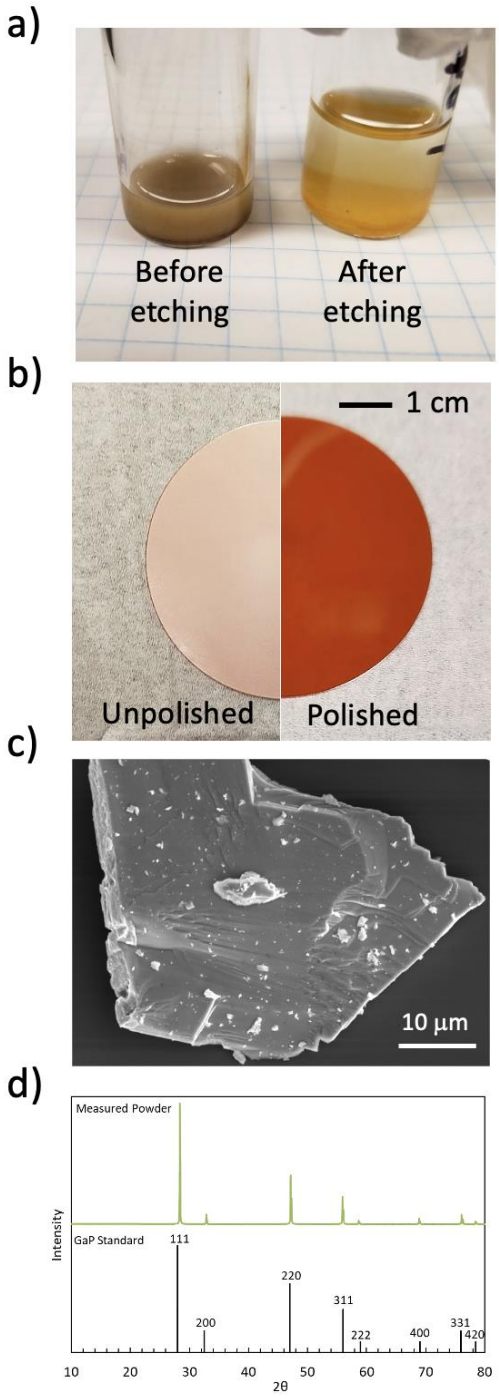

Figure 2.2 (a) Photos of n-GaP powder suspended in ethanol before and after etching. (b) Photos of the rough and polished sides of the n-GaP wafer. (c) Scanning electron micrograph of a single n-GaP particle obtained from a S-doped GaP wafer and (d) XRD pattern.

In the GaP powder, the main absorption onset is shifted to 1.2 eV, approximately 1 eV below the band gap. The sub-bandgap absorption is attributed to states formed during surface oxidation of the GaP powder. Earlier photoluminescence studies[46-47] place O/O^{2-} defects in GaP 0.897 eV below the conduction band edge. These defects are responsible for the brown color of the GaP powder (Fig. 2.3a). Indeed, etching of the GaP powder in piranha acid completely removes the defect absorption in Fig. 2.3b and changes the color of the powder from brown to orange. Etching does not significantly change the particle morphology, but causes small pits and trenches to appear on the surface of the larger particles (Fig. 2.S1c,d).

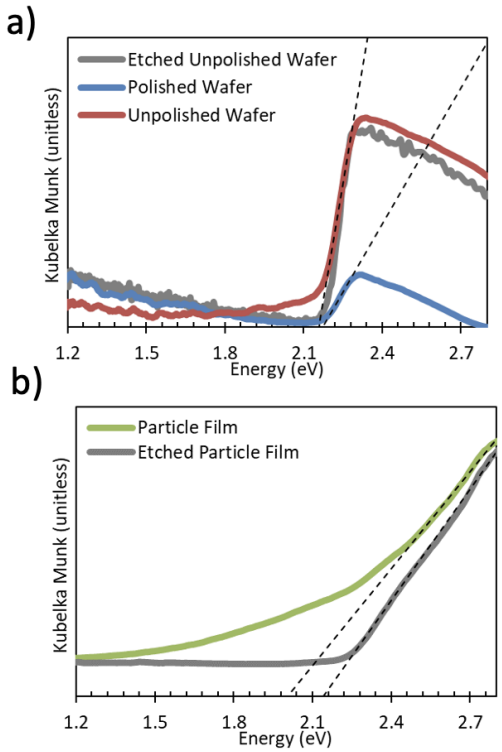

Figure 2.3 Kubelka-Munk (KM) diffuse reflectance spectra of (a) n-GaP wafer and (b) n-GaP powder. The KM signal of the polished wafer is reduced by the specular reflection on the smooth surface.

To assess the ability of n-GaP to generate a photovoltage under illumination, Vibrating Kelvin Probe Surface Photovoltage (VKP-SPV) spectra were recorded on the unpolished side of the as-received wafer. In VKP-SPV, the contact potential difference (CPD) of the wafer is measured in a contactless way with a vibrating, semi-transparent gold Kelvin probe.[48] The SPV signal represents the change of the contact potential difference, SPV = CPD(light) - CPD(dark), resulting from light-induced charge separation. It provides an estimate of the photovoltage of the sample, that is the difference of the electrochemical potentials of the majority and minority carriers at the sample surface.[49-51] SPV spectra are shown in Fig. 2.4a together with the logarithmic plot of the Xe light intensity. For all samples, negative SPV signals are observed (electrons move away from the Kelvin probe) in agreement with charge separation within the electron depletion layer at the n-GaP surface, as shown in Fig. 2.4b. Analogously, previous SPV measurements on p-GaP have yielded positive SPV signals, due to the opposite polarity of the depletion layer.[43] For n-GaP, the maximum SPV is reached at 3.0 eV, where GaP absorbs light and the light intensity from the Xe-Light source are at a maximum. At higher photon energy, the SPV signal is reduced by the decreasing light intensity of the Xe lamp.

For the etched wafer, the SPV signal begins at 2.06 eV and is assigned to band gap excitation of GaP. The 0.1 eV deviation from the bandgap value in Fig. 2.4a is attributed to Urbach tail states at the GaP surface and near the band edges. These states are detected by SPV, due to its greater sensitivity compared to UV/vis spectroscopy. For the as-received wafers, the photovoltage onset occurs much earlier and is attributed to the excitation of surface defects, as shown in Fig. 2.4b. Based on the 1.3 eV photoonset, the states are located 1.3 eV below the GaP conduction band edge. To identify the chemical origin of the defects, two kinds of surface

treatments were applied to a freshly etched wafer. In one experiment, the etched wafer was heated to 600 ^{o}C in air for 6 hours to create a surface oxide layer. XPS survey spectra of the oxidized wafer confirm that this surface treatment causes oxidation of the wafer and leads to increased oxygen and reduced phosphorous content relative to the etched wafer (Fig. 2.S2 and Table 2.S3).

The SPV spectrum of the oxidized wafer is also shown in Fig. 2.4a. It contains an increased SPV signal at 3.0 eV, but the sub-band gap signal in the 1.4 -1.7 eV region is weaker than in the as-received wafer. This suggests that surface oxides are *not* responsible for the 1.4 eV photovoltage signal, but instead produce a separate SPV feature at photon energies above 1.8 eV. These states also increase the SPV signal at 3.0 eV by pinning the Fermi level near the O/O^{2-} energy (Fig. 2.4b), which leads to increased band bending. As expected, 5 min piranha etching of the oxidized wafer restores the SPV spectrum of the original etched wafer.

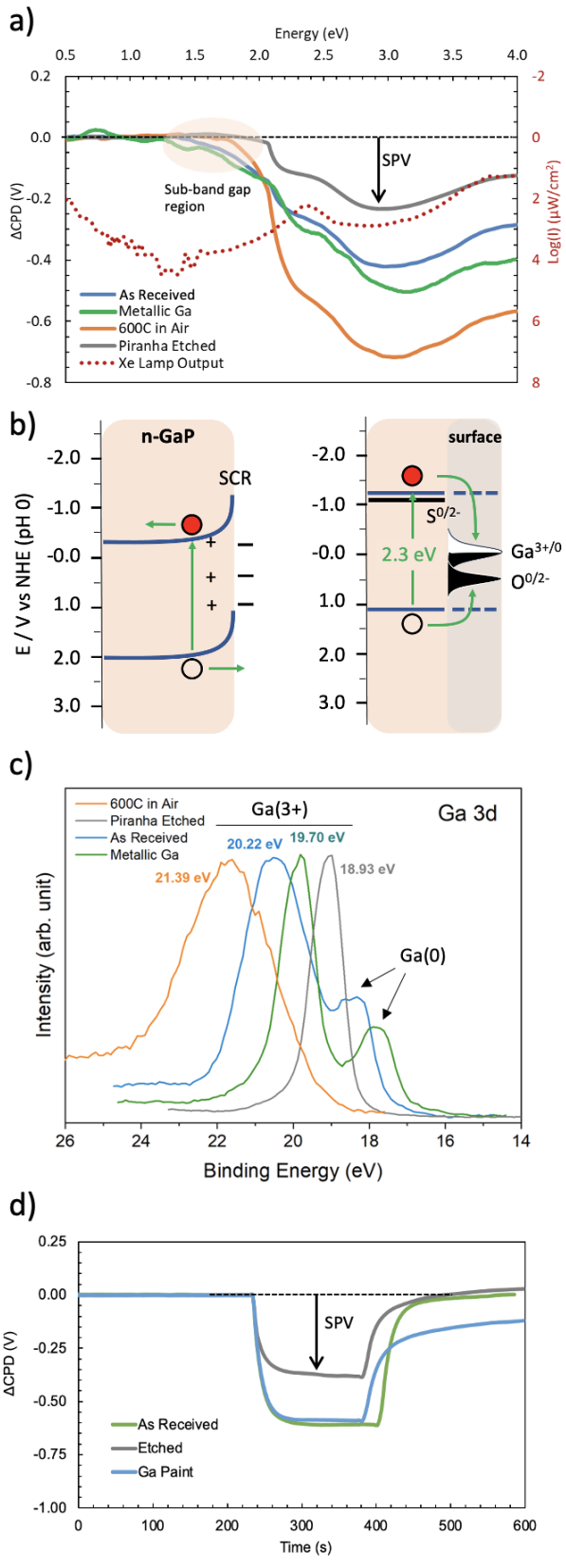
a)
Energy (eV)
0.5 1.0 1.5 2.0 2.5 3.0 3.5 4.0
0.2 0.0 -0.2 -0.4 -0.6 -0.8
ΔCPD (V)
-2 0 2 4 6 8
Log(I) (μW/cm²)
SPV
Sub-band gap region
As Received
Metallic Ga
600C in Air
Piranha Etched
Xe Lamp Output
b)
n-GaP
SCR
surface
E / V vs NHE (pH 0)
-2.0 -1.0 -0.0 1.0 2.0 3.0
S0/2-
2.3 eV
Ga3+/0
O0/2-
c)
600C in Air
Piranha Etched
As Received
Metallic Ga
Ga(3+)
Ga 3d
20.22 eV
19.70 eV
21.39 eV
18.93 eV
Ga(0)
Intensity (arb. unit)
26 24 22 20 18 16 14
Binding Energy (eV)
d)
0.25 0.00 -0.25 -0.50 -0.75 -1.00
ΔCPD (V)
SPV
As Received
Etched
Ga Paint
0 100 200 300 400 500 600
Time (s)

Figure 2.4 (a) Surface photovoltage spectra of unpolished n-GaP wafer before and after surface treatments. The logarithm of the light intensity is shown as dotted line. Above 2.5 eV, the SPV spectra are modulated by the light emission profile of the Xe-light source. (b) Band energy diagrams for n-GaP showing photochemical charge separation and position of defect states. Band edge positions from Chen et al.[28] c) XPS fine structure for Ga region. Spectra are normalized based on the strongest peak. Numerical values in Table 2.S3. d) SPV signal under temporal 405 nm illumination.

In a separate experiment, a thin layer of metallic gallium at 30 ^{o}C was painted onto the surface of the freshly etched n-GaP (Photo in Fig. 2.S4). According to XPS, this increases the Ga/P ratio to 2.2 (Table 2.S3) and adds a Ga(0) population at 17.72 eV as the right shoulder to the existing Ga(3+) states of the etched wafer at 19.70 eV[52-53] (Fig. 2.4c and Table 2.S5). The peak assignment of metallic Ga(0) is based on the 1.98 eV energy difference between the right shoulder and the major peak from Ga(3+).[54] The SPV spectrum of the Ga(0) treated n-GaP wafer (Fig. 2.4a) closely resembles the spectrum of the as-received wafer. This suggests that Ga(0) surface states are responsible for the sub bandgap SPV signal, via excitation of electrons into the GaP conduction band, as shown in Fig. 2.4b. Based on the 1.3 eV photo-onset, the Ga(0) states are located 1.3 eV below the conduction band at +0.1 V vs RHE. The Ga(0) states also increase of the photovoltage signal at 3.0 eV, but not as much as the O/O^{2-} states because the Ga(3+/0) Fermi level is more reducing. In the as-received wafer, surface Ga(0) can form by electron transfer from the GaP wafer (E_F = -1.1 V vs RHE) into empty Ga(+3) surface states. Indeed, XPS (Fig. 2.4c) confirms the presence of both Ga(3+) and Ga(0) on the as-received wafer. In the oxidized wafer,

on the other hand, all gallium is present in the form of Ga_2O_3 or $GaPO_m$ (m = 3 - 4), based on the Ga^{3+}-O-P $3d_{5/2}$ peak at 21.39 eV.[55]

To further evaluate the effect of the surface states on the charge carrier *dynamics* of the GaP wafer, SPV signals were recorded under temporal 405 nm LED illumination (Fig. 2.4d). This produces SPV signals of comparable magnitude to the data in Fig. 2.4a. The photovoltage forms reversibly and on the 20 s time scale, indicating good carrier mobility, as is typical for what was previously observed for GaAs, silicon, and GaN.[56-58] For the as-received and etched GaP wafers, the photovoltage signal forms on the 10-15 s timescale and decays on the 20 s time scale. For the gallium-treated wafer, on the other hand, the decay is much slower (55 s), and 22% of the photovoltage is retained after 200 s. That shows that the Ga(0)-states on the wafer surface can trap photoholes, as shown in Fig. 2.4b.

Next, to evaluate the ability of n-GaP particles to function as a photocatalyst for H_2 evolution, 50 mg of n-GaP powder was suspended in 50 mL of aqueous 0.05 M KI in 0.1 M phosphate buffer at pH 7.2 and irradiated with visible light. Potassium iodide was chosen as a mild sacrificial electron donor because it works well with a p-GaP HER photocatalyst.[43] As can be seen in Fig. 2.5a, H_2 is evolved at a small but steady rate of 0.67 µmol/h. When the n-GaP particles are etched prior to illumination, the H_2 rate increases to 1.12 µmol/h. This shows that removal of the O and Ga surfaces states boosts the photocatalytic activity. This agrees with the well-established fact that states in the middle of the bandgap promote recombination of carriers by trapping electron and holes.[7, 59-60] This reduces the steady state hole concentration under illumination and with it the driving force for the photoelectrochemical reaction.

Because it is known that GaP has a substantial kinetic overpotential for the HER, [61] further activity increases are expected from adding a HER cocatalyst. Accordingly, Pt, $Rh_yCr_{2-y}O_3$, or Ni_2P cocatalysts were attached to the GaP particles by photodeposition or impregnation, as described in the experimental section. These materials have been shown to reduce protons at low overpotentials.[62-65] TEM images in Fig. 2.S6 show that the cocatalysts are randomly distributed on the GaP surface. As can be seen in Fig. 2.5b, etched n-GaP particles loaded with Pt, $Rh_{2-y}Cr_yO_3$, and Ni_2P evolve H_2 at 7.69 µmol/h, 8.26 µmol/h, and 37.90 µmol/h, respectively, approximately 7 – 34 times faster than without cocatalysts (data in Fig. 2.S7). Again, H_2 evolution rates of the non-etched GaP particles are much lower. This is a result of recombination at the photohole trapping Ga(+3/0) surface states, as seen in the photovoltage spectra.

The photocatalytic experiments show that Ni_2P outperforms Pt and $Rh_{2-y}Cr_yO_3$ as HER cocatalyst. This disagrees with the hydrogen evolution overpotentials of the materials which increase in order of Pt < Ni_2P < $Rh_{2-y}Cr_yO_3$, i.e., Pt is a better HER catalyst than Ni_2P.[62-66] Instead, the reactivity trend can be explained with the Schottky junction model in Fig. 2.5c. Based on the known work functions of Pt (5.64 eV)[67] and Ni_2P (4.69 eV),[68] significant Schottky barriers of 2.24 eV and 1.29 eV, respectively, are expected at the n-GaP (E_F = 3.4 eV)-cocatalyst interfaces. Indeed, for n-GaP/Pt a Schottky barrier of 1.5 eV has been measured previously.[69] These barriers prevent electron transfer from n-GaP to the cocatalyst and thus inhibit proton reduction. Ni_2P has the smallest barrier with GaP, and therefore, electron transfer to the cocatalyst is fastest and the HER rate is highest. Based on Kelvin probe contact potential difference (CPD) measurements (Fig. 2.5d), the work function of $Rh_{2-y}Cr_yO_3$ is in between that of Pt and Ni_2P, and therefore the n-GaP/ $Rh_{2-y}Cr_yO_3$ Schottky barrier is of intermediate height. This data agrees well with the

reactivity trend seen in Fig. 2.5b, confirming that the Schottky-junction at the GaP-cocatalyst interface is a limiting factor for HER. An alternative explanation for the lower performance of the n-GaP/Pt photocatalyst is an increased electron-hole recombination rate at the n-semiconductor/metal interface, as has been observed experimentally for n-$GaInP_2$/Pt.[70]

To further optimize hydrogen evolution from the photocatalysts, irradiation experiments were conducted with different sacrificial electron donors, incl. iodide (I^-), ferrous ion (Fe^{2+}), sulfite (SO_3^{2-}), hydrosulfide (HS^-), and hexacyanoferrate ($Fe(CN)_6^{4-}$). Because electrochemical reactions are driven by the charge transfer thermodynamics,[71] the overall photocatalytic reaction shown in Fig. 2.6a is expected to be a function of the redox potential of the sacrificial electron donor. Indeed, this is confirmed experimentally. Fig. 2.6b shows a plot of the observed H_2 evolution rates (Fig. 2.S8) versus the pH-corrected electrochemical potential (RHE) of the donors. It can be seen that the H_2 rates are a direct function of the reducing power, with highest values (~7.06 µmol/h) seen for Na_2SO_3 and Na_2S and lowest values for KI and $FeSO_4$, due to the less reducing electrochemical potentials of the latter. Identical H_2 evolution rates are observed for KI at pH 6.2 and HCF at pH 9.4 because the redox potentials of these two donors are equal (0.91 V vs RHE). This confirms that the reducing power of the electron donor is main determinant of the H_2 evolution rate.

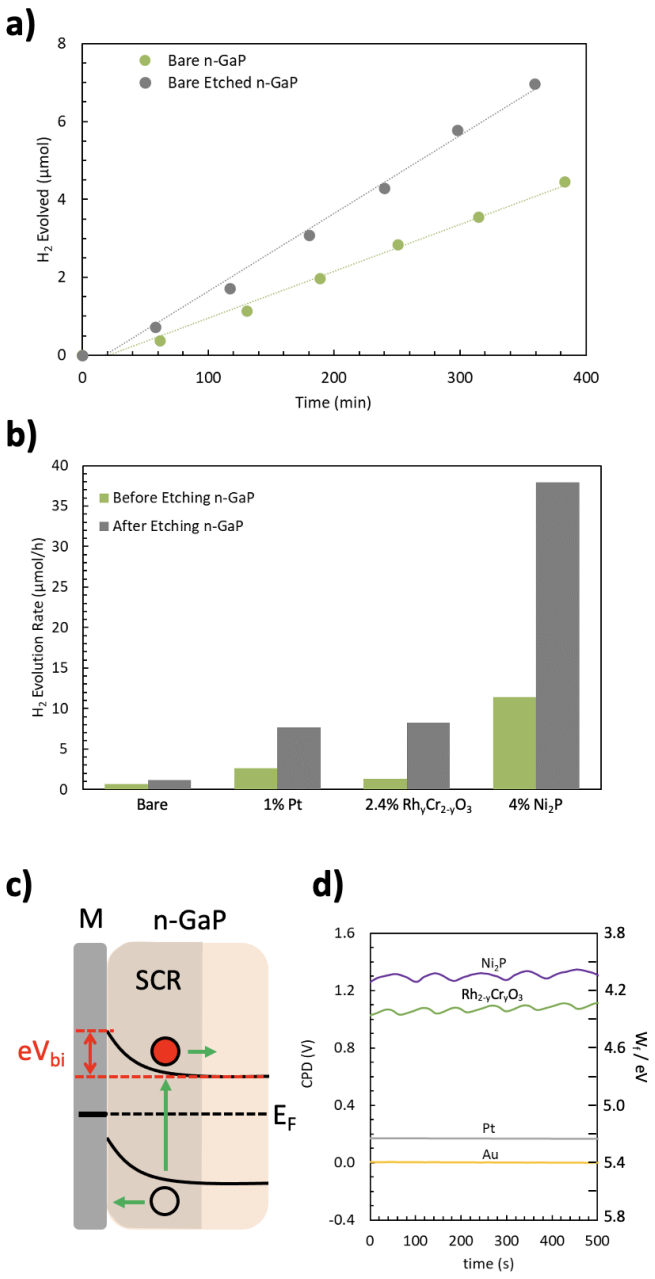

Figure 2.5 (a) H_2 evolution data from n-GaP electrocatalyst in 50.0 mL of 0.05 M KI in 0.10 M phosphate buffer at pH 7.2 under visible light (l >400 nm, 300 W Xe arc lamp, 380-450 mW/cm^2 irradiance at the flask). (b) Summary of H_2 evolution data for bare, 1% Pt, 2.4% $Rh_yCr_{2-y}O_3$, and 4% Ni_2P-loaded photocatalysts using etched and non-etched GaP particles. Measured data is

shown in Fig. 2.S7 and Table 2.S8. (c) Schottky junction at the GaP-cocatalyst (M) interface. To reach the cocatalyst M, photogenerated electrons need to overcome the barrier eV_{bi}, where V_{bi} is the built-in potential [E_F(M)-E_F(GaP)]. (d) Contact potential difference values (relative to gold, measured in vacuum) for $Rh_{2-y}Cr_yO_3$ and Ni_2P films and a Pt wire.

The redox potentials of the $HCF^{3-/4-}$, I_3^-/I^-, and $Fe^{3+/2+}$ couples are pH-independent on the NHE scale, but not on the pH-dependent RHE scale. As a result, the HER rates for these couples increase with decreasing pH. The SO_4^{2-} / SO_3^{2-} redox couple, on the other hand, has the same 59 mV pH^{-1} dependence as the relative hydrogen electrode (RHE), so the two pH dependences cancel out, and similar HER rates (6.6 μmol/h) are observed at all 3 pH conditions. The results in Fig. 2.6 suggest that the H_2 evolution kinetics with the n-GaP/Pt photocatalyst are controlled by the Gibbs free energy change (DG_R) of the overall photocatalytic reaction, as shown in Eq 2.1 and Eq. 2.2.

$$2\ Red + 2\ H^+ \rightarrow H_2 + 2\ Ox \qquad \text{(Equation 2.1)}$$

$$DG_R = -\ 2\ F\ [E^0(H^+/H_2) - E^0(Ox/Red)] \qquad \text{(Equation 2.2)}$$

$$DG^{\ddagger} = \alpha DG_R + \beta \qquad \text{(Equation 2.3)}$$

$$k_{H2} = (k_B T / h) \exp(-\Delta G^{\ddagger} / RT) \qquad \text{(Equation 2.4)}$$

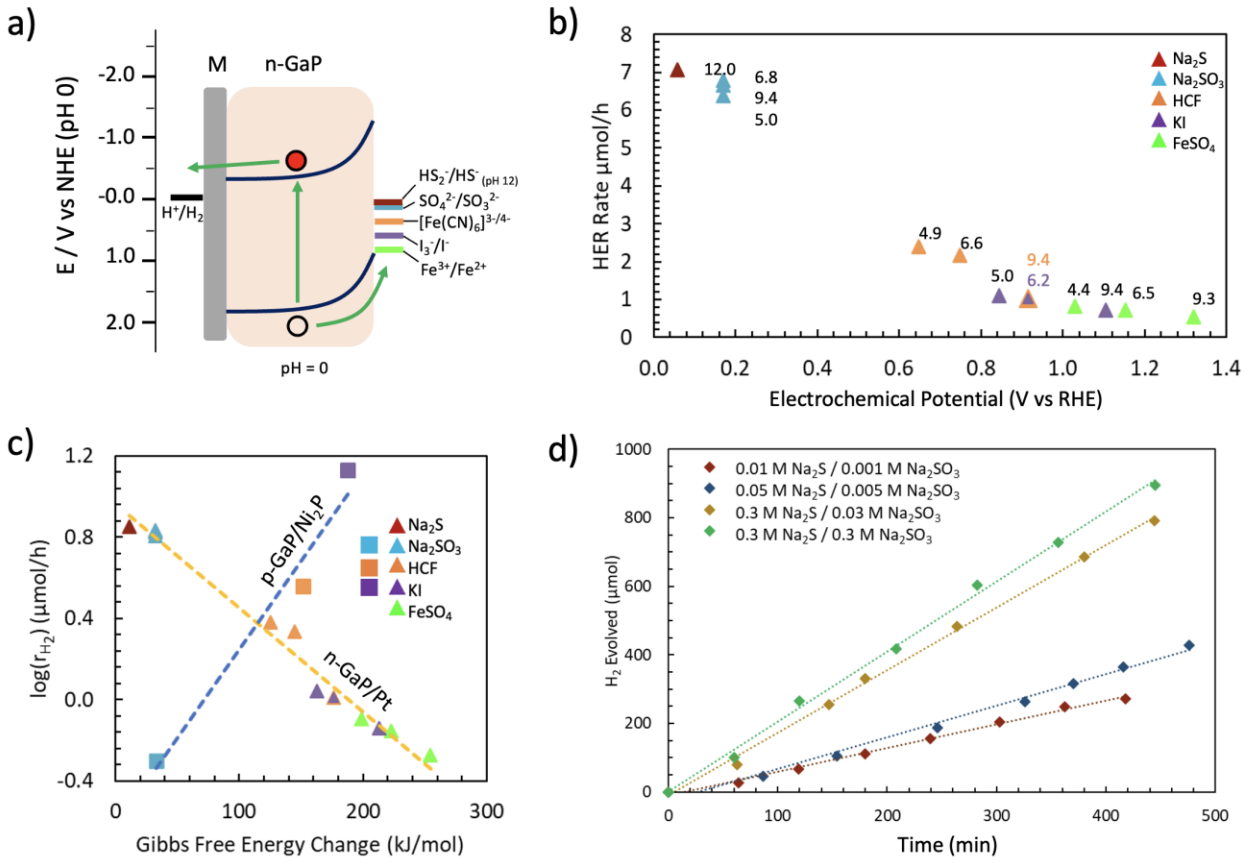

Figure 2.6 (a) Energy diagram of Pt/n-GaP in the presence of sacrificial electron donors. The E^0 for HS_2^-/HS^- is shown at pH 12 because E^0 is not defined at pH 0. (b) Measured HER rates versus the electrochemical potential of the sacrificial donors at various pH values (labels in the plot). Experimental data is shown in Fig. 2.S9 and numerical data in Table 2.S10. (c) Plot of the logarithmic hydrogen evolution rate of n-GaP/Pt and p-GaP/Ni_2P versus Reaction Gibbs Energy Change DG_R. Note that DG_R is positive for all conditions, corresponding to a thermodynamically forbidden (endergonic) process. Data for p-GaP/Ni_2P from Zhao et al.[43] (d) H_2 evolution from 4%-loaded Ni_2P /n-GaP (etched) in 50.0 mL aqueous sulfide/sulfite solution under visible light (l >400

nm, 300 W Xe arc lamp, estimated irradiance at the flask 380-450 mW/cm^2). Data shown in Table 2.S11.

Here, RED and OX are the reduced and oxidized forms of the sacrificial reagent, and F is the Faraday constant. Assuming a linear free energy relationship (Eq. 2.3) between the Gibbs free energy change (DG_R) and the Gibbs free energy of activation $DG^{‡}$ (a and b are constants), [71] and using the Eyring Eq 2.4 for the kinetic rate constant k_{H2}, it can be seen that the logarithmic hydrogen evolution rate should have a linear dependence on the driving force for the overall reaction (at constant pH). Indeed, a plot of $\log_{10}(r_{H2})$ versus DG_R is linear (Fig. 2.6c), confirming the validity of this model. Deviations from linearity are attributed to the effect of the proton concentration on the electron transfer rate, which is not captured in Eq. 2.3 and Eq. 2.4. Fig. 2.6c also shows that the reaction is endergonic (DG_R is positive) for all electron donors. This means that H_2 evolution results from the net conversion of photochemical energy into Gibbs free energy (Eq. 2.1), as wanted for a *fuel forming process*.[72] The highest rates are seen for sulfide because it is the most reducing electron donor (E^0 = 0.055 V vs RHE at pH 12) in the series. Remarkably, the reactivity trend (orange fit) for the earlier reported p-GaP/Pt HER photocatalysts is opposite of that for n-GaP/Ni_2P photocatalyst.[43] For the p-GaP/Ni_2P catalyst, the H_2 evolution rate *decreases* with increasing driving force of the reaction DG_R (Fig. 2.6c). This is due to the dominating influence of the space charge region at the p-GaP/liquid contact on charge separation. Because the polarity of the space charge region in p-GaP is inverted (Fig. 2.1a), it impedes hole-transfer from p-GaP to the sacrificial donors and prevents capture of electrons needed for proton reduction. According to surface photovoltage measurements, hole-transfer barrier heights (V_{bi}) for the p-GaP/electrolyte interface increase in the order of KI (0.25 eV), HCF (0.37 eV), and Na_2SO_3

(0.45 eV).[43] This agrees with the prediction of the Schottky model, according to which the barrier $V_{bi} = E^0(Ox/red) - E_F(GaP)$ grows as the sacrificial electron donors become more reducing (Fig. 2.1a). For n-GaP, on the other hand, the SCR does not introduce a hole transfer barrier and the rate of the HER is instead controlled by the linear free energy relationship in Eq. 2.3.

The model in Fig. 2.1 not only explains the data measured for n-GaP studied here but provides a general understanding for the established dominance of n-type over p-type photocatalysts for the hydrogen evolution reaction.[3, 73] For p-type photocatalysts, the polarity of the semiconductor-liquid junction prevents electron collection from the sacrificial donor in the solution, which limits hydrogen evolution. For practical applications of p-type semiconductors as HER materials, this problem is often overcome by providing electrons through a solid-solid contact. This can be done by interfacing the p-type semiconductor with an electrode support, for example in p-$CuGa_3Se_5$ photocathodes,[74] or with a n-type semiconductor, as in the Ru/$SrTiO_3$:Rh/$BiVO_4$ tandem.[75] Alternatively, the semiconductor-liquid junction hole transfer barrier is reduced by raising the semiconductor Fermi level through alloying with non-p-type semiconductors, as in $(ZnSe)_{0.5}(CuGa_{2.5}Se_{4.25})_{0.5}$.[76] However, stand-alone p-type photocatalysts for HER will always be limited by the incorrect polarity of the solid-liquid junction in Fig. 2.1a, which prevents electron collection from the solution phase.

The data in Fig. 2.6 also provides guidance on how to achieve a record performance with the n-GaP/Ni_2P catalyst, by choosing hydrosulfide with the most negative standard reduction potential. Accordingly, H_2 evolution experiments were repeated with n-GaP/Ni_2P (etched) in Na_2S solutions containing 10% (mol) Na_2SO_3. Here, sulfite is added to convert formed polysulfide into

thiosulfate, thereby reducing light shading from the former.[77] As seen in Fig. 2.6d, H_2 is evolved linearly in all cases, and the rates increase with increasing sacrificial donor concentration. The highest rate of 123 µmol/h is observed for a solution containing 0.3 M Na_2S and 0.3 M Na_2SO_3. When the experiment is repeated under 525 nm LED illumination, H_2 is evolved at a rate of 11.8 µmol h^{-1} (Fig. 2.S12 and Table 2.S13), corresponding to an apparent quantum efficiency (AQE) of 14.8 %. For n-GaP particles loaded with $Rh_{2-y}Cr_yO_3$, Pt, and bare n-GaP, AQEs are 6.3, 5.2, and 0.5%, respectively, lower than n-GaP particles loaded with Ni_2P, as expected, and following the previously observed trend. These are the highest reported AQEs for H_2 evolution from GaP photocatalyst particles.[42-43, 78-80]

To evaluate the long-term stability of the n-GaP/Ni_2P photocatalyst in sulfide/sulfite, sequential irradiation experiments were conducted in 6 h intervals. During the 18-hour period (Fig. 2.S7d) 1.4 millimoles of H_2 are evolved, corresponding to a turnover number of 2.8 for the photocatalyst. This suggests a catalytic process. However, as can be seen from the plot, the rate decreases by approximately half after each experiment, until it is only 31% of the original rate. This shows that the Ni_2P/GaP photocatalyst is not stable under the reaction conditions. Photocorrosion is a known problem of n-GaP in aqueous solutions.[30, 81] In the absence of stabilizing agents, GaP undergoes photoanodic conversion into either Ga(3+) and phosphoric acid (in alkaline solution), or GaO_2^- and elemental phosphor (in alkaline solution), with P undergoing further oxidation. [81-82] Indeed, when a proton-decoupled ^{31}P NMR spectrum (Fig. 2.S14) was recorded on the supernatant after an 18 h illumination period, a mixture of hydrogen phosphate (HPO_4^-) and phosphite (HPO_3^{2-}) is observed. Phosphite is formed by direct photocorrosion of

GaP (Eq 2.5), whereas the hydrogen phosphate is formed by photocatalytic oxidation (equation 6) under the air-free conditions of the reaction.

$$GaP + 9\ OH^-(aq) + 6\ h^+ \rightarrow GaO_2^-(aq) + HPO_3^{2-}(aq) + 4\ H_2O \quad \text{(equation 2.5)}$$

$$HPO_3^{2-}(aq) + 2\ OH^-(aq) + 2\ h^+ \rightarrow HPO_4^{2-}(aq) + H_2O \quad \text{(equation 2.6)}$$

These side reactions limit the usability of the n-GaP/Ni_2P photocatalytic system for large-scale photocatalytic production of H_2. Greater stability may be achievable by using selenide or telluride ions as alternative electron donors.[30]

2.4 Conclusions

In summary, we demonstrate photocatalytic H_2 evolution from Ni_2P-modified n-GaP particles with an AQE of 14.8% at 525 nm, two orders of magnitude higher than previous reports. The performance is a result of systematic optimization of junctions at the n-GaP-liquid and n-GaP-cocatalyst interfaces, removal of Ga(0) and O(2-) surface defects and adjustment of the redox potential of the sacrificial electron donor. The work shows that the correct polarity of the solid-liquid junction is essential to achieve hydrogen evolution with a semiconductor photocatalyst. In n-GaP photocatalysts, the depletion layer guides photoholes *towards* the sacrificial donor while in p-GaP particles the depletion layer moves photoholes *away* from it, preventing the collection of electrons for proton reduction. This explains the predominance of n-type semiconductors as hydrogen evolution photocatalysts in the literature. The work also reveals the importance of an ohmic contact at the GaP-cocatalyst contact. Pt and $Rh_{2-y}Cr_yO_3$ cocatalysts with large work functions generate a Schottky barrier in n-GaP that prevents electrons

from reaching the cocatalyst. For Ni_2P the barrier is the smallest, which explains the higher H_2 evolution activity with this cocatalyst. Also, we find that Ga(3+/0) surface defects reduce the photocatalytic activity by trapping holes, but they can be removed by etching GaP with piranha acid. Furthermore, it is established that photocatalytic HER with Pt/n-GaP follows a free energy relationship, i.e. the more reducing the sacrificial donor, the larger the H_2 evolution rate. Notably, all GaP/Ni_2P systems reported here generate H_2 under endergonic conditions, resulting in up to 1.3 eV energy storage per converted photon (with Fe^{2+} at pH 9.3). This is relevant to the development of n-GaP-derived tandem photocatalysts for overall water splitting. A side aspect of the free energy relationship is the observed dependence of the H_2 evolution rate on the solution pH. This effect is observed for sacrificial donors with a pH-independent redox potential (Fe^{2+}/Fe^{3+}, $Fe(CN)_6^{3-/4-}$), but not for sulfite, where the pH dependences of the donor and of the proton reduction reaction cancel out. Lastly, phosphate and phosphite are identified by NMR as products of GaP photocorrosion during photocatalysis. Improved stability may be achievable with other sacrificial donors, such as selenide, or by coupling the Ni_2P/n-GaP system to a water oxidation catalyst.

2.5 Experimental Section

N-type gallium phosphide wafers doped with sulfur (0.20 - 0.125 Ω cm, carrier density 4.5×10^{17} - 4.75×10^{17} cm^{-3}) were obtained from EL-CAT Inc. Hydrogen peroxide (30 wt% in H_2O), concentrated sulfuric acid, potassium iodide (99.9%), potassium hexacyanoferrate (ii) (99%), potassium hydroxide (99%), sodium sulfite (98%), sodium sulfide nonahydrate (98%), iron (ii) sulfate (99%), bisacetylacetonate nickel (ii) (98%, eMolecules), trioctylphosphine (90%),

oleylamine (80-90%,Fisher Scientific),dioctyl ether (99%, Fisher Scientific), hexanes (98.5%), chloroform (HPLC Grade, Thermo-Fisher), ethanol (200 proof), isopropanol (>99%), acetone (99.9%), polyvinylpyrrolidone (MM=55,000), dihydrogen hexachloroplatinate (IV) (99.9%, Alfa Aesar), rhodium (III) chloride (>99%, Fisher Scientific), chromium (III) nitrate nonahydrate (99%, Acros Organics) were used as received. Water was purified using a Nanopure system. Caution: Nickel compounds are carcinogenic.

GaP particles were prepared by grinding the commercial wafers for 45 min in an N_2 atmosphere in a glove box using a mortar and pestle. The resulting powder was stored in a closed container in the dark under N_2. The GaP wafer or the GaP particles were etched in a small beaker containing 3 mL H_2SO_4, 1 mL H_2O_2, and 1 mL H_2O ('piranha acid') at 50 °C for 5 min (particles) or 30 min (wafer). The wafer was washed 5 times with nanopure water to remove excess acid. The particle suspension was diluted to 50 mL of nanopure water after etching and centrifuged at 9,000 rpm for 4 minutes. This was repeated an additional 4 times with 50 mL water. The etched wafer and particles were dried in the dark under a N_2 flow.

Fluorine-doped tin oxide (FTO) and gold substrates were cleaned by ultrasonication in acetone for 15 minutes followed by nanopure water for an additional 15 min. The cleaned substrates were dried at 60°C for at least one hour.

Particle films (GaP, $Rh_yCr_{2-y}O_3$, or Ni_2P) on conductive substrates were fabricated by dispersing 10 mg of the respective powders in 1 mL of ethanol via sonication for 15-30 minutes. A 0.04 mL aliquot of the suspension was drop-coated onto FTO or Au substrates using a circular mask (38.5 mm^2) made from polyester masking tape, followed by drying under N_2 flow in the

dark for 1 hour. Subsequent layers were added until the desired thickness was achieved. n-GaP particle films were allowed to dry under N_2 flow in the dark and then annealed under argon for 3 hours at 450 °C to confirm good contact with the substrate.

Ni_2P cocatalyst particles of average diameter of 12 nm were prepared via an air free two-step synthesis.[62, 83] All glassware was cleaned and dried overnight in a 60 °C oven before use. In a 50 mL two-necked round bottom flask equipped with a coil condenser 0.50 g (2.0 mmol) $Ni(acac)_2$, 8 mL (25 mmol) dioctyl ether, 3 mL (9 mmol) oleylamine, 6 mL (14 mmol) trioctylphosphine, and a stir bar were combined. The system was purged and refilled with N_2 three times before it was heated to 120 °C with a heating mantle. The system was left under vacuum to remove water and other impurities with low boiling points. The solution was then heated to 220 °C for 1 hour to allow formation of Ni nanoparticles followed by an increase in temperature to 350 °C for 8+ hours to form Ni_2P. The reaction mixture was then cooled slowly to 200 °C before being removed from the heating mantle and cooled to room temperature. The liquid reaction mixture was transferred into centrifuge tubes and separated by centrifuging at 12,500 rpm for 5 min. The black product was then washed with a 1:4 by volume mixture of hexanes and ethanol 5 times and suspended in 12 mL of pure hexanes via sonication for the ligand exchange reaction. The balanced reaction for the synthesis of the dinickel phosphide is 4 $Ni(C_5H_7O_2)_2 + H_2NC_{18}H_{37} + 2\ P(C_8H_{17})_3 \rightarrow 2\ Ni_2P + 6\ C_8H_{16} + HNC_{18}H_{36} + 8\ C_5H_8O_2$.

A 200 mL two-necked round bottom flask was charged with 125 mL of chloroform containing 1.0 g of polyvinylpyrrolidone. The nanoparticle suspension was added, and the system was purged and refilled with nitrogen 5 times. The flask was heated to 65 °C for 10-12 hours using

an oil bath. Once cooled to room temperature, the product was centrifuged out after adding twice the volume of acetone (anti-solvent) to the reaction mixture. A centrifuge speed of 12,500 rpm was needed to separate the majority of the product from the supernatant. The resulting black powder was washed 5 times with acetone and then dried in vacuum. The Ni_2P particles were stored in a glove box until use.

Pt Cocatalyst Loading: Platinum was deposited onto GaP particles by irradiating 200 mg of GaP particles in 100 mL of an aqueous solution of H_2PtCl_6 (1 wt% Pt with respect to GaP) and 20% methanol for 3 hours under illumination from an unfiltered 300 W Xe arc lamp. The solid product was isolated by sedimentation and washed three times with nanopure water, followed by drying in vacuum. The resulting powder was stored in a nitrogen filled glove box in the dark until use.

$Rh_yCr_{2-y}O_3$ Cocatalyst Loading: The co-catalyst was deposited by impregnation/calcination as previously reported. [84] In a small beaker, GaP, $RhCl_3 \cdot xH_2O$ (0.5 wt% Rh), $Cr(NO_3)_3 \cdot 9\ H_2O$ (1 wt% Cr) and 30 mL nanopure water were mixed and heated in an 80 °C water bath with occasional stirring. The resulting powder was collected after 2 h and heated in air at 350 °C for 1 h.

Ni_2P Cocatalyst Loading: The Ni_2P cocatalyst was added to 100 mg of n-GaP to achieve ~4% (mass) loading. The particle mixture was suspended in a few mL of ethanol and sonicated for 15 minutes to disperse the Ni_2P nanoparticles. Next the mixture was transferred to a mortar and ground under air until the ethanol evaporated. The fine and uniform powder was transferred

into a ceramic boat and annealed under argon flow in a tube furnace. The temperature was held at 450 ^{o}C for 3 hours to ensure good contact between the Ni_2P and n-GaP particles.

Scanning electron microscopy (SEM) and energy dispersive X-ray spectroscopy (EDX) of GaP samples and particle films on Au substrate were taken on a Scios DualBeam SEM/FIB instrument. Transmission electron microscopy (TEM) was performed on a a FEI L120C TEM with an accelerating voltage of 80 kV.

Powder X-ray diffraction measurements were performed on a Bruker D8 Advance Eco with a Cu Ka radiation source and monochromatic wavelength of 0.15418 nm. UV-vis diffuse reflectance spectra were recorded on a Thermo Scientific Evolution 220 spectrometer using dried sample films and white Teflon tape as a reference.

X-ray Photoelectron Spectroscopy (XPS) measurements were conducted using a Supra XPS spectrometer using an Al Kα source that generate X-rays at 1,487 eV and using an ultra-high vacuum (UHV) analytical chamber with a pressure of 10^{-7} mbar. The spectra were electrostatically corrected based on the position of C 1s (284.6 eV). Baseline simulation of the core-level spectrum was done using the Shirley method.

Surface photovoltage (SPV) spectra were measured under vacuum (≤ 6.0×10^{-4} mbar) on wafer pieces. A *Besocke* gold Kelvin probe was used as the reference electrode. Samples were illuminated with a 150 W xenon lamp. The light was filtered through an Oriel Cornerstone 130 monochromator to obtain the spectra in the 0.4 – 4.0 eV window (scanning from low to high

energy). Transient SPV data was collected by illumination with a 405 nm LED. All SPV data is referenced against the CPD value in the dark.

Work function measurements were performed in vacuum using a gold Kelvin probe reference electrode that was calibrated with a gold-coated glass substrate. The gold-coated glass substrate was then swapped with particle films of Ni_2P or $Rh_xCr_{2-x}O_3$ on gold-coated glass substrates. The Pt work function was measured from a clean Pt wire electrode coiled tightly and flattened to fit under the Kelvin probe.

Photocatalytic hydrogen evolution reactions (HER) were performed by suspending 50 mg of GaP particles (or 50 mg of cocatalyst modified GaP) in 50 mL of 0.05 M electron donor (unless otherwise stated) in a 100 mL round bottom flask. The reaction flask was purged and refilled with argon 5 times before beginning irradiation. A 300 W Xe arc lamp with a 400 nm long pass filter (0.22 M $NaNO_3$ solution) was used to irradiate the suspension. The lamp intensity was measured to be 380-450 $mW \cdot cm^{-2}$ at the surface of the flask by an IL1400BL photometer equipped with a GaAsP detector for 280 nm to 660 nm sensitivity range. A mirror behind the sample flask was employed to ensure full illumination and a fan was used to maintain a constant temperature of 35 ^oC. The irradiation system was hardwired to a Varian 3800 gas chromatograph with a 60/80 Å molecular sieve column and thermal conductivity detector to identify quantities of H_2, O_2, and N_2 in the flask at various times.

Phosphorus nuclear magnetic resonance (NMR) spectroscopy was performed using a Varian 600 MHz NMR spectrometer and data was analyzed using VnmrJ software. Samples were prepared by centrifuging the solution resulting from HER experiments at 10,000 RPM. The

supernatant was then dried using rotary evaporation and resuspended in D_2O. The solution was filtered into an NMR tube and the P-31 NMR was conducted using manual tuning and 32-64 pulses with and without proton decoupling.

2.6 Supplemental Information

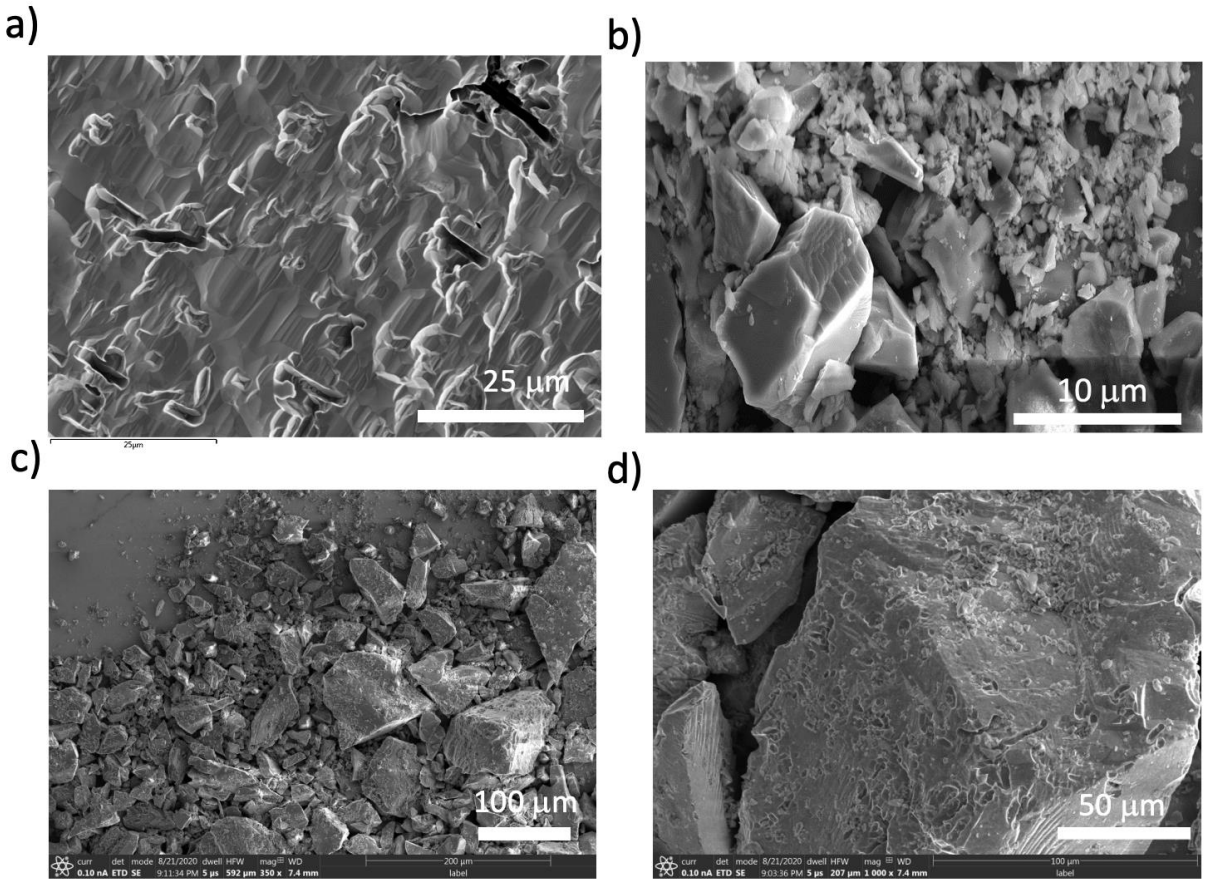

Fig. 2.S1 SEM image of a) non-polished side of etched GaP wafer, and of mechanically ground n-GaP particles, b) before, and c,d) after etching with Piranha acid. Prolonged etching produces small pits and trenches on the surfaces of the larger particles.

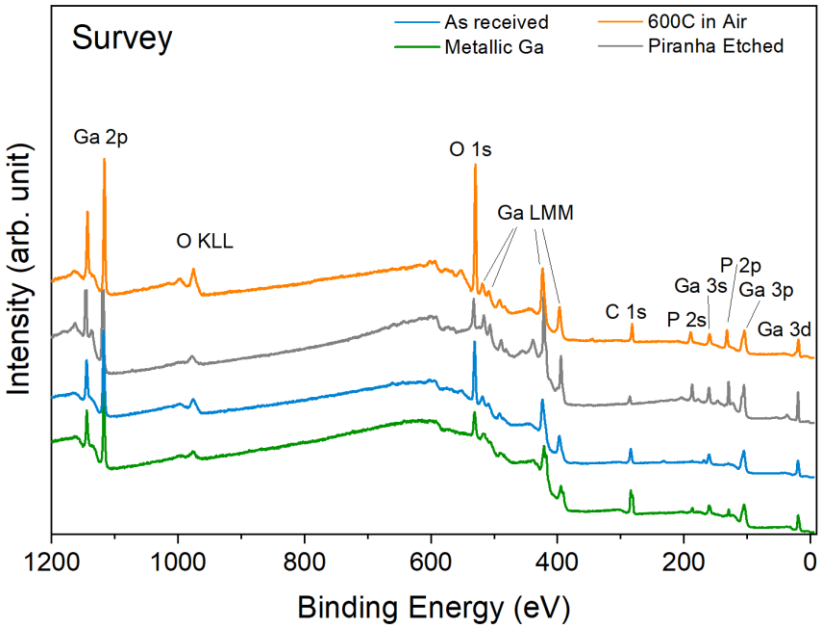

Figure 2.S2 Survey scans of n-GaP wafers.

Table 2.S3 Selected XPS data.

Sample	**Atomic concentration [%]**			
	Ga 2p	P 2p	O 1s	C 1s
As Received	13.3	3.5	47.3	35.8
Piranha Etched	17.6	30.2	38.9	13.4
Metallic Ga	11.4	5.2	17.8	65.7
600 ℃ in Air	11.6	13.1	54.8	20.5

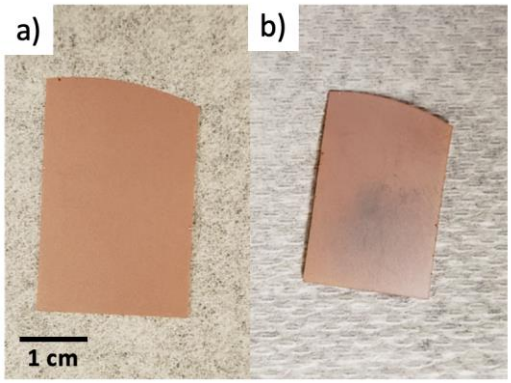

Figure 2.S4 Photos of n-GaP wafer before (a) and after (b) application of gallium metal.

Table 2.S5 Selected XPS data.

Peak name	**Sample peak position (eV)**			
	As Received	Piranha Etched	Metallic Ga	600°C Air Oxidized
Ga^{3+} $3d_{5/2}$	20.22	18.93	19.70	21.39

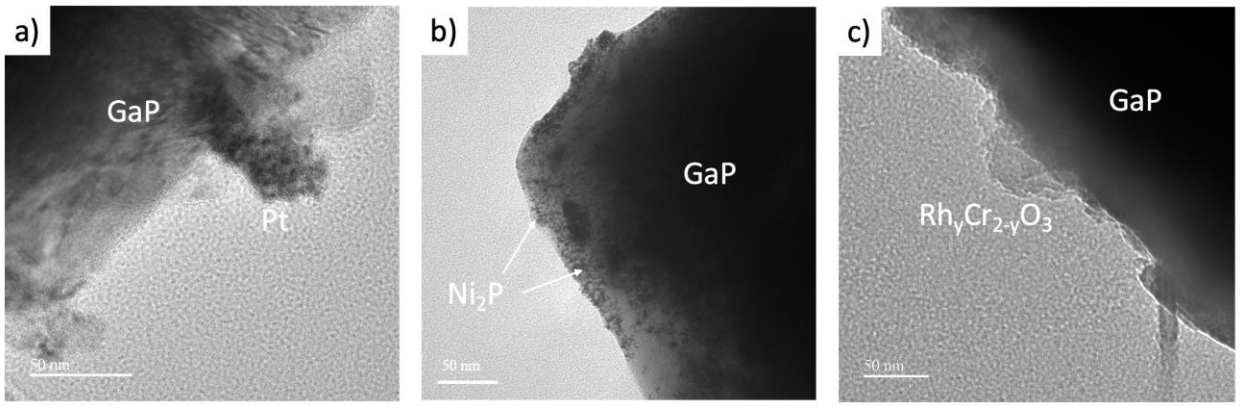

Figure 2.S6 TEM images of a) Pt /GaP, b) Ni_2P/GaP, c) $Rh_yCr_{2-y}O_3$ /GaP.

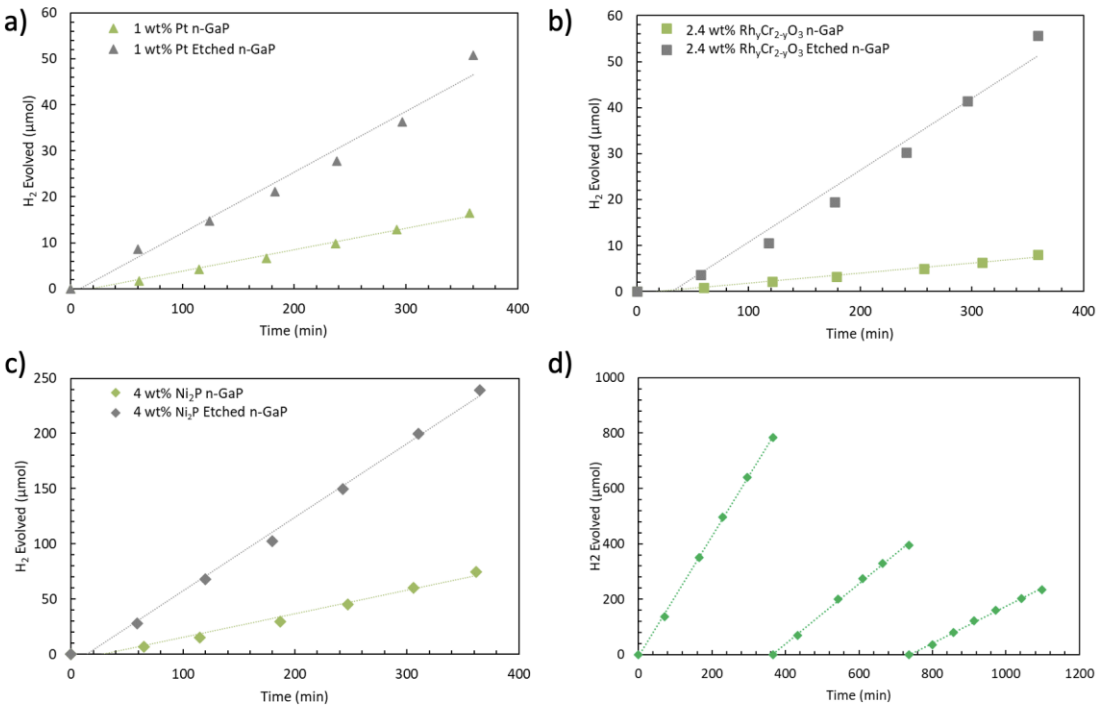

Figure 2.S7 H_2 evolution data from n-GaP before and after removal of surface states. (a) 1% Pt, (b) 2.4% $Rh_yCr_{2-y}O_3$, and (c) 4% Ni_2P electrocatalyst in 50.0 mL of 0.05 M KI in 0.10 M phosphate buffer at pH 7.2 under visible light (l > 400 nm, 300 W Xe arc lamp, 380-450 mW·cm^{-2} irradiance at the flask). (d) H_2 evolution from 4% loaded Ni_2P/ n-GaP (etched) in 50.0 mL of aqueous 0.3 M Na_2S and 0.3 M Na_2SO_3 solution under visible light (l>400 nm, 300 W Xe arc lamp, estimated irradiance at the flask 380-450 mW·cm^{-2}). In between the 6 h experiments, particles were separated from solution and stored in the dark for 10-18 h.

Table 2.S8 Summary of 6 h gas chromatography experiments of cocatalyst loaded n-GaP in 50.0 mL of 0.05 M KI in 0.10 M phosphate buffer at pH 7.2.

Photocatalyst	Mass (mg)	Light Intensity (mW/cm^2)	HER Rate (µmol/h)
Bare n-Gap	48.4	400	0.67
Bare Etched n-GaP	42.6	400	1.12
1% Pt n-GaP	50.3	410	2.61
1% Pt Etched n-GaP	50.2	420	7.69
2.4% $Rh_yCr_{2-y}O_3$ n-GaP	51.9	420	1.34
2.4% $Rh_yCr_{2-y}O_3$ Etched n-GaP	51.3	430	8.26
4% Ni_2P n-GaP	49.9	420	11.41
4% Ni_2P Etched n-GaP	51.0	450	37.90

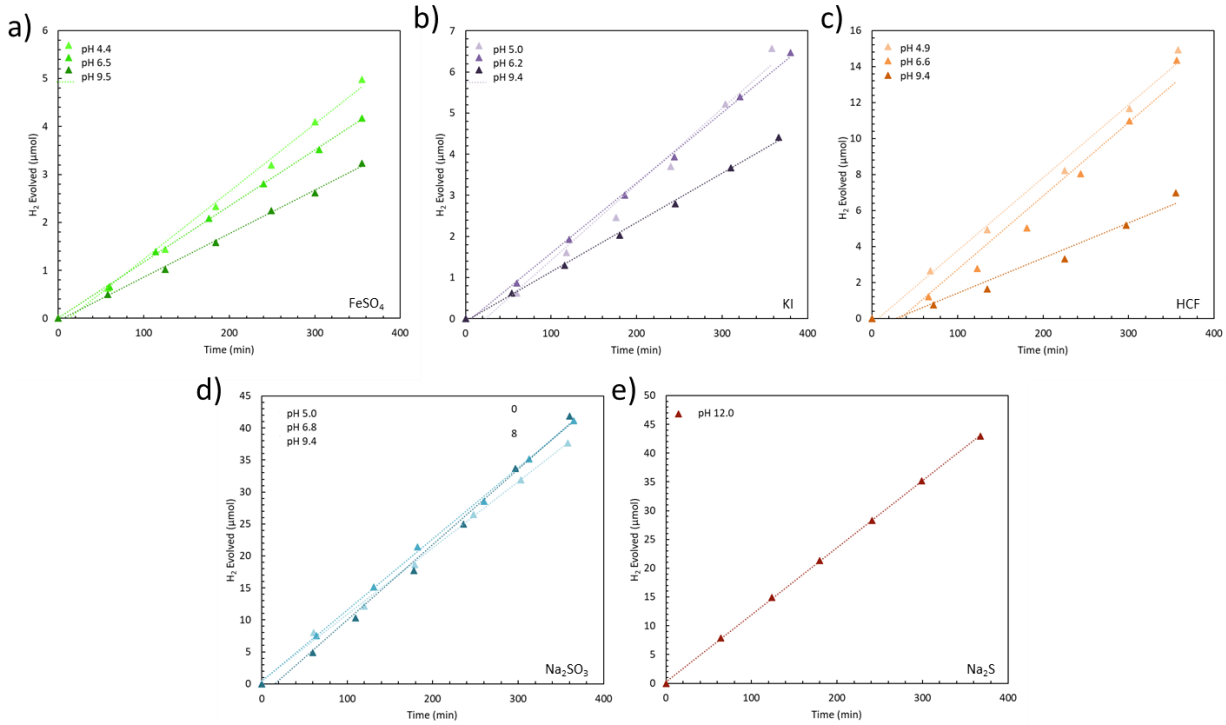

Figure 2.S9 H_2 evolution from of 1% loaded Pt/GaP (etched) in 50.0 mL of 0.05M (a) $FeSO_4$, (b) KI, (c) HCF, (d) Na_2SO_4, and (e) Na_2S at various pH values (adjusted with NaOH or HCl), under visible light (l>400 nm, 300 W Xe arc lamp, irradiance at the flask 380-450 $mW \cdot cm^{-2}$).

Table 2.S10 HER data from Fig. 2.S4 for 1% Pt – n-GaP in 0.5 M of sacrificial reagent solution.

e- donor	E vs NHE (V)	pH	E vs RHE (V)	Light Intensity (mW/cm^2)	HER rate (μmol/h)
$FeSO_4$	0.77	4.4	1.03	490	0.80
KI	0.55	6.2	0.92	540	1.02
HCF	0.36	6.6	0.75	540	2.16
Na_2SO_3	0.17	9.4	0.17	480	6.66
Na_2S	-0.48	12.0	0.06	480	7.06
$FeSO_4$ + NaOH	0.77	6.5	1.15	510	0.70
$FeSO_4$ + NaOH	0.77	9.3	1.32	490	0.53
KI + NaOH	0.55	9.4	1.11	530	0.72
HCF + NaOH	0.36	9.4	0.92	540	1.02
Na_2SO_3 + HCl	0.17	6.8	0.17	540	6.78
KI + HCl	0.55	5.0	0.85	530	1.10
HCF + HCl	0.36	4.9	0.65	520	2.38
Na_2SO_3 + HCl	0.17	5.0	0.17	510	6.36

Table 2.S11 H_2 evolution from 4% loaded Ni_2P/ n-GaP (etched) in 50.0 mL of sulfide / sulfite solution under visible light (l>400 nm, 300 W Xe arc lamp).

Sacrificial Donor	Photocatalyst Mass (mg)	Light Intensity (mW/cm^2)	HER Rate (µmol/h)
0.01 M Na_2S / 0.001 M Na_2SO_3	51.6	540	39.5
0.05 M Na_2S / 0.005 M Na_2SO_3	49.1	550	49.7
0.3 M Na_2S / 0.03 M Na_2SO_3	50.4	540	100.6
0.3 M Na_2S / 0.3 M Na_2SO_3	46.8	520	122.8

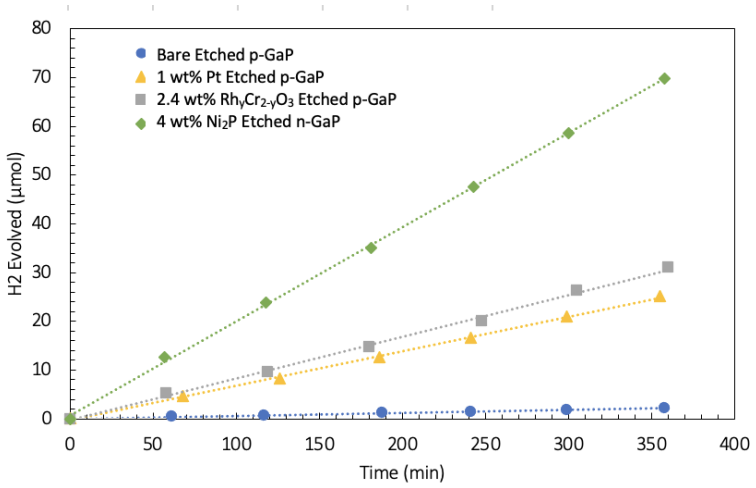

Figure 2.S12 H_2 evolution under 525 nm LED illumination. See data in Table 2.S13.

Table 2.S13 Apparent Quantum efficiencies (AQE) for H_2 evolution from n-GaP photocatalysts under 525 nm LED illumination.

	Bare Etched n-GaP	1 wt% Pt Etched n-GaP	2.4 wt% $Rh_yCr_{2-y}O_3$ Etched n-GaP	4 wt% Ni_2P Etched n-GaP
Wavelength (nm)	525	525	525	525
Energy per photon (J)	3.78E-19	3.78E-19	3.78E-19	3.78E-19
Measured Power (mW/cm^2)	2.16	2.14	2.14	2.14
Corrected Power (mW/cm^2)	2.70	2.68	2.68	2.68
Area (cm^2)	3.84	3.80	3.82	3.76
HER Rate (µmol/h)	0.380	4.19	5.08	11.8
Photons In (1/h)	9.86E+19	9.67E+19	9.72E+19	9.57E+19
Electrons Used (1/h)	4.58E+17	5.04E+18	6.12E+18	1.41E+19
AQE (%)	0.464	5.22	6.29	14.8

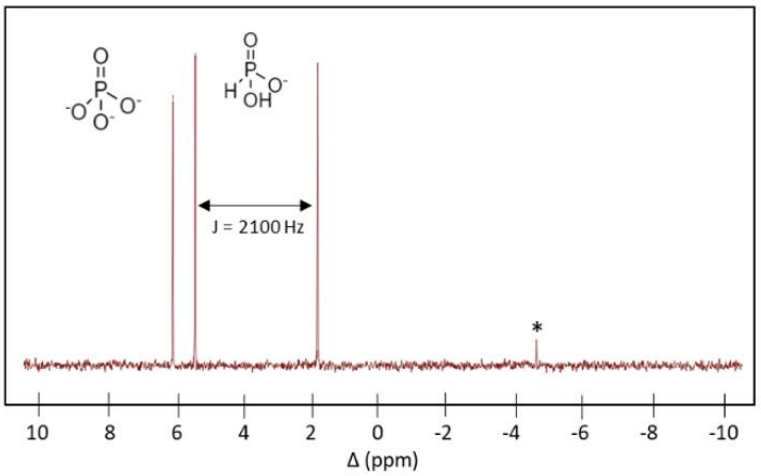

Figure 2.S14 P-31 NMR spectrum of Ni_2P/n-GaP supernatant after 18 hours of illumination in 0.05 M Na_2S and 0.005 M Na_2SO_3 solution. The singlet at 6.2 ppm and the doublet centered at 3.7 ppm are attributed to hydrogen phosphate (HPO_4^-) and phosphite (HPO_3^{2-}), while the asterisk is from diphosphate.

2.7 References

1. Segev, G.; Kibsgaard, J.; Hahn, C.; Xu, Z. J.; Cheng, W.-H.; Deutsch, T. G.; Xiang, C.; Zhang, J. Z.; Hammarström, L.; Nocera, D. G.; Weber, A. Z.; Agbo, P.; Hisatomi, T.; Osterloh, F. E.; Domen, K.; Abdi, F. F.; Haussener, S.; Miller, D. J.; Ardo, S.; McIntyre, P. C.; Hannappel, T.; Hu, S.; Atwater, H.; Gregoire, J. M.; Ertem, M. Z.; Sharp, I. D.; Choi, K.-S.; Lee, J. S.; Ishitani, O.; Ager, J. W.; Prabhakar, R. R.; Bell, A. T.; Boettcher, S. W.; Vincent, K.; Takanabe, K.; Artero, V.; Napier, R.; Cuenya, B. R.; Koper, M. T. M.; Van De Krol, R.; Houle, F., The 2022 solar fuels roadmap. *Journal of Physics D: Applied Physics* **2022,** *55* (32), 323003.

2. Takata, T.; Jiang, J.; Sakata, Y.; Nakabayashi, M.; Shibata, N.; Nandal, V.; Seki, K.; Hisatomi, T.; Domen, K., Photocatalytic water splitting with a quantum efficiency of almost unity. *Nature* **2020,** *581* (7809), 411-414.

3. Fabian, D. M.; Hu, S.; Singh, N.; Houle, F. A.; Hisatomi, T.; Domen, K.; Osterloh, F. E.; Ardo, S., Particle Suspension Reactors and Materials for Solar-Driven Water Splitting. *Energ. & Envi. Sci.* **2015,** *8*, 2825-2850.

4. Nishioka, S.; Osterloh, F. E.; Wang, X.; Mallouk, T. E.; Maeda, K., Photocatalytic water splitting. *Nature Reviews Methods Primers* **2023,** *3* (1), 42.

5. Nozik, A. J., Photochemical Diodes. *Applied Physics Letters* **1977,** *30* (11), 567-569.

6. Kudo, A.; Miseki, Y., Heterogeneous Photocatalyst Materials for Water Splitting. *Chem. Soc. Rev.* **2009,** *38* (1), 253-278.

7. Zhao, Z.; Goncalves, R. V.; Barman, S. K.; Willard, E. J.; Byle, E.; Perry, R.; Wu, Z.; Huda, M. N.; Moulé, A. J.; Osterloh, F. E., Electronic structure basis for enhanced overall water

splitting photocatalysis with aluminum doped $SrTiO_3$ in natural sunlight. *Energy & Environmental Science* **2019,** *12*, 1385-1395.

8. Wang, Q.; Hisatomi, T.; Jia, Q.; Tokudome, H.; Zhong, M.; Wang, C.; Pan, Z.; Takata, T.; Nakabayashi, M.; Shibata, N.; Li, Y.; Sharp, I. D.; Kudo, A.; Yamada, T.; Domen, K., Scalable water splitting on particulate photocatalyst sheets with a solar-to-hydrogen energy conversion efficiency exceeding 1%. *Nat. Mater.* **2016,** *15* ( ), 611–615.

9. Han, R.; Melo Jr, M. A.; Zhao, Z.; Wu, Z.; Osterloh, F. E., Light Intensity Dependence of Photochemical Charge Separation in the $BiVO_4$/Ru-$SrTiO_3$:Rh Direct Contact Tandem Photocatalyst for Overall Water Splitting. *The Journal of Physical Chemistry C* **2020,** *124*, 9724-9733.

10. Bolton, J. R.; Strickler, S. J.; Connolly, J. S., Limiting and Realizable Efficiencies of Solar Photolysis of Water. *Nature* **1985,** *316* (6028), 495-500.

11. Maeda, K.; Domen, K., New non-oxide photocatalysts designed for overall water splitting under visible light. *J. Phys. Chem. C* **2007,** *111* (22), 7851-7861.

12. Xiao, J.; Hisatomi, T.; Domen, K., Narrow-Band-Gap Particulate Photocatalysts for One-Step-Excitation Overall Water Splitting. *Accounts of Chemical Research* **2023,** *56* (7), 878-888.

13. Sivula, K.; van de Krol, R., Semiconducting Materials for Photoelectrochemical Energy Conversion. *Nature Reviews Materials* **2016,** *1*, 15010.

14. Osterloh, F. E., Inorganic Materials as Catalysts for Photochemical Splitting of Water. *Chem. Mater.* **2008,** *20* (1), 35-54.

15. Osterloh, F. E., Inorganic Nanostructures for Photoelectrochemical and Photocatalytic Water Splitting. *Chem. Soc. Rev.* **2013,** *42* (6), 2294-2320.

16. Hisatomi, T.; Kubota, J.; Domen, K., Recent Advances in Semiconductors for Photocatalytic and Photoelectrochemical Water Splitting. *Chem. Soc. Rev.* **2014,** *43* (22), 7520-7535.

17. Wang, X. C.; Maeda, K.; Thomas, A.; Takanabe, K.; Xin, G.; Carlsson, J. M.; Domen, K.; Antonietti, M., A metal-free polymeric photocatalyst for hydrogen production from water under visible light. *Nature Mater.* **2009,** *8* (1), 76-80.

18. Maeda, K.; Teramura, K.; Saito, N.; Inoue, Y.; Domen, K., Photocatalytic overall water splitting on gallium nitride powder. *Bulletin of the Chemical Society of Japan* **2007,** *80* (5), 1004-1010.

19. Kibria, M. G.; Chowdhury, F. A.; Zhao, S.; AlOtaibi, B.; Trudeau, M. L.; Guo, H.; Mi, Z., Visible light-driven efficient overall water splitting using p-type metal-nitride nanowire arrays. *Nat. Commun.* **2015,** *6*, 6797.

20. Shiga, Y.; Umezawa, N.; Srinivasan, N.; Koyasu, S.; Sakai, E.; Miyauchi, M., A metal sulfide photocatalyst composed of ubiquitous elements for solar hydrogen production. *Chem. Commun.* **2016,** *52* (47), 7470-7473.

21. Yoshikuni, T.; Hiroshi, Y.; Hideo, T., Hydrogen evolution on surface-modified silicon powder photocatalysts in aqueous ethanol solutions. *Chemistry Letters* **1983,** *12* (3), 269-272.

22. Sato, J.; Saito, N.; Yamada, Y.; Maeda, K.; Takata, T.; Kondo, J. N.; Hara, M.; Kobayashi, H.; Domen, K.; Inoue, Y., RuO_2-loaded beta-Ge_3N_4 as a non-oxide photocatalyst for overall water splitting. *Journal of the American Chemical Society* **2005,** *127* (12), 4150-4151.

23. Maeda, K.; Saito, N.; Lu, D.; Inoue, Y.; Domen, K., Photocatalytic Properties of RuO_2-Loaded beta-Ge_3N4 for Overall Water Splitting. In *J. Phys. Chem. C*, 2007; Vol. 111, pp 4749-4755.

24. Zhu, X.; Zhang, T.; Sun, Z.; Chen, H.; Guan, J.; Chen, X.; Ji, H.; Du, P.; Yang, S., Black Phosphorus Revisited: A Missing Metal-Free Elemental Photocatalyst for Visible Light Hydrogen Evolution. *Adv. Mater.* **2017,** *29* (17), 1605776.

25. Ohmori, T.; Mametsuka, H.; Suzuki, E., Photocatalytic hydrogen evolution on InP suspension with inorganic sacrificial reducing agent. *International Journal of Hydrogen Energy* **2000,** *25* (10), 953-955.

26. Bessekhouad, Y.; Mohammedi, M.; Trari, M., Hydrogen photoproduction from hydrogen sulfide on Bi2S3 catalyst. *Solar Energy Materials and Solar Cells* **2002,** *73* (3), 339-350.

27. Madelung, O., *Semiconductors: Data Handbook*. 3rd ed.; Springer: Berlin, 2004; p 691 p.

28. Chen, S.; Wang, L.-W., Thermodynamic Oxidation and Reduction Potentials of Photocatalytic Semiconductors in Aqueous Solution. *Chemistry of Materials* **2012,** *24* (18), 3659-3666.

29. Siddiqi, G.; Pan, Z.; Hu, S., Chapter Three - III–V Semiconductor Photoelectrodes. In *Semiconductors and Semimetals*, Mi, Z.; Wang, L.; Jagadish, C., Eds. Elsevier: 2017; Vol. 97, pp 81-138.

30. Ellis, A. B.; Bolts, J. M.; Kaiser, S. W.; Wrighton, M. S., Study of N-Type Gallium Arsenide-Based and Gallium Phosphide-Based Photoelectrochemical Cells - Stabilization by Kinetic Control and Conversion of Optical Energy to Electricity. *Journal of the American Chemical Society* **1977,** *99* (9), 2848-2854.

31. Hu, S.; Shaner, M. R.; Beardslee, J. A.; Lichterman, M.; Brunschwig, B. S.; Lewis, N. S., Amorphous TiO_2 coatings stabilize Si, GaAs, and GaP photoanodes for efficient water oxidation. *Science* **2014,** *344* (6187), 1005-1009.

32. Shen, X.; Zhao, T.; Su, H.; Yang, M.; Chen, J.; Liu, Y.; Yanagi, R.; Solanki, D.; Hu, S., Tuning Intermediate Bands of Protective Coatings to Reach the Bulk-Recombination Limit of Stable Water-Oxidation GaP Photoanodes. *Advanced Energy Materials* **2022,** *12* (29), 2201314.

33. Strandwitz, N. C.; Turner-Evans, D. B.; Tamboli, A. C.; Chen, C. T.; Atwater, H. A.; Lewis, N. S., Photoelectrochemical Behavior of Planar and Microwire-Array Si|GaP Electrodes. *Advanced Energy Materials* **2012,** *2* (9), 1109-1116.

34. Standing, A.; Assali, S.; Gao, L.; Verheijen, M. A.; van Dam, D.; Cui, Y.; Notten, P. H. L.; Haverkort, J. E. M.; Bakkers, E. P. A. M., Efficient water reduction with gallium phosphide nanowires. *Nat. Commun.* **2015,** *6*, 7824.

35. Krawicz, A.; Cedeno, D.; Moore, G. F., Energetics and efficiency analysis of a cobaloxime-modified semiconductor under simulated air mass 1.5 illumination. *Physical Chemistry Chemical Physics* **2014,** *16* (30), 15818-15824.

36. Malizia, M.; Seger, B.; Chorkendorff, I.; Vesborg, P. C. K., Formation of a p–n heterojunction on GaP photocathodes for H_2 production providing an open-circuit voltage of 710 mV. *J. Mater. Chem. A* **2014,** *2* (19), 6847-6853.

37. Nozik, A. J., P-N Photoelectrolysis Cells. *Applied Physics Letters* **1976,** *29* (3), 150-153.

38. Halmann, M., Photoelectrochemical reduction of aqueous carbon dioxide on p-type gallium phosphide in liquid junction solar cells. *Nature* **1978,** *275* (5676), 115-116.

39. Barton, E. E.; Rampulla, D. M.; Bocarsly, A. B., Selective solar-driven reduction of CO_2 to methanol using a catalyzed p-GaP based photoelectrochemical cell. *Journal of the American Chemical Society* **2008,** *130* (20), 6342-+.

40. Lee, S.; Bielinski, A. R.; Fahrenkrug, E.; Dasgupta, N. P.; Maldonado, S., Macroporous p-GaP Photocathodes Prepared by Anodic Etching and Atomic Layer Deposition Doping. *ACS Appl. Mater. Interfaces* **2016,** *8* (25), 16178-16185.

41. Gronet, C. M.; Lewis, N. S., Design of a 13% efficient n-$GaAs_{1-x}P_x$ semiconductor–liquid junction solar cell. *Nature* **1982,** *300* (5894), 733-735.

42. Sun, J. W.; Liu, C.; Yang, P. D., Surfactant-Free, Large-Scale, Solution-Liquid-Solid Growth of Gallium Phosphide Nanowires and Their Use for Visible-Light-Driven Hydrogen Production from Water Reduction. *Journal of the American Chemical Society* **2011,** *133* (48), 19306-19309.

43. Zhao, Z.; Willard, E. J.; Dominguez, J. R.; Wu, Z.; Osterloh, F. E., Depletion layer controls photocatalytic hydrogen evolution with p-type gallium phosphide particles. *Journal of Materials Chemistry A* **2019,** *7* (30), 18020-18029.

44. Garnett, E. C.; Yang, P. D., Silicon nanowire radial p-n junction solar cells. *J. Am. Chem. Soc.* **2008,** *130* (29), 9224-+.

45. Spitzer, W. G.; Gershenzon, M.; Frosch, C. J.; Gibbs, D. F., Optical absorption in n-type gallium phosphide. *J. Phys. Chem. Solids* **1959,** *11* (3), 339-341.

46. Lacey, S. D., The absorption coefficient of gallium phosphide in the wavelength region 530 to 1100 nm. *Solid State Communications* **1970,** *8* (14), 1115-1118.

47. Dean, P. J.; Henry, C. H., Electron-Capture ("Internal") Luminescence from the Oxygen Donor in Gallium Phosphide. *Physical Review* **1968,** *176* (3), 928-937.

48. Kronik, L.; Shapira, Y., Surface Photovoltage Phenomena: Theory, Experiment, and Applications. *Surf. Sci. Rep.* **1999,** *37* (1-5), 1-206.

49. Daemi, S.; Kaushik, S.; Das, S.; Hamann, T. W.; Osterloh, F. E., BiVO4–Liquid Junction Photovoltaic Cell with 0.2% Solar Energy Conversion Efficiency. *J. Am. Chem. Soc.* **2023,** *145* (47), 25797-25805.

50. Cheng, Y.; Xiao, C.; Mahmoudi, B.; Scheer, R.; Maijenburg, A. W.; Osterloh, F. E., Effect of charge selective contacts on the quasi Fermi level splitting of $CuGa_3Se_5$ thin film photocathodes for hydrogen evolution and methylviologen reduction. *EES Catalysis* **2023,** *1*, 74-83.

51. Daemi, S.; Kundmann, A.; Cendula, P.; Becker, K.; Osterloh, F. E., Contactless Measurement of Photovoltage in $BiVO_4$ Photoelectrodes. *Energy Environ. Sci.* **2023,** *16*, 4530-4538.

52. Romanyuk, O.; Gordeev, I.; Paszuk, A.; Supplie, O.; Stoeckmann, J. P.; Houdkova, J.; Ukraintsev, E.; Bartoš, I.; Jiříček, P.; Hannappel, T., GaP/Si(0 0 1) interface study by XPS in combination with Ar gas cluster ion beam sputtering. *Applied Surface Science* **2020,** *514*, 145903.

53. Mukherjee, J.; Erickson, B.; Maldonado, S., Physicochemical and Electrochemical Properties of Etched GaP(111)A and GaP(111)B Surfaces. *J. Electrochem. Soc.* **2010,** *157* (4), H487.

54. Liu, Z.; Höfft, O.; Endres, F., Disproportionation Reaction of Gallium during Electrodeposition from an Ionic Liquid, Monitored by In Situ Electrochemical XPS. *The Journal of Physical Chemistry C* **2021,** *125* (44), 24589-24595.

55. Barr, T. L.; Klinowski, J.; He, H.; Albert, K.; Müller, G.; Lercher, J. A., Evidence for strong acidity of the molecular sieve cloverite. *Nature* **1993,** *365* (6445), 429-431.

56. Doughty, R. M.; Hodges, B.; Dominguez, J.; Han, R.; Zhao, Z.; Assavachin, S.; Osterloh, F. E., Fermi Level Pinning Controls Band Bending and Photochemical Charge Separation in Particles of n-$SrTiO_3$, n-$SrTiO_3$:Al, and n-GaAs:Te. *The Journal of Physical Chemistry C* **2020,** *124* (34), 18426-18435.

57. Yang, Y.; Wang, J.; Zhao, J.; Nail, B. A.; Yuan, X.; Guo, Y.; Osterloh, F. E., Photochemical Charge Separation at Particle Interfaces: The n-$BiVO_4$–p-Silicon System. *ACS Appl. Mater. & Interfaces* **2015,** *10* (7), 5959–5964.

58. Doughty, R. M.; Chowdhury, F. A.; Mi, Z.; Osterloh, F. E., Surface photovoltage spectroscopy observes junctions and carrier separation in gallium nitride nanowire arrays for overall water-splitting. *The Journal of Chemical Physics* **2020,** *153* (14), 144707.

59. Sze, S. M., *Semiconductor devices, physics and technology*. 2nd ed.; Wiley: New York, 2002; p viii, 564 p.

60. Dittrich, T., *Materials concepts for solar cells*. Imperial College Press: London, 2015; p 516 pages (Page 197).

61. Jakubec, I.; Vondrak, J.; Bludska, J.; Pekarek, L., Effect of the crystallographic orientation on photovoltaic properties of p-GaP electrodes. *Collection of Czechoslovak Chemical Communications* **1998,** *63* (1), 75-84.

62. Popczun, E. J.; McKone, J. R.; Read, C. G.; Biacchi, A. J.; Wiltrout, A. M.; Lewis, N. S.; Schaak, R. E., Nanostructured Nickel Phosphide as an Electrocatalyst for the Hydrogen Evolution Reaction. *Journal of the American Chemical Society* **2013,** *135* (25), 9267-9270.

63. Trasatti, S., Work Function, Electronegativity, and Electrochemical Behavior of Metals 3. Electrolytic Hydrogen Evolution in Acid Solutions. *J. Electroanal. Chem.* **1972,** *39* (1), 163-184.

64. McCrory, C. C. L.; Jung, S.; Ferrer, I. M.; Chatman, S. M.; Peters, J. C.; Jaramillo, T. F., Benchmarking Hydrogen Evolving Reaction and Oxygen Evolving Reaction Electrocatalysts for Solar Water Splitting Devices. *J. Am. Chem. Soc.* **2015,** *137* (13), 4347-4357.

65. Maeda, K.; Teramura, K.; Lu, D. L.; Takata, T.; Saito, N.; Inoue, Y.; Domen, K., Characterization of Rh-Cr mixed-oxide nanoparticles dispersed on $(Ga_{1-x}Zn_x)(N_{1-x}O_x)$ as a cocatalyst for visible-light-driven overall water splitting. *J. Phys. Chem. B* **2006,** *110* (28), 13753-13758.

66. Yoshida, M.; Takanabe, K.; Maeda, K.; Ishikawa, A.; Kubota, J.; Sakata, Y.; Ikezawa, Y.; Domen, K., Role and Function of Noble-Metal/Cr-Layer Core/Shell Structure Cocatalysts for Photocatalytic Overall Water Splitting Studied by Model Electrodes. *J. Phys. Chem. C* **2009,** *113* (23), 10151-10157.

67. Michaelson, H. B., Electron Work Function of the Elements. In *CRC Handbook of Chemistry and Physics*, 88 (Internet Version 2008) ed.; Lide, D. R., Ed. CRC Press/Taylor and Francis: Boca Raton, FL, 2008.

68. Liu, X.-t.; Li, B.-h.; Wang, X.-j.; Li, Y.-l.; Zhao, J.; Li, Y.-p.; Li, F.-t., Enhanced Schottky Effect in the Ni2P Cocatalyst via Work Function Up-Shift Induced by MoO2 for Boosting Photocatalytic Hydrogen Evolution. *ACS Sustainable Chemistry & Engineering* **2022,** *10* (32), 10627-10640.

69. Chassé, T.; Theis, W.; Chen, T. P.; Evans, D. A.; Horn, K.; Pettenkofer, C.; Jaegermann, W., Interface chemistry and band bending induced by Pt deposition onto GaP(110). *Surface Science* **1991,** *251-252*, 472-477.

70. Yang, Y.; Gu, J.; Young, J. L.; Miller, E. M.; Turner, J. A.; Neale, N. R.; Beard, M. C., Semiconductor interfacial carrier dynamics via photoinduced electric fields. *Science* **2015,** *350* (6264), 1061-1065.

71. Mayer, J. M., Proton-coupled electron transfer: A reaction chemist's view. *Annual Review of Physical Chemistry* **2004,** *55*, 363-390.

72. Osterloh, F. E., Photocatalysis versus Photosynthesis: A Sensitivity Analysis of Devices for Solar Energy Conversion and Chemical Transformations. *ACS Energy Letters* **2017**, 445-453.

73. Abe, R., Recent Progress on Photocatalytic and Photoelectrochemical Water Splitting under Visible Light Irradiation. *J. Photoch. Photobio. C* **2010,** *11* (4), 179-209.

74. Kumagai, H.; Minegishi, T.; Moriya, Y.; Kubota, J.; Domen, K., Photoelectrochemical Hydrogen Evolution from Water Using Copper Gallium Selenide Electrodes Prepared by a Particle Transfer Method. *J. Phys. Chem. C* **2014,** *118* (30), 16386-16392.

75. Sasaki, Y.; Nemoto, H.; Saito, K.; Kudo, A., Solar Water Splitting Using Powdered Photocatalysts Driven by Z-Schematic Interparticle Electron Transfer without an Electron Mediator. *J. Phys. Chem. C* **2009,** *113* (40), 17536-17542.

76. Chen, S.; Vequizo, J. J. M.; Pan, Z.; Hisatomi, T.; Nakabayashi, M.; Lin, L.; Wang, Z.; Kato, K.; Yamakata, A.; Shibata, N.; Takata, T.; Yamada, T.; Domen, K., Surface Modifications of $(ZnSe)_{0.5}(CuGa_{2.5}Se_{4.25})_{0.5}$ to Promote Photocatalytic Z-Scheme Overall Water Splitting. *Journal of the American Chemical Society* **2021,** *143* (28), 10633-10641.

77. Buhler, N.; Meier, K.; Reber, J. F., Photochemical Hydrogen-Production with Cadmium-Sulfide Suspensions. *J. Phys. Chem.* **1984,** *88* (15), 3261-3268.

78. Yi-Chun, H.; Zhao-Chun, Z.; Hui-Yi, J., Photocatalytic Properties of Pt/GaP Nanoparticles under Visible Light Irradiation. *Journal of Inorganic Materials* **2011,** *26* (6), 579-584.

79. Dang, H. V.; Wang, Y. H.; Wu, J. C. S., Exploration of photocatalytic seawater splitting on Pt/GaP-C_3N_4 under simulated sunlight. *Applied Surface Science* **2022,** *572*, 151346.

80. Dang, H. V.; Wang, Y. H.; Wu, J. C. S., Z-scheme photocatalyst Pt/GaP-TiO_2-SiO_2:Rh for the separated H2 evolution from photocatalytic seawater splitting. *Applied Catalysis B: Environmental* **2021,** *296*, 120339.

81. Meek, R. L.; Schumaker, N. E., Anodic Dissolution and Selective Etching of Gallium Phosphide. *Journal of The Electrochemical Society* **1972,** *119* (9), 1148.

82. Memming, R.; Schwandt, G., Electrochemical properties of gallium phosphide in aqueous solutions. *Electrochimica Acta* **1968,** *13* (6), 1299-1310.

83. Cao, S.; Chen, Y.; Wang, C.-J.; He, P.; Fu, W.-F., Highly efficient photocatalytic hydrogen evolution by nickel phosphide nanoparticles from aqueous solution. *Chem. Commun.* **2014,** *50* (72), 10427-10429.

84. Maeda, K.; Teramura, K.; Masuda, H.; Takata, T.; Saito, N.; Inoue, Y.; Domen, K., Efficient Overall Water Splitting under Visible-Light Irradiation on ($Ga_{1-x}Zn_x$)($N_{1-x}O_x$) Dispersed with Rh−Cr Mixed-Oxide Nanoparticles: Effect of Reaction Conditions on Photocatalytic Activity. *J. Phys. Chem. B* **2006,** *110* (26), 13107-13112.

Chapter 3 – How kinetics and thermodynamics control the energy conversion efficiency of a Gallium phosphide (GaP) solar hydrogen photocathode

Submitted to J. Phys. Chem. C

3.1 Abstract

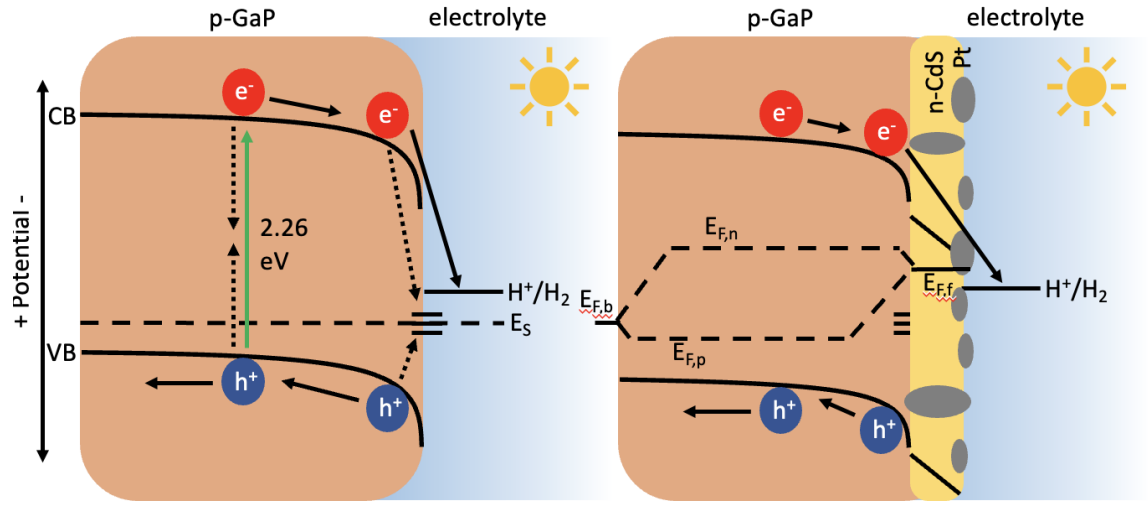

Figure 3.1: The study reveals how the photovoltage and photocurrent of p-GaP photoelectrodes is affected by an CdS passivation layer, added Pt cocatalyst, altered electrolyte composition, and added H_2 and O_2.

P-type gallium phosphide (p-GaP) photocathodes for H_2 evolution from water have a theoretical energy conversion efficiency of 12 % based on the 2.4 eV optical band gap of the material. The performance of actual GaP photocathodes is much lower, for reasons not entirely clear. Here we use surface photovoltage (SPV), open circuit potential (OCP) measurements, and

photoelectrochemical (PEC) experiments to evaluate the kinetic and thermodynamic factors that control energy conversion with p-GaP photocathodes for the hydrogen evolution reaction (HER). We find that the open circuit photovoltage of the bare GaP-H_2O junction is limited by Fermi level pinning from surface states and that an CdS overlayer can passivate these surface defects and increase both photovoltage and photocurrent due to formation of a n-p-junction. An optimized p-GaP/n-CdS/Pt photocathode drives hydrogen evolution with a quantum efficiency of 62 % at 0.0 V RHE and an open circuit photovoltage of 0.43 V at 250 mW/cm^2 (400 nm). The Pt cocatalyst increases the photocurrent due to improve HER kinetics but reduces the photovoltage by promoting recombination. Added H_2 or O_2 control the photovoltage by modifying the electrostatic barrier (band bending) in GaP. This establishes the p-GaP/n-CdS/Pt/H_2O photocathode as an "adaptive junction" whose power conversion depends on the built-in potential at the GaP surface/interface. The implications for the design of hydrogen evolution photocatalysts are discussed.

3.1 Introduction

Solar water splitting provides a potential avenue to carbon free fuels.[1, 2] Highest performances have been achieved by buried junction or photovoltaic/electrolyzer devices,[3, 4] where photovoltage generation and water redox reactions occur in different parts of the device. Semiconductor-liquid junctions generally have lower efficiency,[5, 6] because the junctions have to perform charge separation and multistep redox reactions simultaneously. The trapped charges not only degrade the junctions but also often corrode the semiconductors.[7] Only very few semiconductors are stable and efficient under the corrosive conditions of the water splitting process.[8] This includes the 9.2% efficient InGaN/GaN nanowire array which is protected by a

corrosion resistant N enriched surface layer.[9] Also, $BiVO_4$:Mo photoanodes for water oxidation also have shown long term operation[10] and high efficiency in combination with WO_3.[11, 12] High stability is seen for Al-doped $SrTiO_3$, although this comes at the expense of low conversion efficiency resulting from the large band gap.[13, 14]

GaP is a III-V semiconductor with a zinc-blend crystal structure and a conduction band edge approximately -1.2 V relative to the proton reduction potential.[7, 15] Based on its bandgap of 2.26 eV[15] GaP has a theoretical maximum STH efficiency of 12 %. We recently demonstrated that n-GaP photocatalyst particles can generate H_2 from solution with up to 14.8% quantum efficiency (525 nm).[16] However, p-type GaP photocathodes for hydrogen evolution typically have modest hydrogen evolution rates[17-19] although nanostructured GaP achieves and efficiency of up to 2.9%.[20] GaP photoelectrodes also suffer from significant corrosion in aqueous solutions[20] requiring metal oxide passivation layers,[19, 21-23] or covalent surface modifications for protection.[24]

Here we show for the first time that the performance and stability of p-GaP photocathodes can be improved by chemical bath deposition of CdS overlayers followed by photodeposition of Pt cocatalysts. Surprisingly the photocurrent and photovoltage of the device depend sensitively on the chemical composition of the electrolyte. This characterizes the GaP/CdS/Pt photoelectrodes as an adaptive junction.[25, 26] While the thermodynamics of the junction control the photovoltage, the photocurrent is primarily affected by the kinetics of the charge transfer processes. Optimized GaP photocathodes and photocatalysts for hydrogen evolution need to balance the thermodynamic and kinetic influences.

3.3 Results and Discussion

GaP electrodes were fabricated by cutting a commercial Zn doped GaP wafer (carrier density of 6.8×10^{17} cm^{-3}) into 1×2 cm^2 pieces and by etching it for 10 mins with Piranha acid. Electric contact was established with a Cu metal clip to both sides of the wafer. All measurements/ modifications were performed on the rough side of the wafer after masking the polished side with polyester tape. In assessing the performance of the electrode, we focus on the open circuit photovoltage V_{Ph} as the principal measure of the maximum possible electric energy output. V_{Ph} given by the difference between the Fermi levels at the front and back of the illuminated photoelectrode (Fig. 3.1 and Eq. 3.1) at zero current.[27, 28]

$$V_{Ph} = E_{F,front} - E_{F,back} \qquad \text{(Equation 3.1)}$$

According to Eq. 3.2, a PEC scan of the illuminated electrode yields the open circuit photovoltage from the difference of the photocurrent onset potential E_{On}(light) and the electrochemical potential E^0(Ox/Red) of the corresponding redox couple. This method is used often[29, 30] but its disadvantage is that the identity of the redox couple is not always clear (e.g. in the presence of multiple charge transfer processes, cocatalysts,[26] photocorrosion, or Fermi level pinning[31]), which can make E^0 ill-defined.

$$V_{Ph}(PEC) = E_{On}(light) - E^0(Ox/Red) \qquad \text{(Equation 3.2)}$$

$$V_{Ph}(OCP) = OCP(light) - OCP(dark) \qquad \text{(Equation 3.3)}$$

$$V_{Ph}(SPV) = SPV = CPD(light) - CPD(dark) \qquad \text{(Equation 3.4)}$$

Eq. 3.3 provides the open circuit photovoltage as the difference of the open circuit potentials in the dark and under illumination. This method is commonly used in the literature.[32-

[35] However, it assumes that $E_{F,f}$, the electrochemical potential at the electrode front, remains constant when the light is turned on, which may be the case for fast redox couples, but not for slow ones, which require a kinetic overpotential. As we showed recently, the open circuit photovoltage can also be obtained from surface photovoltage (SPV) data. SPV data is measured using a vibrating Kelvin probe that detects the contact potential difference (CPD) of the sample with regard to a gold reference. The SPV signal corresponds to the light-induced change of the CPD (Eq. 4). For semiconductors in electrochemical equilibrium with their adjacent phases, the SPV equals the open circuit photovoltage V_{Ph}(SPV).[27, 28, 36] As will be demonstrated in the following, V_{Ph}(SPV) is the most reliable assessment of V_{Ph}. In combination with Eq. 1 it provides the absolute electrochemical potential $E_{F,f}$ at the front of the GaP photoelectrode as a function of the light intensity. Values for $E_{F,f}$ are not directly accessible through standard OCP and PEC measurements, but it can be obtained experimentally with added electrodes.[29, 37] The photoelectrochemical properties of the etched p-GaP wafer in 0.1 M H_2SO_4 (pH of 0.9) and in the presence of N_2 are shown in Fig. 3.2 and Table 1.

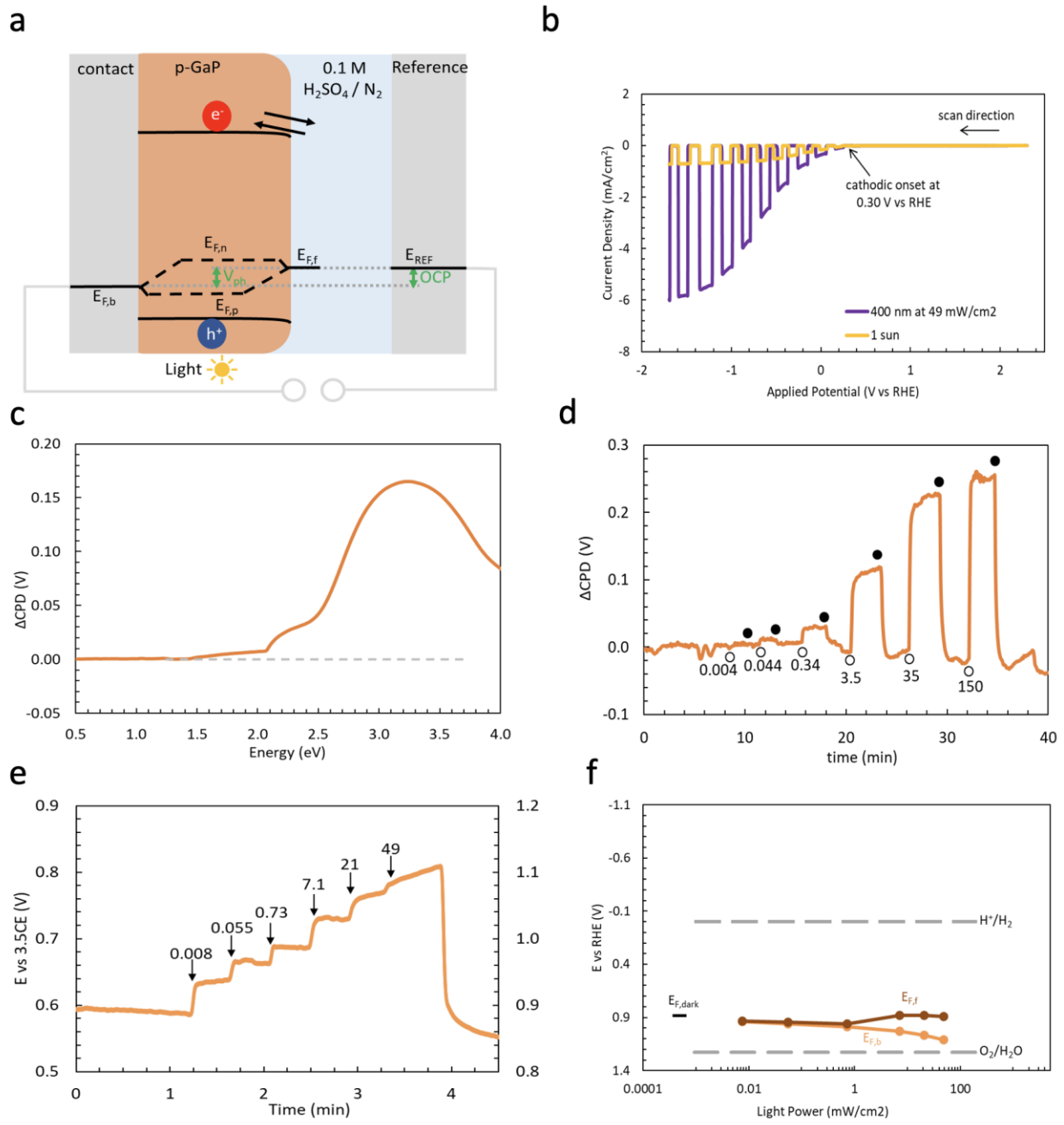

Figure 3.2: p-GaP in aqueous H_2SO_4 at pH 0.9 under N_2 flow. (a) Illuminated Junction. (b) Linear sweep voltammetry scans under chopped 1 sun or 400 nm (49 mW/cm^2) illumination. Repeat scans are shown in Fig. 3.S1a. (c) Surface photovoltage spectrum under monochromatic Xe lamp illumination (0.1-1.0 mW/cm^2) in 0.1M H_2SO_4 and N_2 flow. The discontinuities at 1.28 and 2.07 eV are from optical filter changes. (d) Surface photovoltage under intermittent illumination from 405

nm LED (irradiance in mW/cm^2). (e) Open circuit potential under intermittent illumination from 400 nm LED (irradiance in mW/cm^2). (f) Fermi level diagrams constructed by using the OCP as the $E_{F,b}$ and the max ΔCPD as the difference between $E_{F,b}$ and $E_{F,f}$.

Under simulated 1 sun illumination, the p-GaP wafer produces a cathodic photocurrent of -0.16 mA/cm^2 at 0 V vs RHE with a photocurrent onset of 0.30 V vs. RHE. LED illumination at 400 nm produces a slightly higher photocurrent of mA/cm^2 corresponding to a photon-to-current-conversion efficiency (IPCE) of 2.53 %. Repeat scans (Fig. 3.S1a) show a ~50% decrease in photocurrent and cathodic shift of the onset potential, indicating electrode degradation during PEC. This is not surprising considering the positive cathodic corrosion potential of GaP (0.25 V RHE).[7] This competing reduction reaction makes it impossible to determine the nature of the Faraday process or the photovoltage from the PEC scan in Fig. 3.2b. Hydrogen evolution is not obvious as there is no detectable gas evolution at the electrode. In order to independently measure the photovoltage, surface photovoltage (SPV) spectra were recorded for p-GaP immersed in a 0.1 M H_2SO_4 (wet N_2 atmosphere), using the liquid SPV configuration described previously and shown in Fig. 3.S2.[27, 28, 36] According to Fig. 3.2c, a positive photovoltage begins at 2.06 eV which is near the optical band gap (2.18 eV) of the wafer (see diffuse reflectance spectrum in Fig. 3.S3). The largest SPV signal of 0.16 V occurs at 3.28 eV, where the intensity from the Xe emission is at maximum. The photovoltage spectrum is similar to earlier observations[38] and can be attributed to charge separation under GaP band gap excitation, as shown in Fig. 3.2a. Here the photoelectrons move towards the GaP surface where the Kelvin probe is located, and photoholes move to the back of the wafer. During the SPV scan in Fig. 3.2c, V_{Ph}(SPV) is limited by the low light intensity from the monochromator (1-2 mW/cm^2). To obtain V_{Ph}(SPV) with higher irradiance, SPV

scans were recorded with intermittent illumination from a 405 nm LED (Fig. 3.2d). Reversible SPV signals form and decay on the 10 s times scale. This is fast in comparison to metal oxide films, where generation and decay can occur on the 600 s timescale.[39, 40] The fast dynamics are attributed to the better mobility of charge carriers in GaP.[15] The SPV signals show a linear dependence on the logarithmic light intensity (Fig. 3.S5a) as expected from the diode equation for an ideal junction. However, under 150 mW/cm^2, the photovoltage reaches only 0.26 V, equal to ~10% of the band gap of the material, suggesting severe electron hole recombination. The recombination rate can be estimated from the minimum irradiance required to produce the SPV signal (0.34 mW/cm^2 in Fig. 3.3c). At this threshold intensity, charges recombine as quickly as they are generated. Based on the photon flux F_q from the LED, the charge carrier recombination rate R equals $R = F_q = 6.9 \times 10^{14}$ s^{-1} cm^{-2}.

Next, the electrochemical potential $E_{F,b}$ at the backside of the GaP electrode was obtained from the open circuit potential (OCP) of the working electrode versus the reference electrode (Fig. 3.2e). In the dark, E_{Fb} = 0.88 V vs RHE and appears to be controlled by the E_F of p-GaP (~1.0 V vs RHE, see Fig. 3.S6). Under illumination, $E_{F,b}$ moves to more oxidizing values, in support of the charge separation direction shown in Fig. 3.2a. Based on the potential variation $E_{F,b}$ (light) - $E_{F,b}$(dark), the OCP photovoltage V_{Ph}(OCP) can be estimated as 0.23 V at 49 mW/cm^2. This agrees well with V_{Ph}(SPV) = 0.22 V at 35 mW/cm^2. Using Eq. 1, the Fermi level $E_{F,f}$ at the GaP front can be calculated for each irradiation condition. The data is plotted in Fig. 3.2f. In the dark, the single E_F value appears to be controlled by the work function of GaP (0.99 V, Fig. 3.S6). For this zinc-doped wafer (carrier density 6.8×10^{17} cm^{-3}), E_F is expected 0.2 – 0.3 V above the GaP valence band edge (1.1 V RHE).[7] Under illumination, $E_{F,b}$ moves to oxidizing potentials with increasing

light intensity, whereas $E_{F,f}$ remains near the dark Fermi level. This confirms that the reducing ability of the photocathode is limited, and that no electron transfer to the solution can take place due to the lack of suitable electron acceptors at this potential. That means that photogenerated electrons either recombine or become trapped in surface states. Our previous study on n-GaP shows that surface oxides and Ga(3+) form states 1.8 and 1.3 eV, respectively, below the GaP conduction band edge.[16] These states likely are responsible for the poor photocathode performance. Overall, the data in Fig. 3.2 shows a severely degraded photocathode function for the n-GaP/H_2O(N_2) interface.

Next, to evaluate the effect of a Pt cocatalyst on the performance of a bare GaP photocathode, Pt nanoparticles were grown on the GaP wafer by photoelectrodeposition (Fig. 3.S6). The photoelectrochemical properties of the p-GaP/Pt electrode in 0.1 M H_2SO_4 in N_2 atmosphere are summarized in Fig. 3.3.

The addition of Pt moves the cathodic onset potential in cathodic direction, corresponding to an improved photovoltage of V_{Ph}(PEC) = 0.55 V (Fig. 3.3b). The photocurrent reaches 3.8 mA/cm^2 at 0 V vs RHE resulting in a much-improved incident photon to current efficiency of 24.0 % under 400 nm illumination. At low light intensities, the photovoltage (ΔCPD) is very small, and reduced by either from shading effect decreasing the number of photons reaching the p-GaP absorber layer, or from increased electron-hole recombination at the GaP/Pt contact. Based on the zero SPV at 4 mW/cm^2 (O), the electron hole recombination rate would be estimated as < 9.0 × 10^{13} s^{-1} cm^{-2}. Indeed, there are sub-bandgap states seen in the SPV spectrum in Fig. 3.3c in the 1.2-2.0 eV range, while the bandgap is unchanged at 2.06 eV. The SPV signal increases with

illumination intensity (Fig. 3.3d), and again drift in the baseline reveals electron trapping at the GaP/Pt surface.

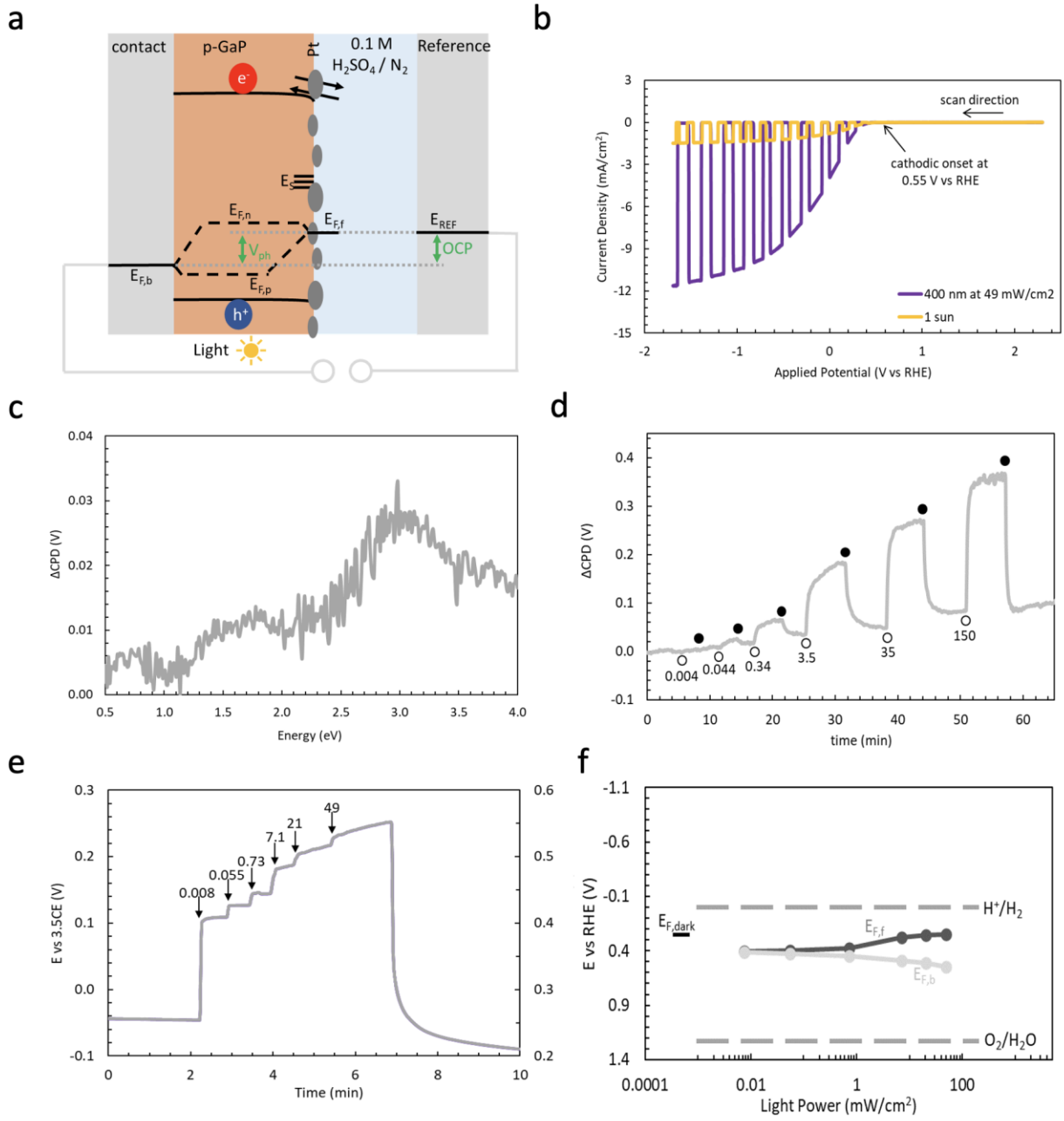

Figure 3.3: p-GaP/Pt in aqueous H_2SO_4 at pH 1.0 under N_2 flow. (a) Junction scheme under illumination. (b) Linear sweep voltammetry scans under chopped illumination. (c) Surface photovoltage spectra under monochromatic Xe lamp illumination. (d) Intensity dependent

surface photovoltage from a 405 nm LED displayed in mW/cm^2. (e) Intensity dependent open circuit potential from a 400 nm LED displayed in mW/cm^2. (f) Fermi level diagrams constructed by using the OCP as the $E_{F,b}$ and the max ΔCPD as the difference between $E_{F,b}$ and $E_{F,f}$..

Open circuit potential measurements place the GaP/Pt resting potential at 0.25 V vs RHE, up from 0.88 V RHE for the bare GaP surface. This shows that the photoelectrochemical deposition of Pt shifts the Fermi level to more reducing potentials, likely due to partial reduction of the GaP surface. Under illumination, a photovoltage of 0.31 V is generated at 49 mW/cm^2, based on the variation of the OCP. This is a minor improvement compared to the bare GaP surface (0.22 V at 35 mW/cm^2). The Fermi level diagram in Fig. 3.3f describes the reducing power of the GaP/Pt photoelectrode at open circuit. Both Fermi levels change with increasing illumination intensity, but no Faraday reaction can occur, because $E_{F,f}$ never reaches the E^0 of the proton reduction potential. The photovoltage trend is similar to that of the bare GaP electrode, except that both $E_{F,n}$ and $E_{F,f}$ are more about 0.5 V more reducing. This is attributed to the possible reduction of the GaP surface during the cathodic photodeposition of the Pt cocatalyst, which populates some of the surface Ga(3+) states with electrons. Overall, the data shows that the addition of the Pt cocatalyst does not improve the open circuit photovoltage of the electrode. However, it does significantly increase the photocurrent at 0 V RHE (Fig. 3.3b), by speeding up electron transfer to the H^+/H_2 couple.

According to the literature, TiO_2, ZnS, and CdS buffer layers have the ability to passivate surface states resulting from corrosion states and dangling bonds.[29,32–34 41] For this study we chose CdS because of the favorable band alignment in Fig. 3.S7. The CdS layer was grown by chemical bath deposition from cadmium (II) acetate dihydrate and thiourea at basic pH. Based on Scanning

electron microscopy (SEM) and Energy dispersive X-ray (EDX) in Fig. 3.S8 and 3.S9, the CdS film is conformal and ~380 nm thick. PEC data for a GaP/CdS electrode in aqueous H_2SO_4 at pH 0.8 under N_2 flow is shown in Fig. 3.4b. The PEC scan reveals a greatly improved performance over the bare GaP electrode. The photocurrent is -1.6 mA/cm^2 at 0 V vs RHE, corresponding to an incident photon to current efficiency of 10.1 %. The photovoltage V_{Ph}(PEC) = 0.76 V (based on the 0.76 v RHE photocurrent onset potential) is improved over the previous 0.3 V value, and hydrogen is evolved visibly as gas bubbles at the working electrode. During 3 repeat scans, the bubbles cause the CdS layer to peel off the GaP wafer.

The n-CdS layer also increases the SPV (0.28 V at 3.03 eV) compared to bare p-GaP (Fig. 3.4c). While the effective band gap remains at 2.05 eV, the sub-band gap signal at 1.2-2.1 eV is increased by the CdS layer. Strong sub-band gap signals often indicate mid-band gap states exposed to strong electric fields.[42] On this basis, the 1.2-2.1 eV signal is assigned to states at the p-GaP/n-CdS interface (see Fig. 3.4a). The intensity dependent SPV in Fig. 3.4d reaches 0.68 V at 150 mW/cm^2, almost three times the previous value. Unlike bare p-GaP, p-GaP/n-CdS produces an SPV signal even under the smallest tested light intensity. Based on the photon flux at the lowest irradiance (4 mW/cm^2), the recombination rate is less than 8×10^{12} s-1 cm^{-2}. Also, a plot of the SPV signal versus the logarithmic light intensity is linear for the entire intensity range (Fig. 3.S3b), suggesting near ideal behavior of the photodiode. However, a very significant drift of the SPV baseline in Fig. 3.4d to more positive values suggests that electrons are trapped in the CdS surface or at states at the GaP/CdS interface.

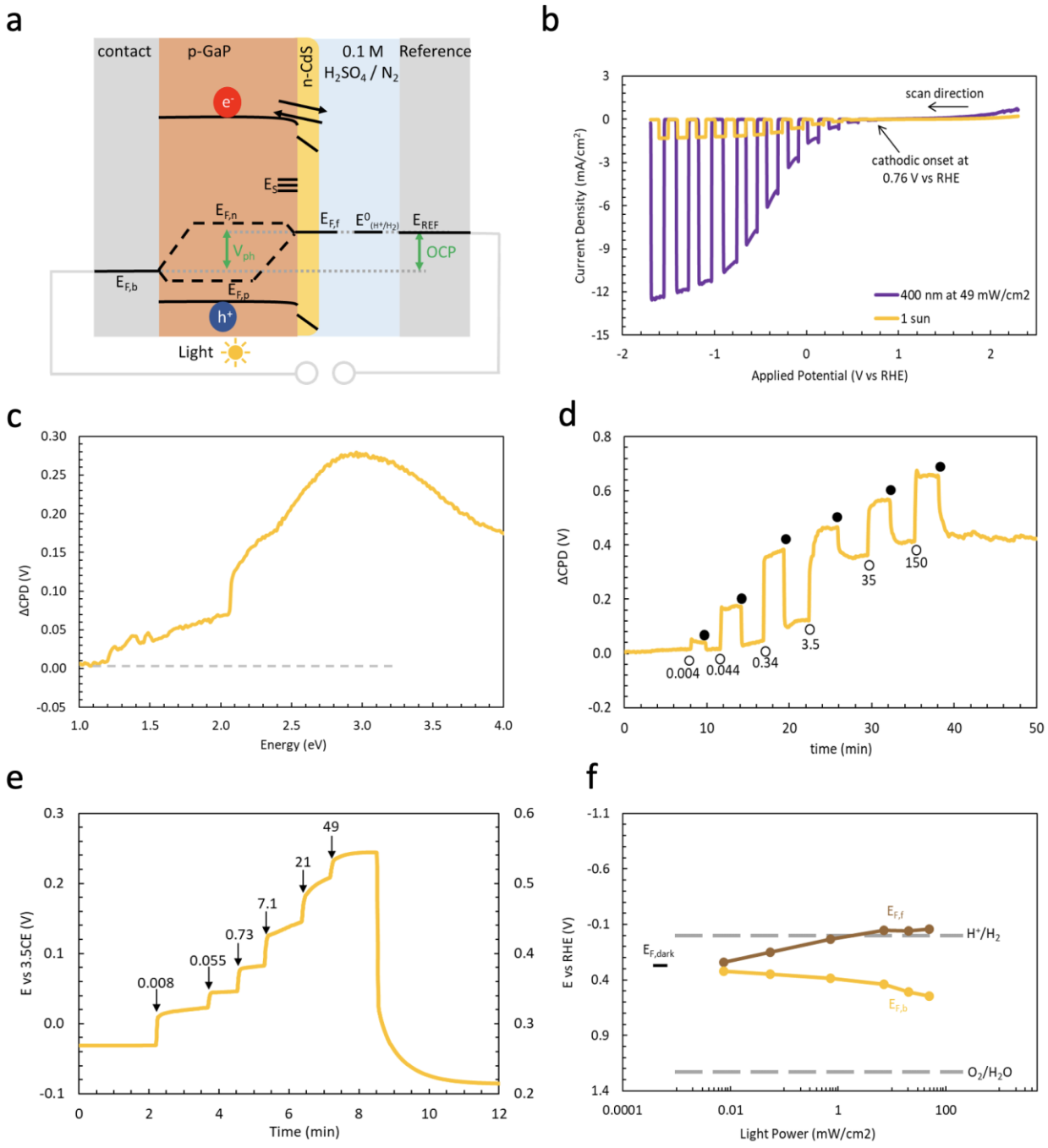

Figure 3.4: p-GaP/n-CdS in aqueous H_2SO_4 at pH 0.8 under N_2 flow. (a) Junction scheme under illumination. (b) Linear sweep voltammetry scans under chopped illumination from a 400 nm LED (49 mW/cm^2). (c) Surface photovoltage spectra under monochromatic Xe lamp illumination. (d) Intensity dependent surface photovoltage from a 405 nm LED displayed in mW/cm^2. (e) Intensity

dependent open circuit potential from a 400 nm LED displayed in mW/cm^2. (f) Fermi level diagrams constructed by using the OCP as the $E_{F,b}$ and the max ΔCPD as the difference between $E_{F,b}$ and $E_{F,f}$

According to OCP data in Fig. 3.4e, the $E_{F,b}$ of the GaP/CdS electrode is 0.27 V vs RHE in the dark, compared to 0.88 V vs RHE for the bare GaP. This proves that the n-CdS layer controls the Fermi level in the p-GaP electrode with its reducing workfunction and that a p-n-junction forms at the GaP/CdS interface. Based on the $E_{F,b}$ variation under illumination, the GaP/CdS electrode produces a photovoltage of V_{Ph}(OCP) 0.27 V at 49 mW/cm^2, slightly higher than what seen for the bare GaP wafer (0.23 V at 49 mW/cm^2). This agrees with the improved photovoltage seen in the SPV experiments. Please note also that V_{Ph}(OCP) values fall behind V_{Ph}(SPV) values over the entire illumination range (Fig. 3.4de). This discrepancy is due to the shortcomings of the OCP measurement, which probes the change in the back potential ($E_{F,b}$) while ignoring any drift of the front potential ($E_{F,f}$) to more reducing values. This is illustrated in the Fermi level plot in Fig. 3.4f. The diagram reveals considerable variation of *both* Fermi levels with light intensity. The drift in $E_{F,f}$ is attributed to electron trapping in the CdS layer, as mentioned above. Eventually, at 0.725 mW/cm^2, $E_{F,f}$ at the GaP/CdS front reaches the proton reduction potential, allowing the hydrogen evolution reaction (HER) without applied external bias. This agrees with the observation of gas evolution at the working electrode. As a result of the charge transfer equilibrium, $E_{F,f}$ becomes pinned at $E^o(H^+/H_2)$. Meanwhile, the hole fermi level moves to more oxidizing potentials, and higher photovoltage, as expected from the diode equation. Overall, these data demonstrate that removal of surface states from the bare GaP electrode and introduction of a p-n- junction at the GaP/CdS interface in Fig. 3.4a improve the solar energy conversion efficiency. However, the

photocurrent at 0 V RHE is lower for the GaP/CdS interface than for the GaP/Pt system, due to a large kinetic overpotential of CdS for proton reduction.[43]

To combine the benefits of the p-n-junction and the reduced proton reduction overpotential of Pt, a GaP/CdS/Pt device was constructed by sequential deposition of CdS and Pt nanoparticles. The photoelectrochemical properties of the p-GaP/n-CdS/Pt electrode are summarized in Fig. 3.5. Under 400 nm illumination (49 mW/cm^2) a photovoltage V_{ph}(PEC) of 0.59 V and a photocurrent of 9.8 mA/cm^2 at 0 V vs RHE resulting in an incident photon to current efficiency of 62 % (400 nm). As expected, these values are superior to the previous electrode configurations.

The SPV spectrum of the GaP/CdS/Pt device shows the photovoltage onset shifted to 2.51 eV compared to 2.06 eV for the bare GaP wafer. This is a result of shading by the Pt nanoparticle and CdS layers. Indeed, the optical absorption edge (Fig. 3.S3) of the GaP/CdS/Pt stack is found at 2.18 eV as a result of the parasitic absorption from the Pt nanoparticles. The maximum SPV is found at 0.43 V (250 mW/cm^2), much higher than seen for GaP/Pt, but slightly below the value observed for the GaP/CdS sample. The latter again is attributed to optical shading from Pt, which also explains why no SPV is generated at 0.008 mW/cm^2 405 nm LED illumination.

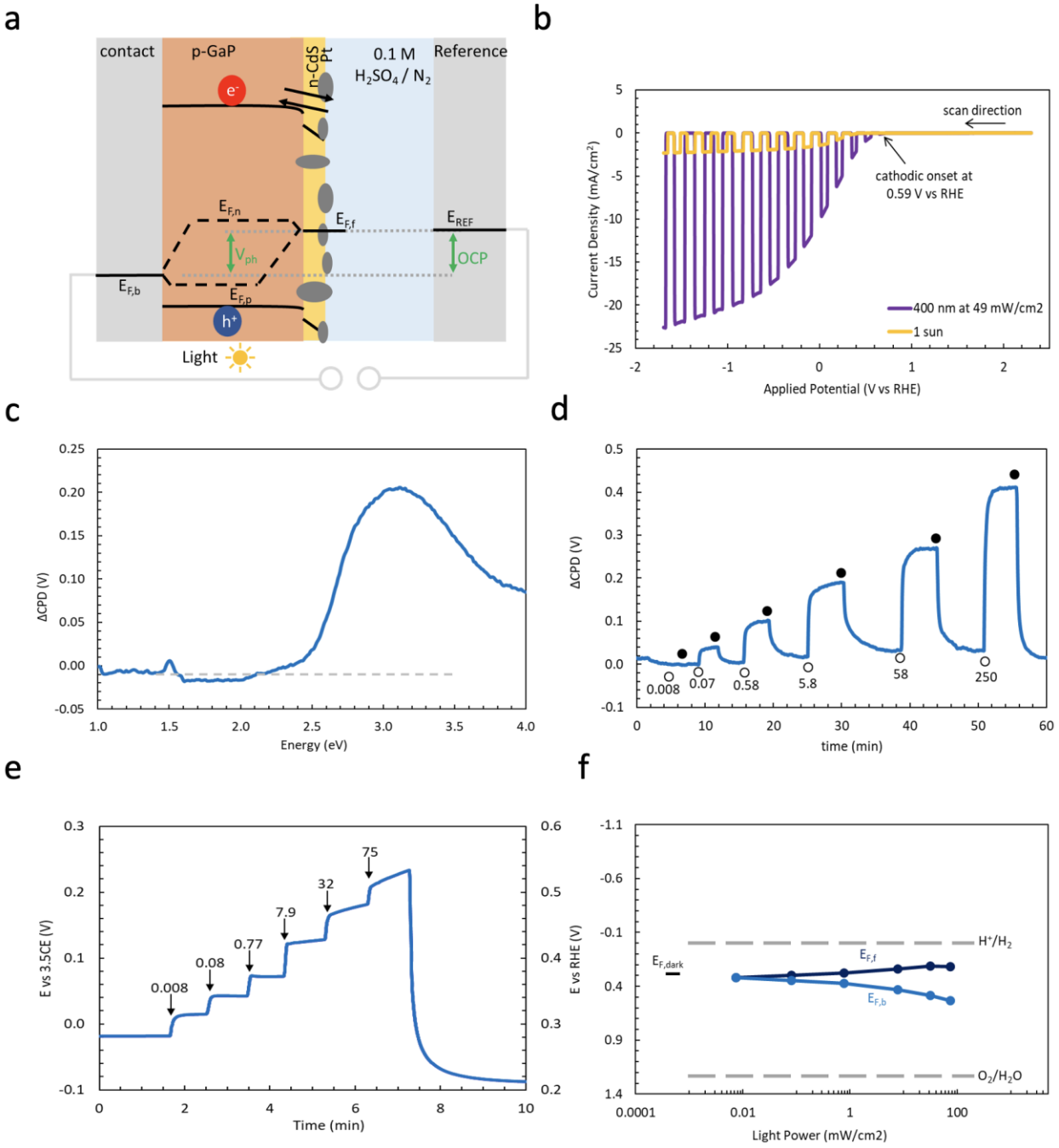

Figure 3.5: p-GaP/n-CdS/Pt in aqueous H_2SO_4 at pH 0.9 under N_2 flow. (a) Junction scheme under illumination. (b) Linear sweep voltammetry scans under chopped illumination. (c) Surface photovoltage spectra under monochromatic Xe lamp illumination. (d) Intensity dependent surface photovoltage from a 405 nm LED displayed in mW/cm^2. (e) Intensity dependent open

circuit potential from a 400 nm LED displayed in mW/cm^2. (f) Fermi level diagrams constructed by using the OCP as the $E_{F,b}$ and the max ΔCPD as the difference between $E_{F,b}$ and $E_{F,f}$. .

Based on the OCP measurements in Fig. 3.5e, the p-GaP/n-CdS/Pt electrode has a similar dark resting potential (0.28 V RHE) as the p-GaP/n-CdS electrode, i.e. the Fermi level is again controlled by the reducing CdS work function. The potential shifts to reducing values (0.21 V RHE) after completing an illumination cycle, which is attributed to electron trapping in CdS, as mentioned before. After combining the SPV and OCP data in the Fermi level diagram in Fig. 3.5f, it can be seen that photovoltage generation by the p-GaP/n-CdS/Pt electrode is only 67 % of that of the p-GaP/n-CdS version. Both Fermi levels drift under illumination, and even under the highest illumination intensity of 75 mW/cm^2 the minority carrier Fermi level $E_{F,f}$ does not quite reach the proton reduction potential. This means HER is not achieved with the unbiased p-GaP/n-CdS/Pt electrode in aqueous H_2SO_4 / N_2.

This surprising finding characterizes the p-GaP/n-CdS/Pt junction as an adaptive junction.[25, 26, 44] In adaptive junctions the semiconductor band bending (barrier height) and photovoltage are not fixed, as in a buried junction,[45-49] but change, depending on the charge transfer kinetics with the electrolyte and the redox potential of the electrocatalyst. Specifically, for the p-GaP/n-CdS/Pt electrode, the built-in potential of the junction is ill-defined because the N_2-purged H_2SO_4 solution lacks a fast redox couple.

Table 1: Summary of electrode properties from LSV, SPV, and OCP measurements for electrodes in 0.1 M H_2SO_4 under N_2 flow.

Sample	V_{Ph}(PEC) 1 sun (V vs RHE)	j_{ph} 400 nm 0 V vs RHE (mA/cm^2)	IPCE at 400 nm (%)	V_{Ph}(SPV) Under 405 nm Illumination (V)	R (s^{-1} cm^{-2})	V_{bi} From Dark OCP (V)	V_{Ph}(OCP) Under Max 400 nm Illumination (V)
Etched pGaP	0.30	-0.36	2.53	0.27	6.9×10^{14}	0.47	0.23
p-GaP/Pt	0.55	-3.78	24.0	0.38	9.0×10^{13}	1.09	0.31
p-GaP/n-CdS	0.76	-1.61	10.1	0.64	$< 8\times10^{12}$	1.09	0.27
p-GaP/n-CdS/Pt	0.59	-9.66	62.0	0.43	1.6×10^{13}	1.07	0.26
100 % N_2	0.56	-1.7	10.8	0.17	9.2×10^{12}	0.40	0.13
100 % O_2	0.62	-0.26	1.64	0.12	9.0×10^{13}	0.35	0.18
10 % H_2, 90 % N_2	0.31	-0.41	1.96	0.44	$< 1.0\times10^{13}$	1.04	0.30

To better understand the behavior of the p-GaP/n-CdS/Pt junction, and its response to the chemical composition of the electrolyte, measurements were repeated in a 0.1 M Na_2SO_4 (pH of 7) in the presence of N_2, H_2 or O_2. The results in N_2 atmosphere are shown in Fig. 3.6. In this

solvent the photovoltage and photocurrent of the electrode are degraded compared to 0.1 M H_2SO_4 (pH of 0.9).

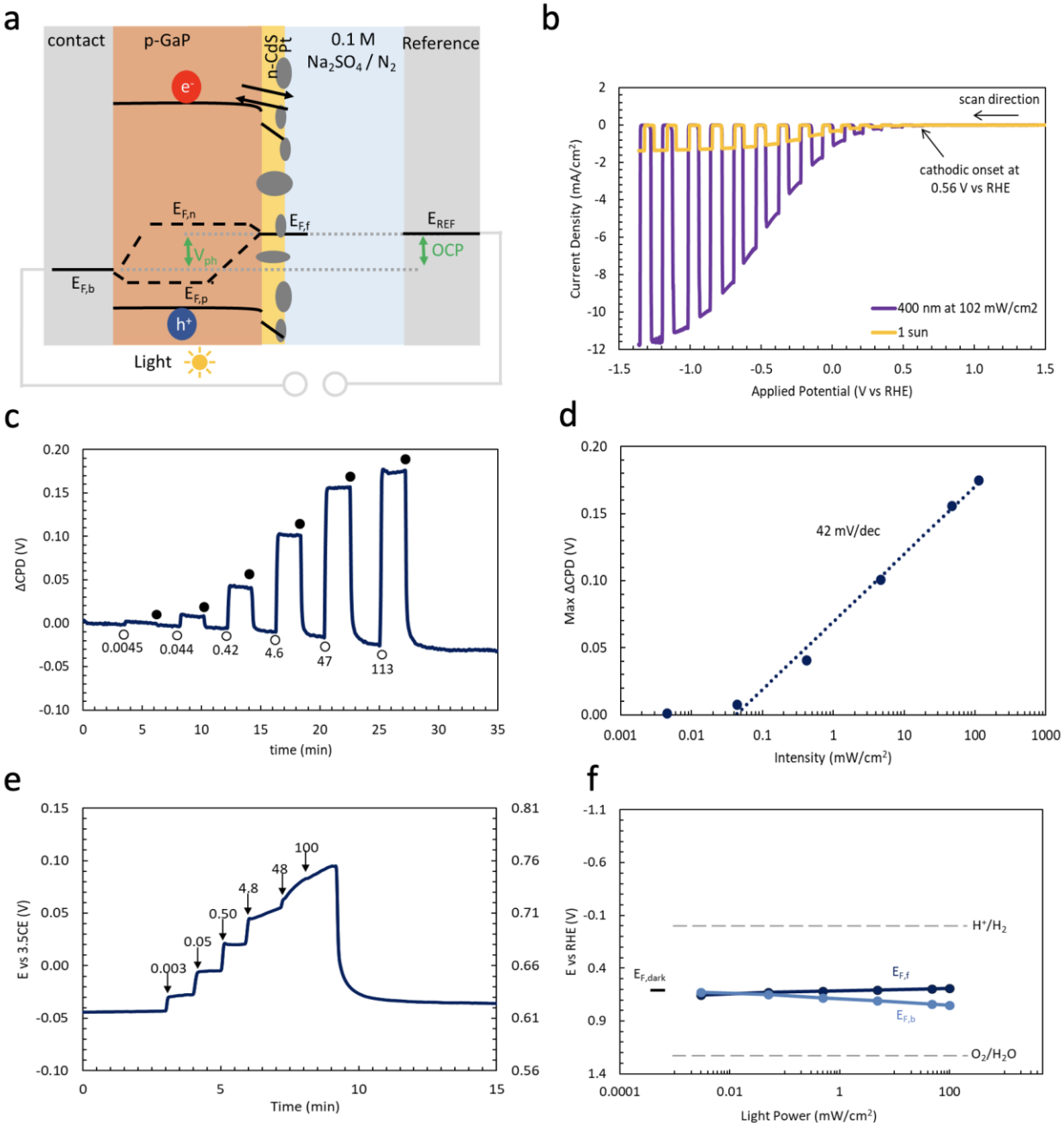

Figure 3.6: p-GaP/n-CdS/Pt in aqueous Na_2SO_4 at pH 6.6 under N_2 flow. (a) Junction scheme under illumination. (b) Linear sweep voltammetry scans under chopped illumination. (c) Intensity

dependent surface photovoltage from a 405 nm LED displayed in mW/cm^2 and (d) maximum ΔCPD versus logarithm of light intensity. (e) Intensity dependent OCP from a 400 nm LED displayed in mW/cm^2. (f) Fermi level diagrams constructed by using the OCP as the $E_{F,b}$ and the max ΔCPD as the difference between $E_{F,b}$ and $E_{F,f}$.

The photocurrent of 1.7 mA/cm^2 at 0 V vs RHE (IPCE of 10.8%) is only 17% of the value in 0.1 H_2SO_4. This is because the decrease in proton concentration slows down the HER kinetics. While V_{Ph}(PEC) = 0.56 V is similar to the electrode in acidic solution (0.59 V), the SPV signal is much smaller (0.18 V under 113 mW/cm^2 compared to 0.25 V under 75 mW/cm^2). Also, the SPV increases 42 mV per decadic increase in irradiance, while in acidic electrolyte the value is 71 mV dec^{-1}. The photovoltage from OCP (0.13 V at 100 mW/cm^2) is also much smaller than seen in 0.1 H_2SO_4 solution (N_2). These observations point towards a less effective solid-liquid junction in neutral Na_2SO_4 solution. This degraded junction is caused by a lower built-in potential, as seen from the more oxidizing E_F value in the dark (0.61 V RHE in neutral electrolyte, versus 0.22-0.28 V RHE in acidic solution). We hypothesize, this is a result of the slower charge transfer kinetics between the electrode and the electrolyte. Because no fast redox couples (H_2/H_2O, or O_2/H_2O) are present, the E_F value of the electrode is controlled by the combined work functions of Pt (5.64 eV, +1.20 V vs RHE for polycrystalline Pt)[50] and CdS (-0.1 V RHE).

To probe the effect of added O_2, measurements were repeated in 0.1 M Na_2SO_4 saturated with O_2 at 1.0 atm. This time (Fig. 3.7), the cathodic photocurrent reaches only 0.26 mA cm^{-2} at 0 V vs RHE, which is 15 % of the photocurrent in 0.1 M Na_2SO_4 (N_2). The photocurrent onset is at 0.62 V vs RHE, but the photovoltage cannot be extracted from this because it is not clear if protons or oxygen are being reduced. Lastly, saw-toothed shaped photocurrent transients appear, that

are a sign of trapping and de-trapping of electrons at the photoelectrode surface.[35] This may involve the chemisorbed O_2/O_2^-(superoxide) redox couple.

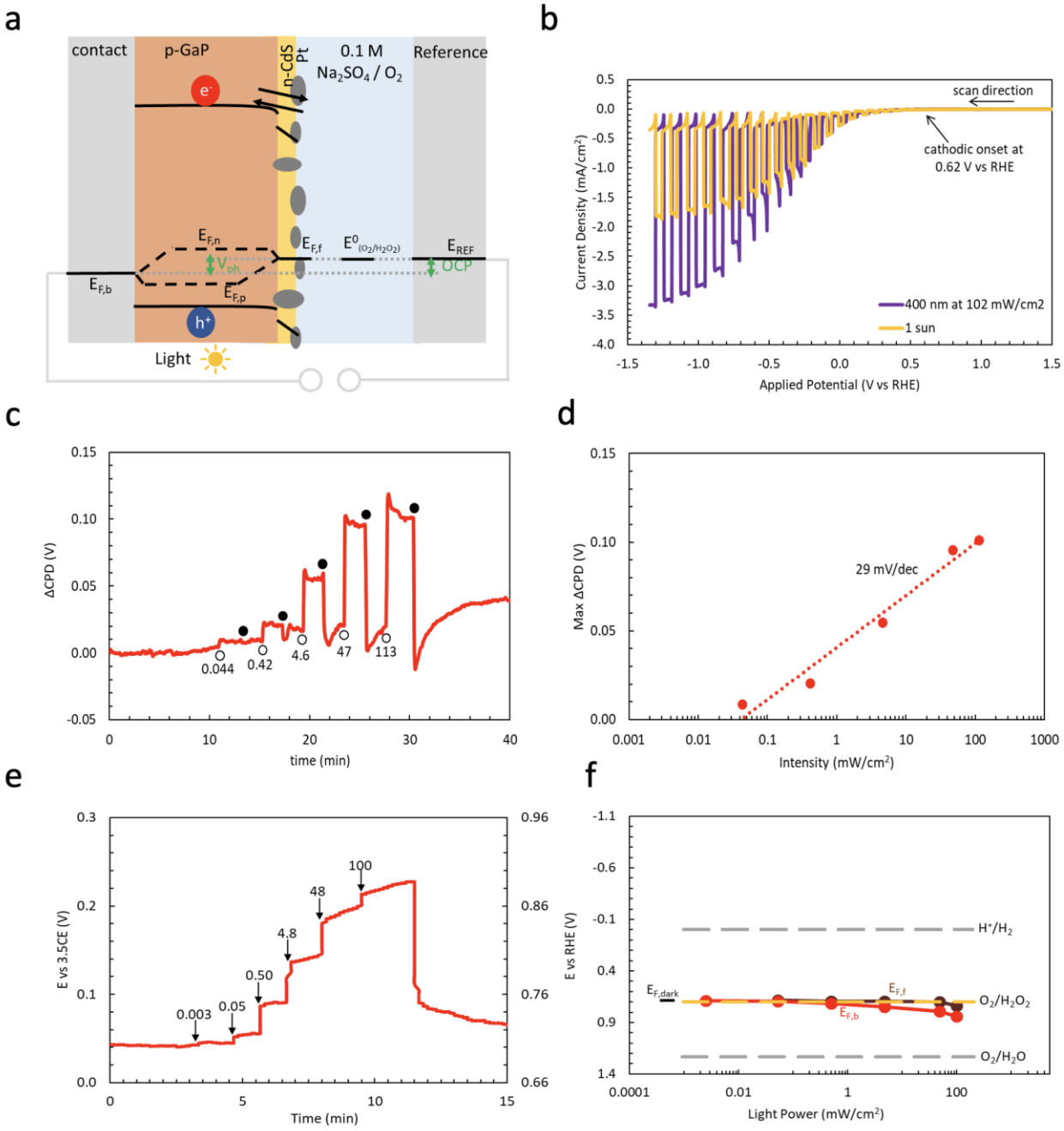

Figure 3.7: p-GaP/n-CdS/Pt in aqueous Na_2SO_4 at pH 6.8 under O_2 flow. (a) Junction scheme under illumination. (b) Linear sweep voltammetry scans under chopped illumination. (c) Intensity

dependent surface photovoltage from a 405 nm LED displayed in mW/cm^2 and (d) maximum ΔCPD versus logarithm of light intensity. (e) Intensity dependent OCP from a 400 nm LED displayed in mW/cm^2. (f) Fermi level diagrams constructed by using the OCP as the $E_{F,b}$ and the max ΔCPD as the difference between $E_{F,b}$ and $E_{F,f}$.

Transient LED illumination (Fig. 3.7c) produces positive SPV signals, but the values are small (0.12 V) and near zero under the weakest illumination (0.003 mW/cm^2). Based on the change of the E_F under 100 mW/cm^2 illumination, a V_{Ph}(OCP) of up to 0.18 V develops, as shown in Fig. 3.7e. This is much smaller than seen in 0.1 M H_2SO_4 (N_2) solution (0.26 at 75 mW/cm^2). In the dark, a Fermi level of 0.70 V vs RHE was recorded, which increases to 0.72 V after the illumination cycle is finished. These positive values are due to adsorbed O_2 and the associated O_2/H_2O_2 reduction potential of 0.70 V RHE.[51]

Looking at the Fermi energy diagram in Fig. 3.7f, it can be seen that the minority carrier potential at the front of the electrode $E_{F,f}$ is pinned to the O_2/H_2O_2 reduction potential (0.70 V RHE throughout the experiment. This occurs because in the presence of 1.0 atm O_2 and 10^{-7} M H_3O^+, O_2 reduction is approximately 10^7 times much faster than proton reduction. This reduces the built-in potential of the junction and its photovoltage output. Based on the 0.62 V vs RHE photocurrent onset in Fig. 3.7b the energy conversion efficiency of this O_2 reduction photocathode is zero.

Lastly, PEC data for the p-GaP/n-CdS/Pt electrode in 0.1 M Na_2SO_4 saturated with forming gas (10% H_2 and 90% N_2) are shown in Fig. 3.8. The cathodic photocurrent is found to be 1.7 mAcm^{-2} at 0 V vs RHE (IPCE = 1.96 %) and the photovoltage, V_{ph}(PEC) is 0.31 V. The SPV reaches 0.44 V (Fig. 3.8c), which is 2.5 and 4 times the value in N_2 or O_2 atmosphere, respectively.

Illumination is accompanied by the formation of small gas bubbles on the surface of the electrode (Fig. 3.S10), indicating successful proton reduction to H_2, without any applied bias. Based on the positive CPD base line drift in Fig. 3.8c this charge transfer is irreversible. It is caused by the quasi-irreversible charge transfer resulting from the diffusion of hydrogen gas away from the electrode.

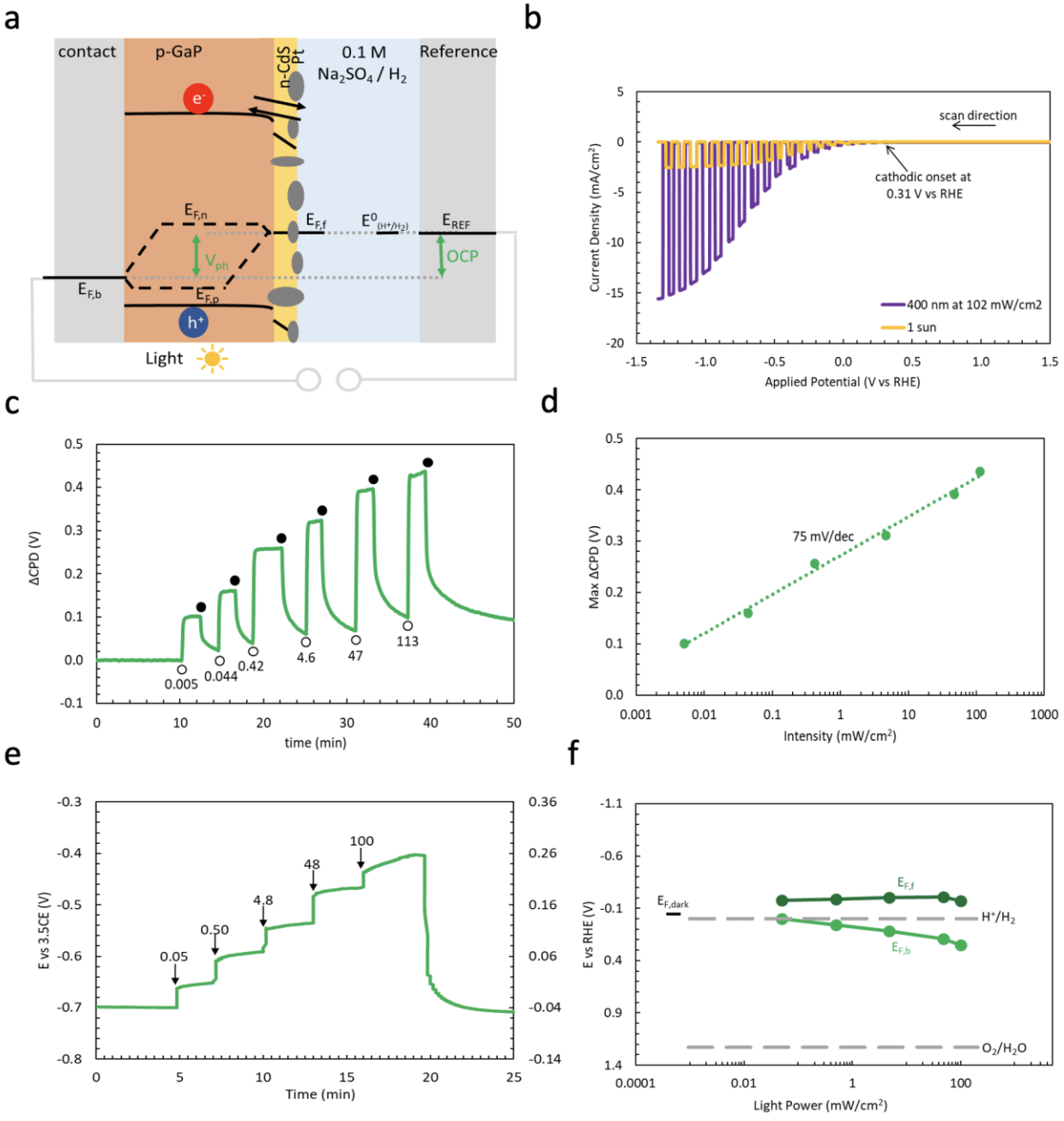

Figure 3.8: p-GaP/n-CdS/Pt in aqueous Na_2SO_4 at pH 6.9 under 10% H_2 in N_2 flow. (a) Junction scheme under illumination. (b) Linear sweep voltammetry scans under chopped illumination. (c) Intensity dependent surface photovoltage from a 405 nm LED displayed in mW/cm^2 and (d) maximum ΔCPD versus logarithm of light intensity. (e) Intensity dependent OCP from a 400 nm LED displayed in mW/cm^2. (f) Fermi level diagrams constructed by using the OCP as the $E_{F,b}$ and the max ΔCPD as the difference between $E_{F,b}$ and $E_{F,f}$.

Based on the SPV vs Log I data in Fig. 3.8d (slope 75 mV dec^{-1}), the junction is near ideal and generates photovoltage even at the lowest light intensity (0.05 mW/cm^2). The ability of the p-GaP/n-CdS/Pt electrode to generate H_2 without applied bias is reflected in the Fermi level diagram in Fig. 3.8f. It shows an $E_{F,f}$ at -0.2 V vs RHE at all light intensities, sufficient for proton reduction. In the dark, the E_F of -0.04 V RHE is also controlled by the electrochemical potential (0.0 V RHE) of the H^+/H_2 couple. This shows how fast charge transfer with the H^+/H_2 couple provides generates a strong built-in potential for good charge separation.

The above results illustrate how the photovoltage and photocurrent of the GaP photocathode vary with the addition of Pt electrocatalysts and the CdS layer and depend also on the charge transfer kinetics of the redox couples in the electrolyte and their redox potentials. To better depict the influence of these parameters, a plot of the photovoltage versus the built-in potentials V_{Bi} is shown in Fig. 3.9a. It can be seen that the photovoltage (the maximum free energy output of the electrode per electron) increases with the built-in voltage of the electrode-liquid contact. A nearly linear relationship between V_{Ph} and V_{Bi} is seen for all GaP/CdS/Pt electrodes in Na_2SO_4 electrolyte. This is because the GaP/CdS/Pt liquid junctions are chemically identical and

only differ in the redox properties of the gases, N_2, H_2/N_2(1:9), O_2, present during the measurements. The linear correlation between V_{Bi} and V_{Ph} shows that the barrier height of the junction controls charge separation under illumination. However, photovoltages are only ~ 33% of the built-in potentials, which suggest that significant electron hole recombination is dominant in these systems. Photovoltage losses are particularly significant for Pt containing electrodes. This suggests that Pt causes electron-hole recombination loss in these electrodes. Other studies have confirmed recombination at semiconductor-Pt contacts for n-$GaInP_2$/Pt photoelectrodes[52] and in CdS/Pt photocatalysts for hydrogen evolution.[53] Because the p-GaP/Pt contact is nearly ohmic (due to the similarity of work functions), charge transfer from GaP is expected to be non-selective, allowing electrons to recombine with holes at the GaP/Pt interface.[54] The addition of the CdS passivation layer minimizes contact between GaP and Pt particles and improves the photovoltage. This allows the higher photovoltages for the p-GaP/CdS/Pt – H_2SO_4 – N_2 and H_2 systems.

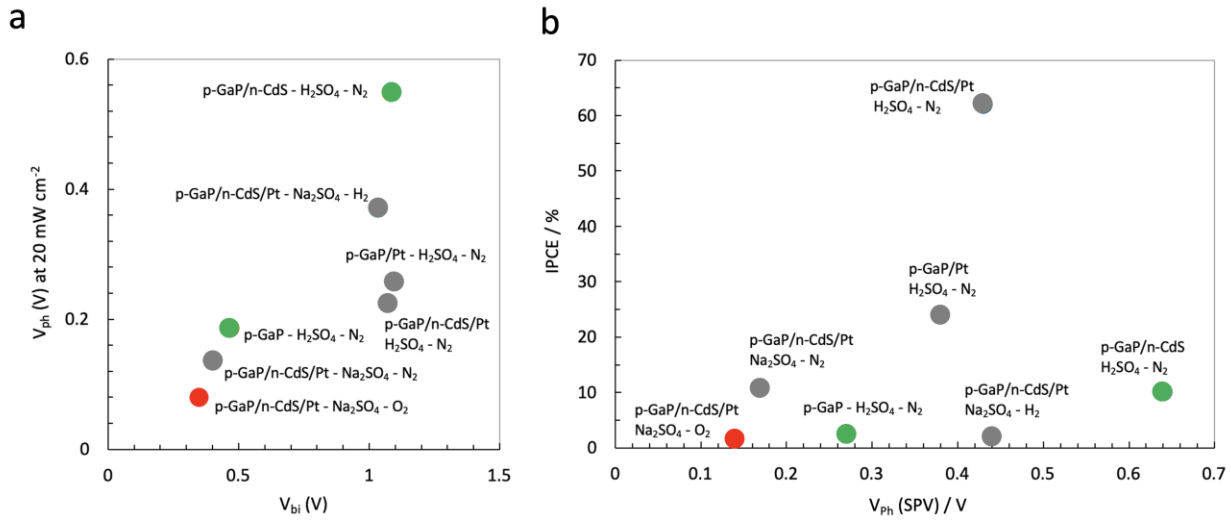

Figure 3.9: Plot of the a) open circuit photovoltage V_{Ph}(SPV) at 405 nm (20 mW/cm^2) versus the built-in potential $V_{Bi} = E_{FB}$-E_F(dark). Values from Table 1. b) IPCE versus V_{Ph}(SPV).

Energy conversion with the p-GaP/CdS/Pt – H_2SO_4 – O_2 system is diminished because the oxidizing O_2/H_2O_2 redox couple reduces the electron transfer barrier V_{Bi}. Energy conversion is enhanced with added H_2 due to an increased barrier V_{Bi}. The effects of O_2 and H_2 on the charge separation efficiency of the junction are noteworthy in the context of water splitting photocatalysts. They predict improved photocatalytic activity in the presence of hydrogen (improves the semiconductor-liquid junction) and diminished activity in the presence of oxygen. The fact that O_2 promotes the back reaction (O_2 reduction) by accepting electrons from the proton reduction site is already well known. This reaction needs to be suppressed with selective electrocatalysts, such as Rh/Cr_2O_3 or $Rh_{2-y}Cr_yO_3$ to achieve water splitting.[55, 56] The new results here show that O_2 is not just a competitive electron acceptor, but it is also degrading the p-type semiconductor-liquid junction, causing electron hole recombination. Therefore, improved water splitting photocatalysts might be possible by preventing *electric* contact between O_2 and the proton reduction site.

To better understand the variables affecting the photocurrent of the various devices, IPCE values are plotted in Fig. 3.9b versus the measured photovoltage. As expected, there is a correlation between the open circuit photovoltage and the photocurrent, but the correlation is weak and there are many exceptions. The highest IPCE values occur for electrodes containing a Pt cocatalyst, illustrating the importance of fast charge transfer kinetics (and a low overpotential) on electrode performance. For GaP/CdS device the photocurrent is low because cadmium chalcogenides have significant proton reduction overpotentials, [43] even though this configuration has a very large photovoltage due to its p-/n-junction. Similarly, the low IPCE of the GaP-H_2SO_4 electrode is due to the absence of the Pt cocatalyst, and the presence of surface states which

cause a low built-in voltage. Fig. 3.9b also shows that depressed IPCE values result from the exchange of the H_2SO_4 electrolyte for Na_2SO_4. The proton concentration in the latter is 10^7 lower, and the proton reduction kinetics are slower,[57] which limits the photocurrents in Na_2SO_4. Interestingly, the presence of H_2 in the GaP/CdS/Pt -H_2SO_4 – H_2 system also slows down proton reduction. The observed lower IPCE values are attributed to the H_2 induced Nernstian shift of the proton reduction potential to more negative values, and to an increased H_2 diffusion overpotential.[57] Overall, Fig. 3.9 shows that the charge separating ability (photovoltage) of GaP solar fuel electrodes is mainly controlled by the thermodynamics at the semiconductor interface (the built-in potential). The photocurrent on the other hand is mainly controlled by the charge transfer kinetics, as controlled by the concentrations and reduction potentials of the electron acceptors and by the electrocatalytic properties of the interface. Superior energy conversion performance, as in the p-GaP/CdS/Pt/H_2SO_4 - N_2 device, is only possible in the absence of both slow charge transfer kinetics and a low built-in potential of the junction.

3.4 Conclusion

In summary, we provide a comprehensive evaluation of the factors that control the photocurrent and open circuit photovoltage of p-GaP photoelectrodes for hydrogen evolution from water. The open circuit photovoltage of the bare GaP-liquid junction is limited by Fermi level pinning from surface states, which reduces the band bending of the junction and its ability to separate charge. An CdS overlayer increases the GaP photovoltage and photocurrent due to formation of a n-p- buried junction and due to passivation of GaP surface defects. An electrodeposited Pt cocatalyst increases the photocurrent due to improved HER kinetics, but

reduces the photovoltage by promoting charge recombination at the GaP/Pt interface. Added O_2 reduces the photovoltage by diminishing the electrostatic barrier (band bending) in the junction, and added H_2 increases it. This characterizes the the p-GaP/n-CdS/Pt electrode as an 'adaptive' and not a 'buried' junction. This can be attributed to direct contact between Pt and the GaP. Conversely, added H_2 or increasing pH of the electrolyte reduces the photocurrent. This is due to the effect of the charge transfer kinetics. The higher performance (IPCE of 62% and photovoltage of 0.43 V at 250 mW/cm^2 and 400 nm) of the p-GaP/n-CdS/Pt/H_2/H_2O champion device results from a balance between charge separation and good kinetics. The other electrodes are limited by either poor kinetics or bad charge separation. Both processes need to be optimized for superior energy conversion with photoelectrodes and photocatalysts under low or zero applied bias. Separately the work compares different methods to measure the open circuit photovoltage of solar fuel photoelectrodes. Photovoltage values from vibrating Kelvin probe VKP-SPV appear more reliable than photovoltage values from photoelectrochemical (PEC) or open circuit potential (OCP) measurements because no assumptions are needed regarding the nature of the Faraday reaction at the electrode or the electrochemical potential at the electrode front.

3.5 Experimental

Chemicals: Concentrated sulfuric acid (Sigma-Aldrich) , hydrogen peroxide (30%, Fisher), thiourea (99%, Alfa Aesar), cadmium acetate dihydrate (analytical reagent, Mallinckrodt), ammonium hydroxide (29.7%, certified ACS plus, Fisher), hexachloroplatinic acid (99.9%, Alfa Aesar), and sodium sulfate (>99.0%, Sigma-Aldrich) were used as received. Water was purified using a Nano-pure system to >16 MΩcm resistivity. The p-type gallium phosphide wafer doped with zinc (polished/unpolished, carrier density of 6.8×10^{17} cm^{-3}) was obtained from El-Cat and

manufactured by the Institute of Electronic Materials Technology. It was etched in a small beaker containing 3 mL sulfuric acid, 1 mL hydrogen peroxide, and 1 mL nanopure water (piranha acid) at 50 °C for 10 min. The wafer was washed 5 times with nanopure water to remove excess etchant and dried in the dark under a N_2 flow. All measurements were conducted on the non-polished side of the wafer.

CdS deposition: Thin n-CdS layers were fabricated using a modified procedure by Zhang and co-workers.[34] A freshly etched piece of p-GaP wafer was pre-soaked in 20 mL of an aqueous solution containing 7.5 mM cadmium acetate dihydrate and 2.5 M ammonium hydroxide at 80 °C for 10 minutes. Then the wafer was moved to a solution of 7.5 mM cadmium acetate dihydrate, 0.375 M thiourea, and 2.5 M ammonium hydroxide at 70 °C for an additional 10 minutes. The wafer was rinsed with water to remove excess reagents and allowed to dry for 15 minutes in air. Finally, the wafer was annealed in air at 300^0C for one hour.

Pt photodeposition: Following the procedure by Mali and co-workers,[36] a 50 mL solution of 0.1 M sodium sulfate and 10 μM hexachloroplatinic acid was prepared and placed into a 3-electrode electrochemical cell, using a Pt counter electrode and a 3.5 M SCE reference electrode. The p-GaP/n-CdS wafer was masked with polyethylene tape on the back side and lowered into the solution. The solution was then degassed with N_2 for 20 minutes before simulated 1 sun illumination and an applied bias of -0.75 V vs 3.5CE was applied for one hour. The wafer was removed from the solution and rinsed with water and stored in the dark in air.

Surface photovoltage (SPV): measurements were conducted using a circular (2.5 mm diameter), semitransparent vibrating gold mesh disk (Kelvin Probe S, Besocke Delta Phi) that was mounted inside of a home-built vacuum chamber and controlled by a Kelvin Control 7

Oscillator/amplifier (*Besocke Delta Phi*). Samples were grounded electrically via an allegator clip and 10 µL of electrolyte was pipetted onto the electrode and a microscopy cover glass (*Fisher Scientific*, 0.17 to 0.25 mm thickness) was placed over the liquid. The Kelvin probe was lowered until 1-2 mm above the sample. The spectrum was measured with light from a 300 W xenon lamp filtered through an Oriel Cornerstone 130 monochromator in the 0.4 – 5.0 eV interval. During the measurements, the chamber was purged continuously (1 L/min) with N_2 or O_2 or H_2/N_2 gas saturated with water to prevent drying of electrolyte. Intensity dependent SPV measurements were conducted with an air-cooled 405 nm LED in the 0.004 mW/cm^2 and 250 mW/cm^2 intensity range. The baseline was corrected by subtracting a fit of a dark scan.

Photoelectrochemical (PEC): measurements were conducted in a three-electrode set up with a Pt counter electrode and a 3.5 M calomel reference electrode (3.5CE). The p-GaP working electrode had the back side covered with polyethylene tape and was connected using a toothless copper clip. The exposed area was measured graphically (imageJ) to calculate current density. The solution and enclosed head space was purged with N_2 gas to remove oxygen for >15 min or until the measured OCP had no more drift. The working electrode was calibrated using the potential (E^0=+0.358 V vs. NHE) of the $K_{4/3}[Fe(CN)_6]/Fe(CN)_6^{4-}$ redox couple. A 300 W Xe lamp was used as the light source and the distance was adjusted to have an intensity of 100 mW/cm^2 (1 sun) at the working electrode using a photometer equipped with a GaAsP light detector (International Light Technologies, Inc.).

Open circuit potential (OCP): measurements were performed using light from an air cooled 400 nm LED between 0.003 mW/cm^2 and 100 mW/cm^2. The voltage was regulated with a DC power supply and its intensity measured by a photometer equipped with a GaAsP UV-Vis

detector (International Light Technologies, Inc.). Several light on/off cycles were used to determine the electrode potential in the dark once it stabilized. UV-vis diffuse reflectance spectra were recorded on the wafer using a Thermo Scientific Evolution 220 spectrometer after calibration with a $BaSO_4$ disc as a reference. Scanning electron microscopy (SEM) and energy dispersive X-ray spectroscopy (EDX) were taken on a Scios DualBeam SEM/FIB instrument with an accelerating voltage of 10-20 kV.

3.6 Supplemental Information

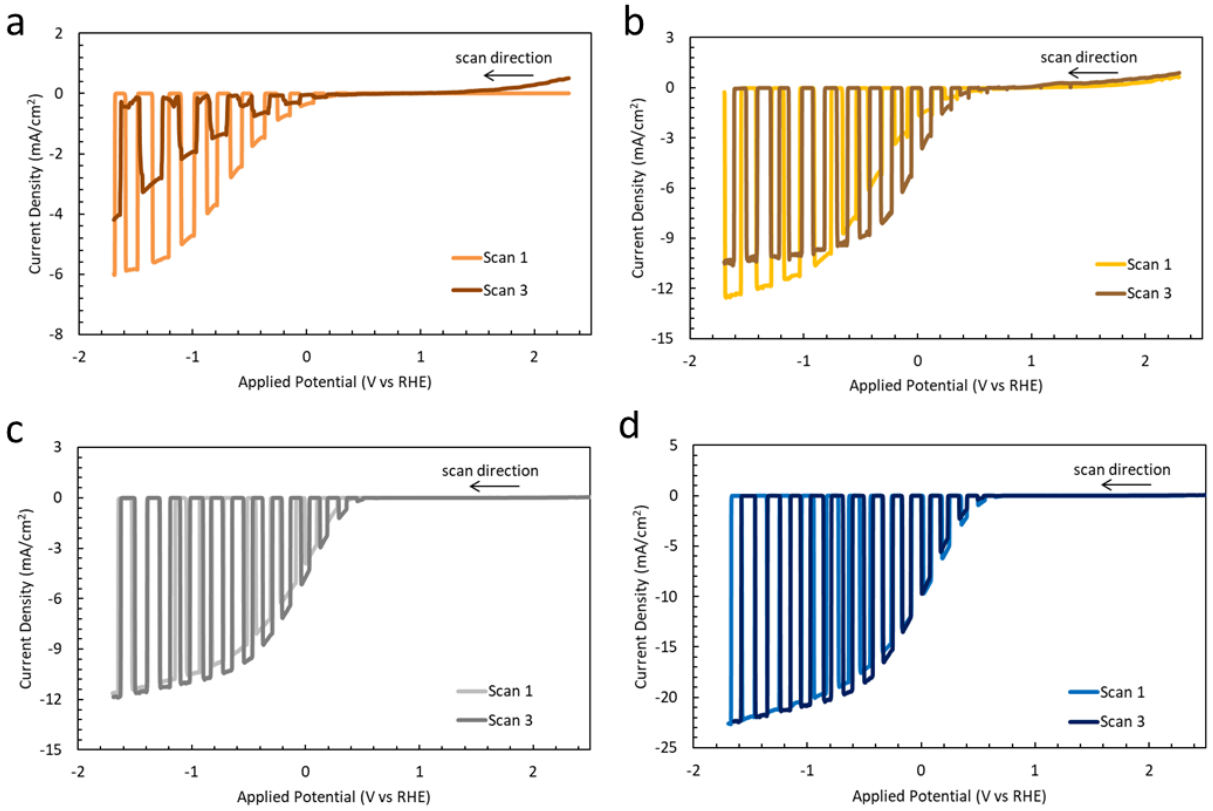

Figure 3.S1: Repeated linear sweep voltammetry scans under chopped illumination in aqueous H_2SO_4 at pH 0.8 to 1.0 under N_2 flow for (a) p-GaP, (b) p-GaP/n-CdS, (c) p-Gap/Pt, and (d) p-GaP/n-CdS/Pt electrodes.

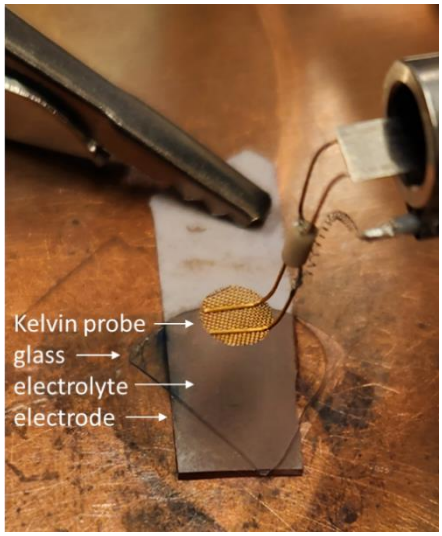

Figure 3.S2: Photo of GaP electrode in configuration for SPV measurements.

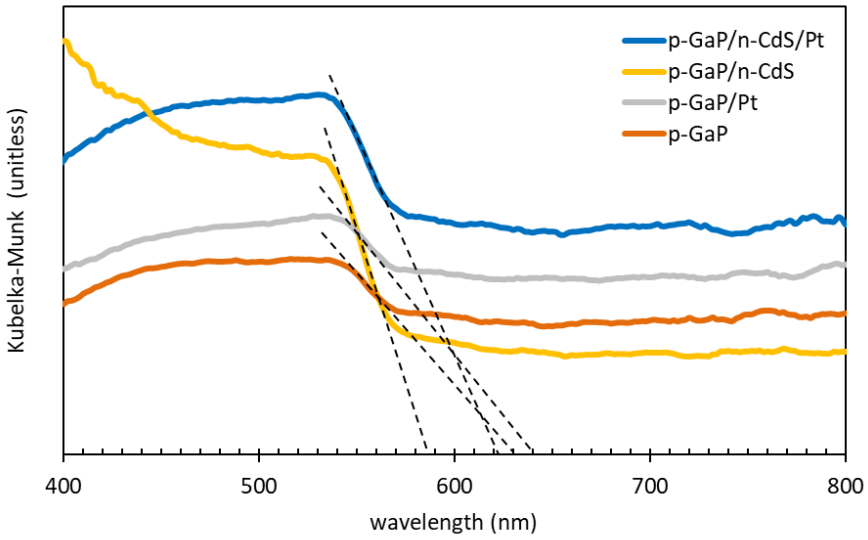

Figure 3.S3: Diffuse reflectance spectroscopy of electrodes.

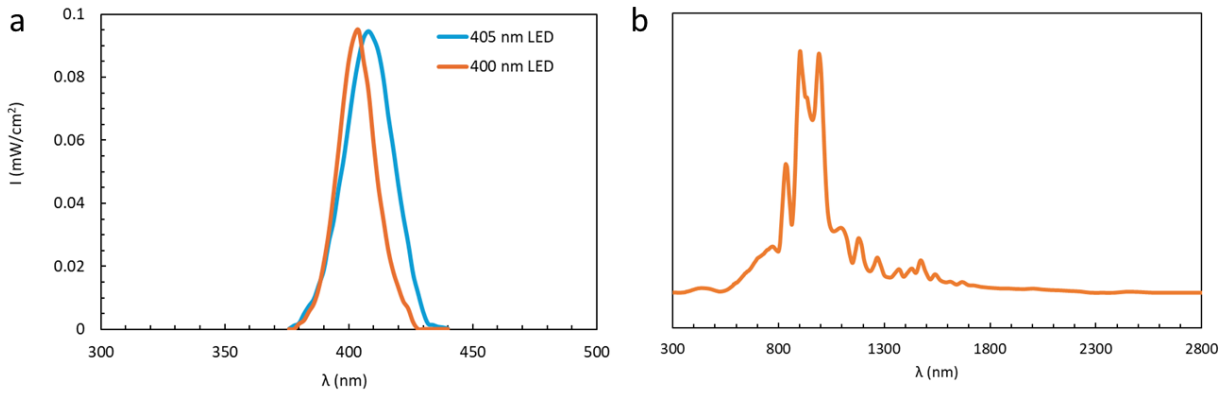

Figure 3.S4: Light source power spectra for (a) 400 and 405 nm LEDs and (b) 300 W Xe lamp.

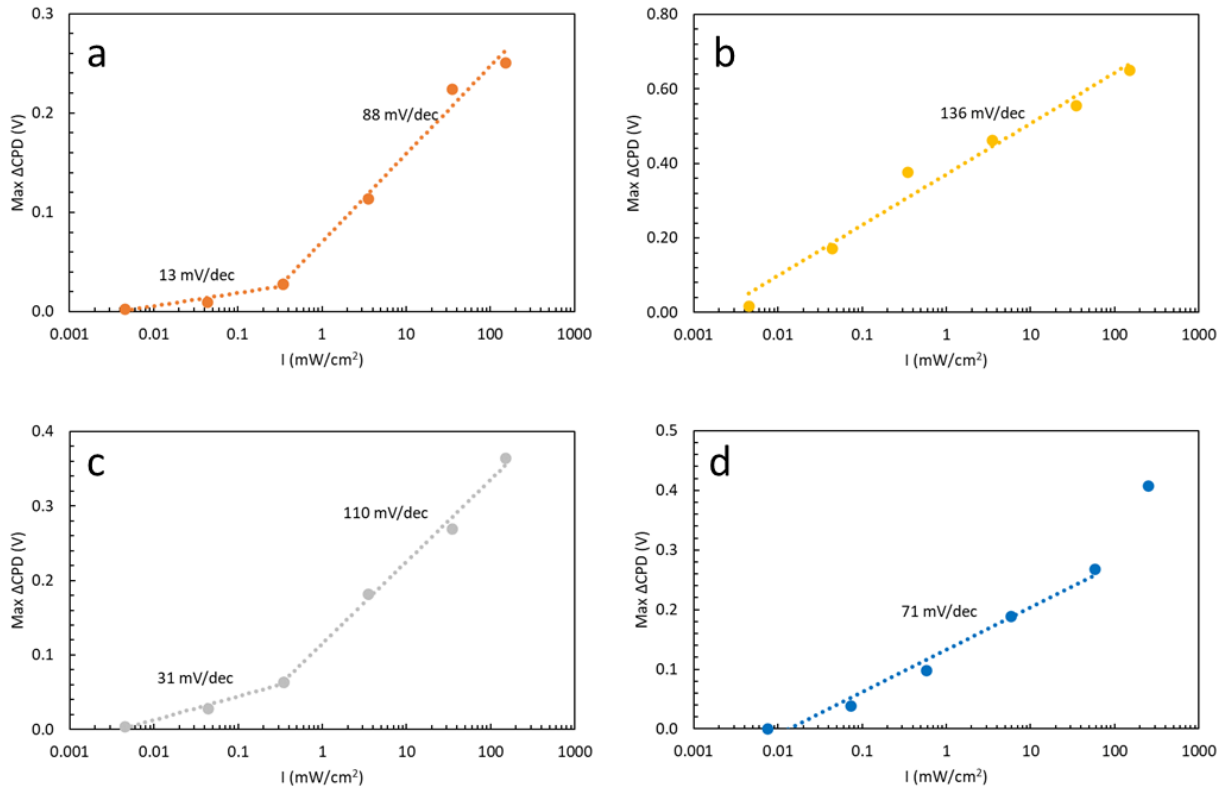

Figure 3.S5: Surface Photovoltage (ΔCPD) versus logarithm of light intensity for (a) p-GaP, (b) p-GaP/n-CdS, (c) p-GaP/Pt, and (d) p-GaP/n-CdS/Pt. Chamber was purged with continuous N_2 flow. All solutions 0.1 M H_2SO_4 with a pH between 0.8 and 1.0. a) continue tangent to include point at

0. The ideality factor for the p-GaP/n-CdS junction in b) is 2.3. Deviation from the ideal value of 1 are attributed to recombination in the depletion layer.

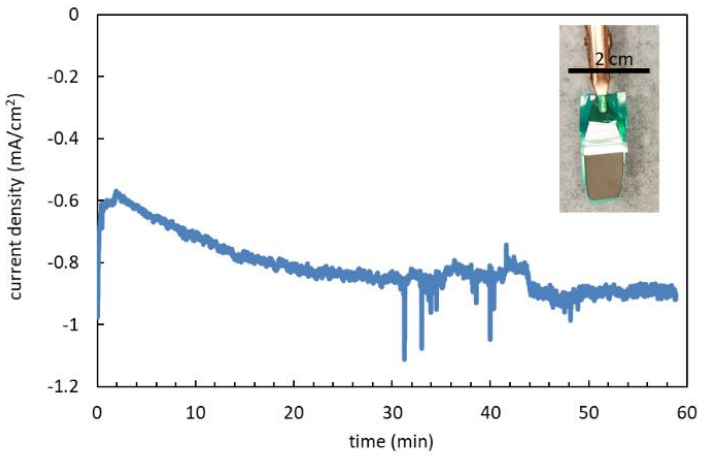

Figure 3.S6: Current density versus time for photodeposition of Pt onto p-GaP/n-CdS at an applied bias of -0.75 V vs 3.5 CE. (Insert)photo of resulting p-GaP/nCdS/Pt electrode photo.

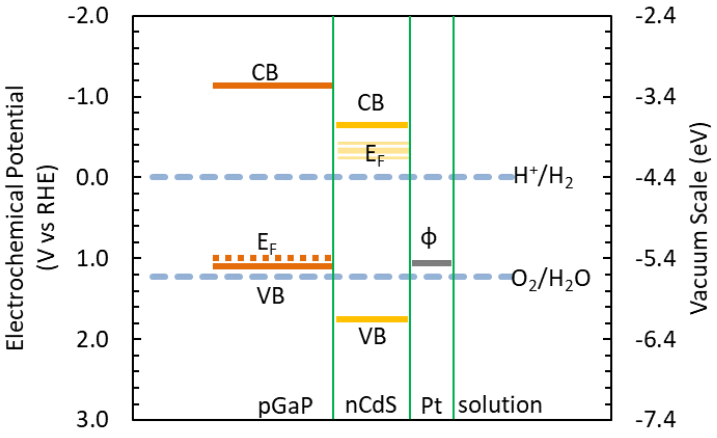

Figure 3.S7: flat band energy diagram for pGaP/CdS/Pt/H_2O. Where the conduction and valence band potentials are from Chen and Wang.[1] The native Fermi level for the pGaP wafer was

calculated from the carrier density and valence band position. Meanwhile the exact position of the Fermi level for n-CdS is unknown. Pt work function [1]

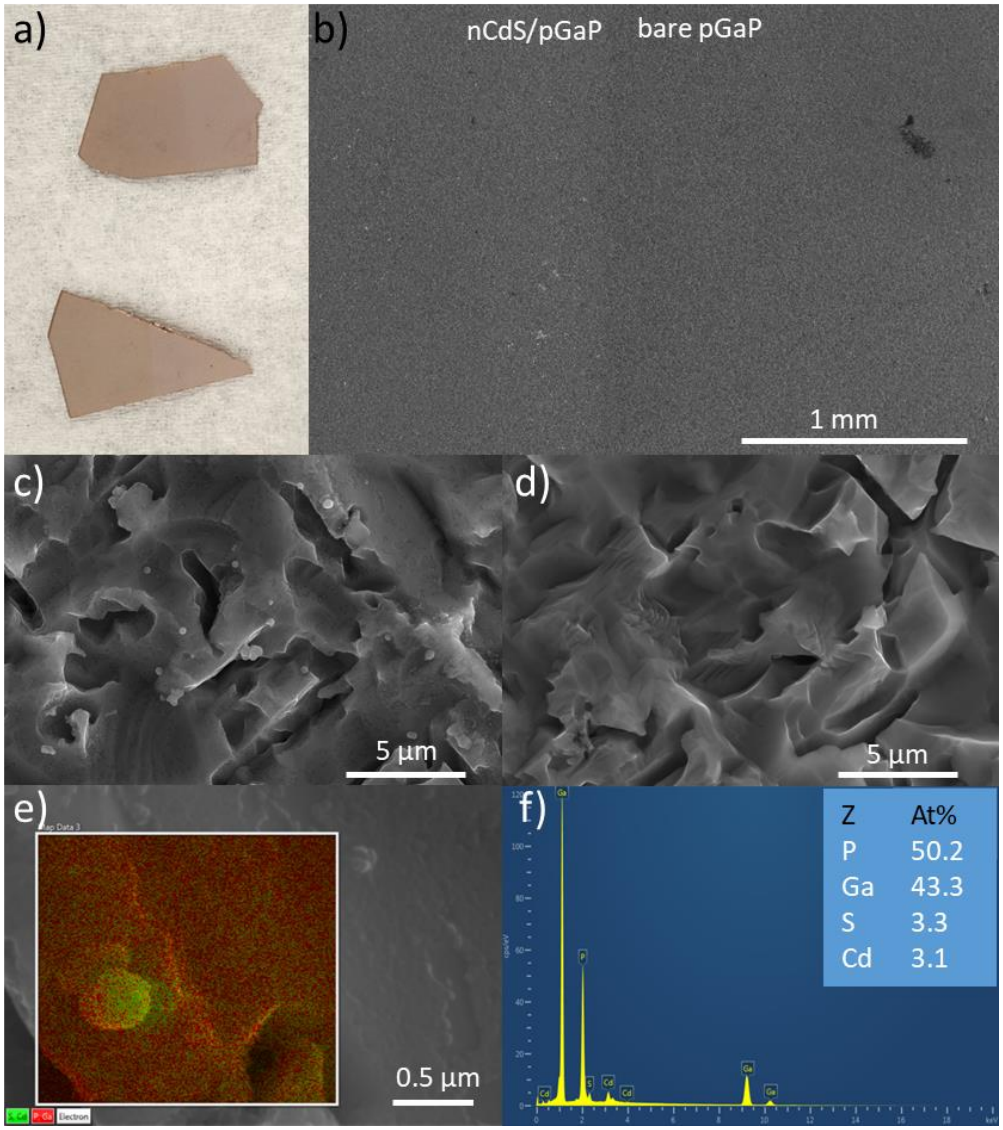

Figure 3.S8: (a) Photo of two p-GaP/n-CdS electrodes. The lefthand side of each electrode, more yellow/brown side contains the n-CdS layer and the right, more orange/grey side is bare p-GaP. (b-d) SEM images of p-GaP/n-CdS and bare p-GaP regions. (e-f) energy dispersive X-ray (EDX) of p-GaP/n-CdS region.

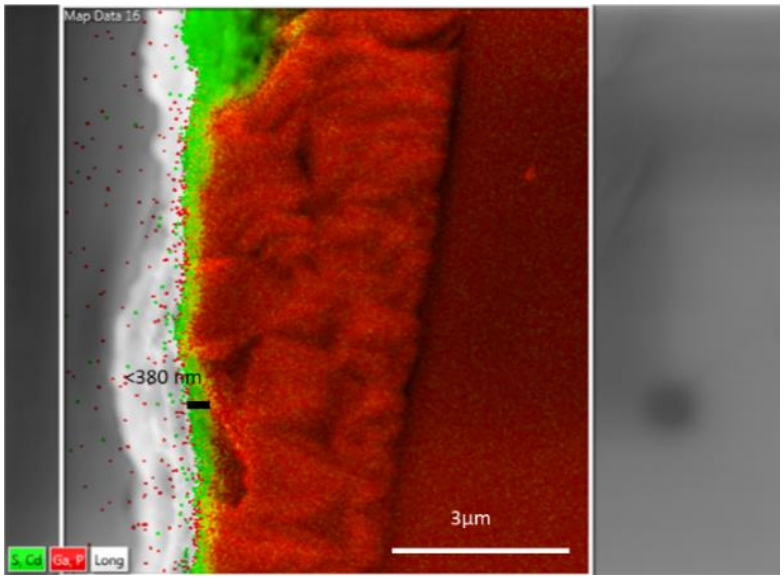

Figure 3.S9: Cross-sectional SEM of p-GaP/n-CdS electrode. The angle the sample fractured at makes it difficult to obtain a true edge on image, resulting in a larger measured n-CdS layer.

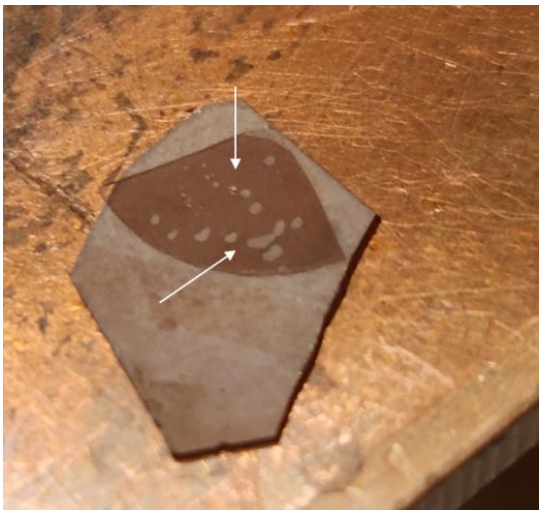

Figure 3.S10: Photo of p-GaP/n-CdS/Pt electrode after SPV measurements in forming gas.

3.7 References

1. D. M. Fabian, S. Hu, N. Singh, F. A. Houle, T. Hisatomi, K. Domen, F. E. Osterloh and S. Ardo, *Energ. & Envi. Sci.*, 2015, **8**, 2825-2850.
2. A. Kudo and Y. Miseki, *Chem. Soc. Rev.*, 2009, **38**, 253-278.
3. J. Jia, L. C. Seitz, J. D. Benck, Y. Huo, Y. Chen, J. W. D. Ng, T. Bilir, J. S. Harris and T. F. Jaramillo, *Nat. Commun.*, 2016, **7**, 13237.
4. A. M. K. Fehr, A. Agrawal, F. Mandani, C. L. Conrad, Q. Jiang, S. Y. Park, O. Alley, B. Li, S. Sidhik, I. Metcalf, C. Botello, J. L. Young, J. Even, J. C. Blancon, T. G. Deutsch, K. Zhu, S. Albrecht, F. M. Toma, M. Wong and A. D. Mohite, *Nat. Commun.*, 2023, **14**, 3797.
5. Q. Wang, T. Hisatomi, Y. Suzuki, Z. Pan, J. Seo, M. Katayama, T. Minegishi, H. Nishiyama, T. Takata, K. Seki, A. Kudo, T. Yamada and K. Domen, *Journal of the American Chemical Society*, 2017, **139**, 1675-1683.
6. T. Takata, J. Jiang, Y. Sakata, M. Nakabayashi, N. Shibata, V. Nandal, K. Seki, T. Hisatomi and K. Domen, *Nature*, 2020, **581**, 411-414.
7. S. Chen and L.-W. Wang, *Chemistry of Materials*, 2012, **24**, 3659-3666.
8. K. Sivula and R. van de Krol, *Nature Reviews Materials*, 2016, **1**, 15010.
9. P. Zhou, I. A. Navid, Y. Ma, Y. Xiao, P. Wang, Z. Ye, B. Zhou, K. Sun and Z. Mi, *Nature*, 2023, **613**, 66-70.
10. Y. B. Kuang, Q. X. Jia, G. J. Ma, T. Hisatomi, T. Minegishi, H. Nishiyama, M. Nakabayashi, N. Shibata, T. Yamada, A. Kudo and K. Domen, *Nature Energy*, 2017, **2**.
11. X. Shi, I. Y. Choi, K. Zhang, J. Kwon, D. Y. Kim, J. K. Lee, S. H. Oh, J. K. Kim and J. H. Park, *Nat. Commun.*, 2014, **5**, 4775.

12. Y. Pihosh, I. Turkevych, K. Mawatari, J. Uemura, Y. Kazoe, S. Kosar, K. Makita, T. Sugaya, T. Matsui, D. Fujita, M. Tosa, M. Kondo and T. Kitamori, *Scientific Reports*, 2015, **5**, 11141.

13. Y. Goto, T. Hisatomi, Q. Wang, T. Higashi, K. Ishikiriyama, T. Maeda, Y. Sakata, S. Okunaka, H. Tokudome, M. Katayama, S. Akiyama, H. Nishiyama, Y. Inoue, T. Takewaki, T. Setoyama, T. Minegishi, T. Takata, T. Yamada and K. Domen, *Joule*, 2018, **2**, 509-520.

14. H. Lyu, T. Hisatomi, Y. Goto, M. Yoshida, T. Higashi, M. Katayama, T. Takata, T. Minegishi, H. Nishiyama, T. Yamada, Y. Sakata, K. Asakura and K. Domen, *Chemical Science*, 2019, DOI: 10.1039/C8SC05757E.

15. O. Madelung, *Semiconductors: Data Handbook*, Springer, Berlin, 3rd edn., 2004.

16. K. Becker, C. Xiao, S. Assavachin, A. Kundmann and F. E. Osterloh, *J. Am. Chem. Soc.*, 2024, **146**, 7723-7733.

17. A. J. Nozik, *Applied Physics Letters*, 1976, **29**, 150-153.

18. A. Krawicz, D. Cedeno and G. F. Moore, *Physical Chemistry Chemical Physics*, 2014, **16**, 15818-15824.

19. M. Malizia, B. Seger, I. Chorkendorff and P. C. K. Vesborg, *J. Mater. Chem. A*, 2014, **2**, 6847-6853.

20. A. Standing, S. Assali, L. Gao, M. A. Verheijen, D. van Dam, Y. Cui, P. H. L. Notten, J. E. M. Haverkort and E. P. A. M. Bakkers, *Nat. Commun.*, 2015, **6**, 7824.

21. S. Lee, A. R. Bielinski, E. Fahrenkrug, N. P. Dasgupta and S. Maldonado, *ACS Appl. Mater. Interfaces*, 2016, **8**, 16178-16185.

22. S. Hu, M. R. Shaner, J. A. Beardslee, M. Lichterman, B. S. Brunschwig and N. S. Lewis, *Science*, 2014, **344**, 1005-1009.

23. Z. Xu, B. Hou, F. Zhao, S. Suo, Y. Liu, H. Shi, Z. Cai, C. L. Hill, D. G. Musaev, M. Mecklenburg, S. B. Cronin and T. Lian, *Journal of the American Chemical Society*, 2023, **145**, 2860-2869.

24. E. S. Brown, S. L. Peczonczyk, Z. Wang and S. Maldonado, *J. Phys. Chem. C*, 2014, **118**, 11593-11600.

25. F. D. Lin and S. W. Boettcher, *Nature Mater.*, 2014, **13**, 81-86.

26. M. R. Nellist, F. A. L. Laskowski, F. Lin, T. J. Mills and S. W. Boettcher, *Accounts of Chemical Research*, 2016, **49**, 733-740.

27. Y. Cheng, C. Xiao, B. Mahmoudi, R. Scheer, A. W. Maijenburg and F. E. Osterloh, *EES Catalysis*, 2023, **1**, 74-83.

28. S. Daemi, A. Kundmann, P. Cendula, K. Becker and F. E. Osterloh, *Energy Environ. Sci.*, 2023, **16**, 4530-4538.

29. F. A. L. Laskowski, S. Z. Oener, M. R. Nellist, A. M. Gordon, D. C. Bain, J. L. Fehrs and S. W. Boettcher, *Nature Mater.*, 2020, **19**, 69-76.

30. Z. Pan, J. A. Röhr, Z. Ye, Z. S. Fishman, Q. Zhu, X. Shen and S. Hu, *Sustainable Energy & Fuels*, 2019, **3**, 850-864.

31. A. J. Bard, A. B. Bocarsly, F. R. F. Fan, E. G. Walton and M. S. Wrighton, *Journal of the American Chemical Society*, 1980, **102**, 3671-3677.

32. Z. Pan, R. Yanagi, Q. Wang, X. Shen, Q. Zhu, Y. Xue, J. A. Röhr, T. Hisatomi, K. Domen and S. Hu, *Energ. & Environ. Sci.*, 2020, **13**, 162-173.

33. R. Han, M. A. Melo Jr, Z. Zhao, Z. Wu and F. E. Osterloh, *The Journal of Physical Chemistry C*, 2020, **124**, 9724-9733.

34. Y. Liu, N. Guijarro and K. Sivula, *Helvetica Chimica Acta*, 2020, **n/a**.

35. A. Kumar, P. G. Santangelo and N. S. Lewis, *Journal of Physical Chemistry*, 1992, **96**, 834-842.

36. S. Daemi, S. Kaushik, S. Das, T. W. Hamann and F. E. Osterloh, *J. Am. Chem. Soc.*, 2023, **145**, 25797-25805.

37. M. R. Nellist, F. A. L. Laskowski, J. Qiu, H. Hajibabaei, K. Sivula, T. W. Hamann and S. W. Boettcher, *Nature Energy*, 2018, **3**, 46-52.

38. Z. Zhao, E. J. Willard, J. R. Dominguez, Z. Wu and F. E. Osterloh, *Journal of Materials Chemistry A*, 2019, **7**, 18020-18029.

39. B. A. Wuille Bille, A. C. Kundmann, F. E. Osterloh and J. M. Velázquez, *Chem. Mater.*, 2022, **34**, 7553-7562.

40. R. Han, T.-Y. Kim, T. W. Hamann and F. E. Osterloh, *The Journal of Physical Chemistry C*, 2020, **124**, 26174-26183.

41. S. Y. Chae, S. J. Park, S. G. Han, H. Jung, C.-W. Kim, C. Jeong, O.-S. Joo, B. K. Min and Y. J. Hwang, *Journal of the American Chemical Society*, 2016, **138**, 15673-15681.

42. R. M. Doughty, F. A. Chowdhury, Z. Mi and F. E. Osterloh, *The Journal of Chemical Physics*, 2020, **153**, 144707.

43. J. Zhao, M. A. Holmes and F. E. Osterloh, *ACS Nano*, 2013, **7**, 4316–4325.

44. P. Nunez, M. Cabán-Acevedo, W. Yu, M. H. Richter, K. Kennedy, A. M. Villarino, B. S. Brunschwig and N. S. Lewis, *J. Phys. Chem. C*, 2021, **125**, 17660-17670.

45. L. Pan, J. H. Kim, M. T. Mayer, M.-K. Son, A. Ummadisingu, J. S. Lee, A. Hagfeldt, J. Luo and M. Grätzel, *Nature Catalysis*, 2018, DOI: 10.1038/s41929-018-0077-6.

46. P. Dai, W. Li, J. Xie, Y. He, J. Thorne, G. McMahon, J. Zhan and D. Wang, *Angew. Chem. Int. Ed.*, 2014, **53**, 13493-13497.

47. L. Gao, Y. Cui, R. H. J. Vervuurt, D. van Dam, R. P. J. van Veldhoven, J. P. Hofmann, A. A. Bol, J. E. M. Haverkort, P. H. L. Notten, E. P. A. M. Bakkers and E. J. M. Hensen, *Adv. Funct. Mater.*, 2016, **26**, 679-686.

48. M. Zhong, T. Hisatomi, Y. Kuang, J. Zhao, M. Liu, A. Iwase, Q. Jia, H. Nishiyama, T. Minegishi, M. Nakabayashi, N. Shibata, R. Niishiro, C. Katayama, H. Shibano, M. Katayama, A. Kudo, T. Yamada and K. Domen, *Journal of the American Chemical Society*, 2015, **137**, 5053-5060.

49. W. Vijselaar, P. P. Kunturu, T. Moehl, S. D. Tilley and J. Huskens, *ACS Energy Letters*, 2019, DOI: 10.1021/acsenergylett.9b01402, 2287-2294.

50. H. B. Michaelson, in *CRC Handbook of Chemistry and Physics*, ed. D. R. Lide, CRC Press/Taylor and Francis, Boca Raton, FL, 88 (Internet Version 2008) edn., 2008.

51. P. Vanysek, in *CRC Handbook of Chemistry and Physics*, CRC Press/Taylor and Francis, Boca Raton, FL, 88 (Internet Version 2008) edn., 2008.

52. Y. Yang, J. Gu, J. L. Young, E. M. Miller, J. A. Turner, N. R. Neale and M. C. Beard, *Science*, 2015, **350**, 1061-1065.

53. T. Uchihara, M. Matsumura, A. Yamamoto and H. Tsubomura, *Journal of Physical Chemistry*, 1989, **93**, 5870-5874.

54. T. Dittrich, *Materials concepts for solar cells*, Imperial College Press, London, 2015.

55. K. Maeda, K. Teramura, D. L. Lu, T. Takata, N. Saito, Y. Inoue and K. Domen, *Nature*, 2006, **440**, 295-295.

56. K. Maeda, K. Teramura, D. L. Lu, N. Saito, Y. Inoue and K. Domen, *Angew. Chem., Int. Ed. Engl.*, 2006, **45**, 7806-7809.

57. W. Sheng, H. A. Gasteiger and Y. Shao-Horn, *Journal of The Electrochemical Society*, 2010, **157**, B1529.

Chapter 4 – Photovoltage study of carbon nitride films

4.1 Abstract

Carbon nitride (CN) is a popular photocatalyst material, but its performance still remains much below its theoretical limit. This study explores the photovoltage (V_{ph}) of carbon nitride (CN) films prepared using different fabrication techniques and in different electrolytes. By employing surface photovoltage (SPV) measurements in combination with photoelectrochemical scans, we aim to characterize these films and identify the factors limiting their efficiency. We find that CN samples synthesized from melamine and deposited by doctor blading demonstrated the most consistent and durable results across different electrolyte solutions. The best performance was achieved in 0.1 M KOH with O_2 purging. This film reached 200 μA/cm^2 photocurrent at 1.23 V vs RHE and 1 sun illumination and a V_{ph}(SPV) of 1.1 V under 79 mW/cm^2 illumination from a 405 nm LED. The ability of CN to produce >1.0 V photovoltage in contact with aqueous electrolytes confirms its potential as a practical solar fuel photocatalyst.

4.2 Introduction

Carbon nitride (CN) is a cheap and nontoxic absorber for photoelectrochemical (PEC) cells due to its stability under harsh conditions and suitable band edge energies for OWS as shown in Fig 4.1b.[1,2] Graphitic CN (Fig. 4.1a) was first used for OWS in 2009, showing promise as environmentally friendly and earth abundant material for energy conversion.[3]

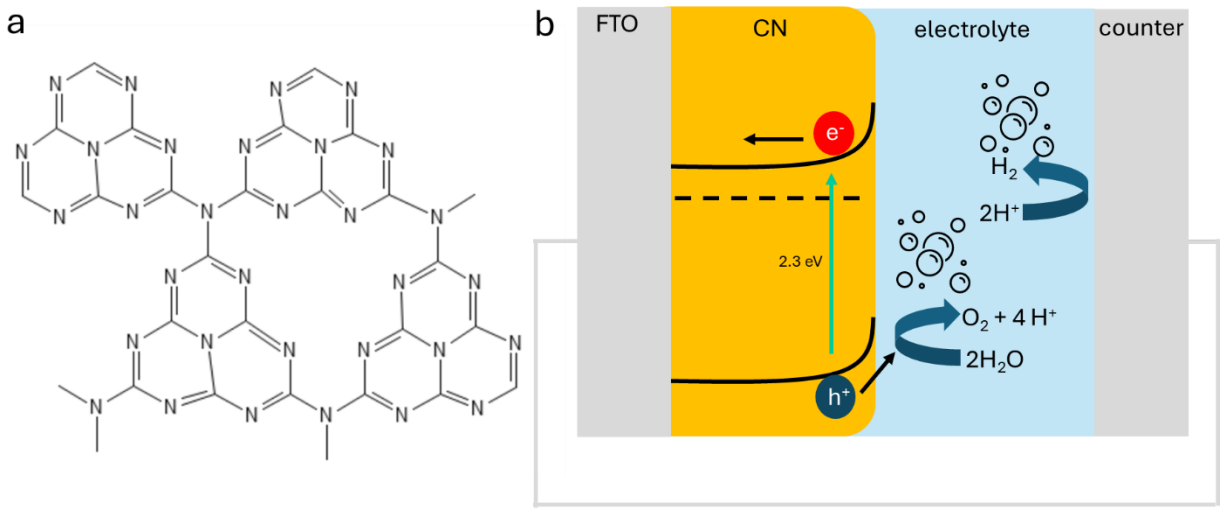

Figure 4.1 (a) layer structure of CN and (b) band diagram of CN anode under illumination where water oxidation occurs at the front contact and electrons are shuttled to the counter electrode to reduce protons.

However, the power conversion efficiency of CN is still low compared to the maximum theoretical value and lags behind other semiconductors.[4] Recently, the Menny Shalom group at Ben Gurion University in Israel showed that improved CN photoelectrodes could be achieved by dipping fluorine-doped tin oxide (FTO)-coated glass in a hot, saturated aqueous thiourea solution for 1 second, forming a uniform film whose thickness can be adjusted by repeated dipping. Calcining the thiourea films in the presence of melamine at 500 °C for 2 hours under nitrogen produces uniform yellow (CN) layers with tunable thickness (13-53 µm), based on SEM and XRD analyses. These CN films show a structured architecture with µm scale pores and exhibit a direct bandgap of 2.15–2.38 eV. In alkaline solution, the photocurrent at 1.23 V vs RHE increased from 270 to 350 µA/cm^2 and the incident photon to current efficiency (IPCE) value at 400 nm increased from 13 to 18%, with the addition of melamine to the fabrication process introducing surface modifications.[5] Doctor blading precursor pastes of melamine with various amounts of graphene

oxide (GO) in ethylene glycol were cast onto FT,. also improved performance. These films were calcined at 550 °C in N_2 for 4 h. At this temperature, melamine crystals condense into CN and GO is thermally reduced to rGO. Addition of rGO to the films raises the photocurrent (at 1.23 V vs RHE) from 80 to 120 μA/cm^2 and the IPCE value from 6 to 9 % at 400 nm. This enhancement is attributed to newly formed electronic paths introduced by the rGO leading to a larger electron diffusion length and better hole extraction efficiency.[6]

These findings are remarkable considering the defect rich structure of CN and its expected thermodynamic instability under water oxidation conditions. Here we employ surface photovoltage (SPV) spectroscopy and open circuit potential measurements in combination with photoelectrochemical scans to assess the photovoltage of these CN films. Generally, the power output of photoelectrochemical devices is determined by the photovoltage of the junction under illumination. For slow redox couples such as water oxidation, photovoltage measurements are not straightforward, due to the kinetic overpotentials during charge transfer. As described in Chapter 3, the photovoltage can be measured three different ways, from open circuit potential data, photoelectrochemical scans, and surface photovoltage data as shown in Fig. 4.2. All three methods will be used in the following to probe the photovoltage and open circuit potential under operating conditions (aqueous electrolytes and solar irradiance) and verify the photovoltage is sufficient for water oxidation.

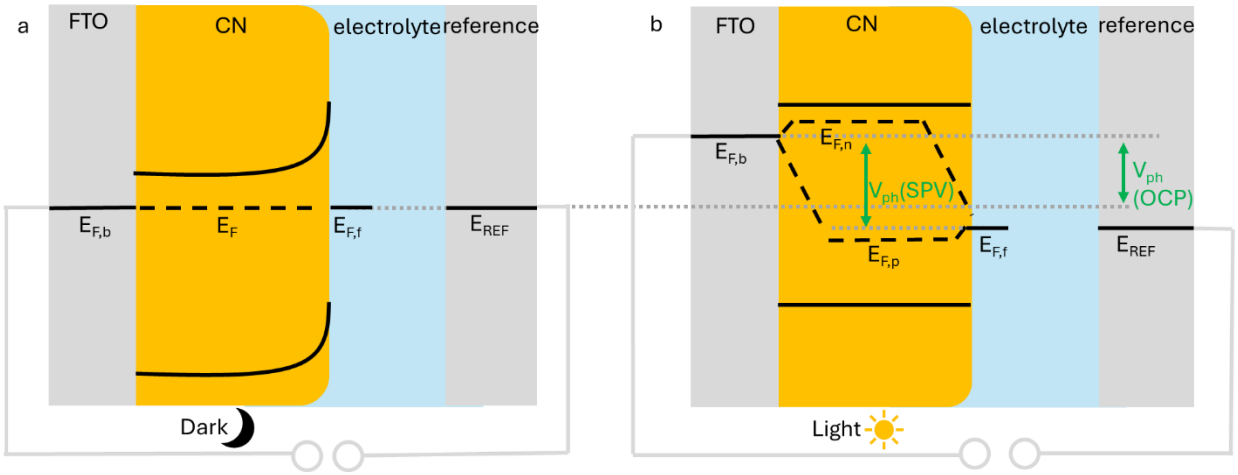

Figure 4.2 (a) At equilibrium in the dark so that $E_{F,b} = E_{F,f} = E_{REF}$. (b) Upon illumination the Fermi Levels split to produce the photovoltage. The unknown quasi-Fermi levels $E_{F,n}$ and $E_{F,p}$ are shown also.

Further, we aim to probe the defects in these CN films and also understand the effect of the electrolyte on the photovoltage. Specifically, sacrificial electron donors (TEAO) and acceptors (NaClO) are expected to modify the electrolyte Fermi level and the semiconductor-liquid junction. These influences will be probed in the following.

4.3 Results and Discussion

Carbon nitride films used for the study are summarized in Table 4.1 CN1 samples were made from thiourea alone and CN2 samples were made from a combination of thiourea and melamine.[5] Three samples were fabricated using the doctor blading method described by Peng and coworkers.[6] CN3 contains no rGO, but CN4 has rGO throughout the sample, and CN5 has a bottom layer containing rGO and a top layer of pure CN. Photos of CN1-5 are shown in Fig. 4.3 and optical properties summarized in Table 4.1.

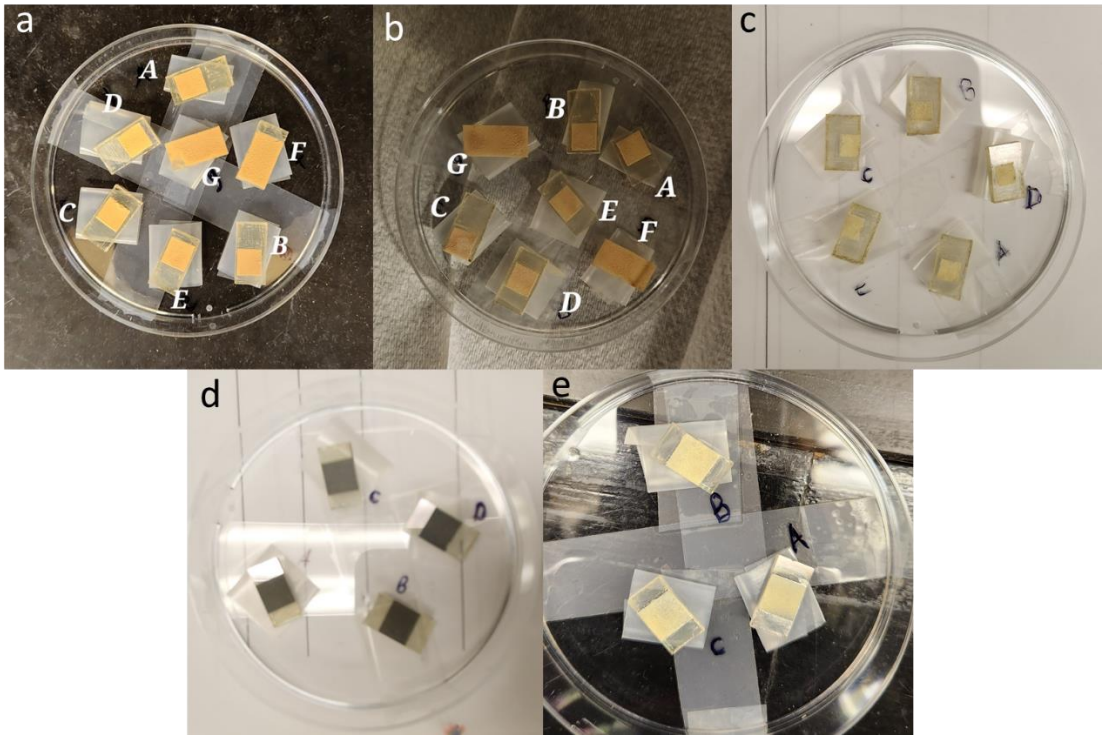

Figure 4.3 photos of CN films fabricated via (a) direct growth from thiourea, (b) direct growth from thiourea and melamine, (c) doctor blading from melamine, (d) doctor blading from melamine and rGO throughout, and (e) doctor blading from melamine and rGO bottom layer only.

Table 4.1 Summary of the CN samples and their measured properties.

Sample	Fabrication Method	Precursors	Sub Bandgap (eV)	Bandgap (eV)	Reference
CN1	Direct growth	thiourea	1.7	2.3	[5]
CN2	Direct growth	thiourea + melamine	1.6	2.3	[5]
CN3	Doctor blade	melamine	2.4	2.5	[6]
CN4	Doctor blade	melamine + GO	2.4	2.7	[6]
CN5	Doctor blade	melamine + GO	2.4	2.7	[6]

To probe the ability of the samples to generate a photovoltage V_{ph} under illumination, SPV SPV spectra for each film in vacuum were recorded (Fig. 4.4a). All samples generate a negative SPV signal (SPV = CPD(light) - CPD(dark)) upon illumination, in agreement with their n-type character. These findings are similar to earlier ones reported by the Osterloh group.[7,8] According to the earlier work, the sub band gap signal (yellow region) at 1.2 eV can be attributed to the excitation of defects in the materials, whereas the signal 2.4 - 2.7 eV (green region) is from band gap (2.3 eV) excitation. For CN1 and CN2 the sub band gap signal almost reaches 60% of the band gap SPV signal, suggesting large defect concentrations. For the other samples, this signal is less strong. CN1 and CN2 also have the strongest band gap SPV signal in the series, indicating improved photochemical charge separation. However, the large SPV values (in excess of the band

gap) and poor SPV reversibility indicates poor conductivity of the samples. The addition of rGO in CN4 and CN5 increases the SPV reversibility, likely by raising the conductivity of these films. A summary of the SPV results is shown in Table 4.2.

Table 4.2 CN films and their optical and photovoltage properties in vacuum.

Sample	Sub Bandgap (eV)	Bandgap (eV)	Max SPV (V)
CN1	1.2 [5]	2.4	-2.9
CN2	1.2	2.4	-3.5
CN3	1.2	2.5	-2.6
CN4	2.1	2.7	-1.2
CN5	1.8	2.5	-1.7

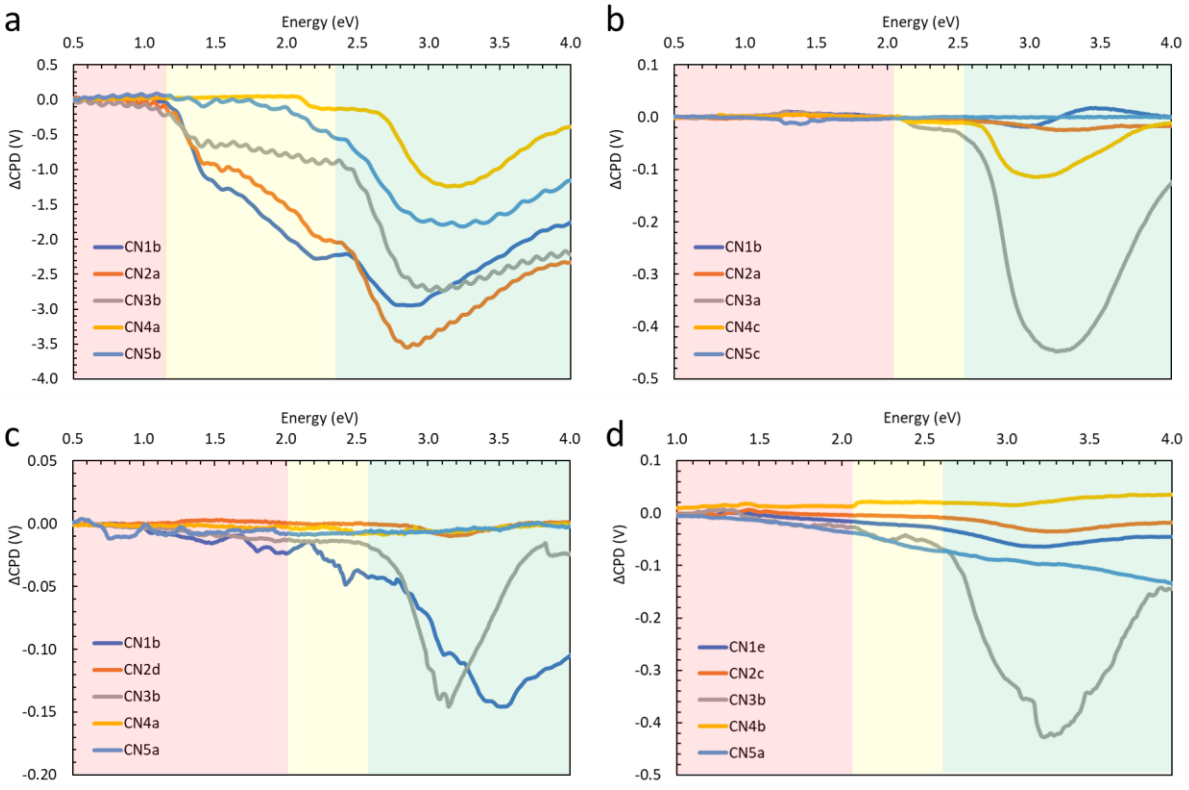

Figure 4.4 SPV spectra of CN films in (a) vacuum, (b) 0.1 M KOH (N_2), (c) 10% TEOA in 0.1 M KOH (N_2), and (d) 0.1 M NaClO in 0.1 M KOH (N_2). The colored regions indicate the baseline (red), sub-bandgap (yellow), and super-bandgap (green) excitation regions.

To simulate operational conditions, SPV spectra were repeated after immersing the films in aqueous electrolytes containing KOH, triethanolamine (TEOA) and sodium hypochlorite (NaClO). The redox potentials of these reagents relative to CN are summarized in Fig. 4.5. The reagents were selected because they are intermediates in water oxidation (O_2/H_2O) or they are commonly used a sacrificial electron donor (TEAO) during hydrogen evolution. NaClO, $NaIO_4$ and the $NaClO_2/NaClO_3$ couple were selected due to their strong oxidizing properties. We hypothesize these reagents can form depletion layers in CN and turn the CN-liquid contacts into strongly rectifying junctions for superior energy conversion.

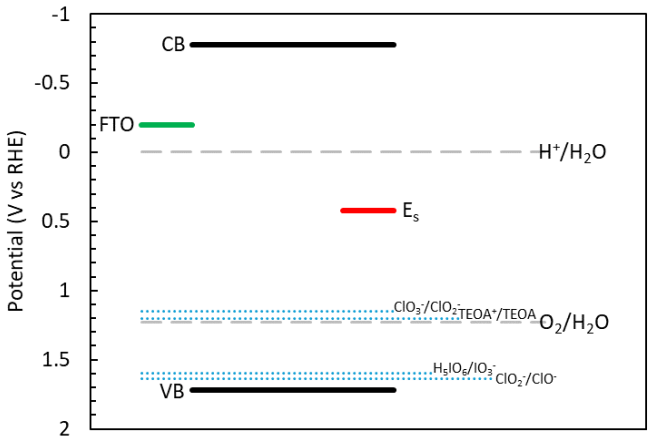

Figure 4.5 Proposed bandgap diagram of the CN3 photoanode on FTO. CB from Mott Schottky plot reported by Peng and coworkers.[6] VB calculated using bandgap from vacuum SPV and E_s from SPV onset.[9]

Spectra acquired in the various electrolytes are shown in Fig. 4.4b-d. It can be seen that the addition of electrolyte decreases the maximum ΔCPD. In 0.1 M aqueous KOH, CN3 reaches -0.44 V at 3.2 eV illumination, 17 % of the signal compared to vacuum. While CN4 only reaches -0.12 V and all other samples show virtually no photovoltage. In 10 % TEOA (ph 13.5), the maximum ΔCPD is reduced to -0.15 V for CN3 and -0.16 V for CN5. In 0.1 M NaClO (pH 13.1), CN3 gives a ΔCPD of -0.41 V and CN1 gives -0.06 V. All other samples gave no photovoltage. These decreases in signal compared to vacuum can be attributed to two main factors. Firstly, the spectra show a much reduced sub band gap signal from the passivation of surface states at the solid-liquid interface that may involve adsorption of H_2O or of ions to the CN. A schematic for this hypothesis is shown in Fig. 4.6. Second, several samples were found to detach from FTO after exposure to liquid, indicating poor contact with the substrate causing the small photovoltages.

These samples were excluded from the study as their durability would make multiple measurements difficult. The following investigations focus on CN3, named CN in the following.

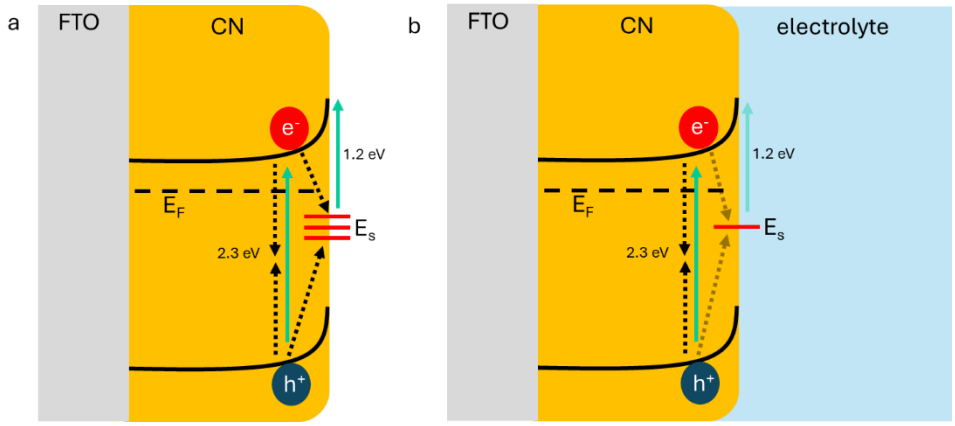

Figure 4.6 Band bending scheme for CN on FTO substrate upon illumination in (a) vacuum and (b) electrolyte. Solid arrows indicate light induced charge separation and dashed arrows indicate recombination.

The photoelectrochemical behavior of the CN electrode immersed in N_2 purged 0.1 M KOH (pH 12.8) is shown in Fig. 4.6. Selected measurement data is summarized in Table 4.3. According to the PEC scan in Fig. 4.6a, the CN electrode generates anodic photocurrents, reaching 80 µA/cm^2 at 1.23 V vs RHE under simulated 1 sun illumination (100 mW/cm^2). This is approximately three-quarters of the photocurrent achieved in a 0.1 M KOH electrolyte under AM 1.5G solar irradiance, as reported previously by Peng and coworkers.[6] Assuming the current is due to the oxygen evolution reaction (OER), the anodic photocurrent onset can be used to calculate a photovoltage V_{ph}(PEC) of 1.18 V.

Next, transient SPV was used to independently assess the photovoltage V_{ph}(SPV) under 405 nm illumination. At this energy, the photovoltage signal is entirely due to photocarriers in the

CN valence and conduction bands. The ΔCPD appears almost immediately upon light exposure (τ_{on} = 10 s) and rapidly returns to baseline when the light is turned off (τ_{off} = 46 s). The slower (τ_{off} is attributed to charge transfer via diffusion, while charge separation (τ_{on}) occurs through drift in the electric field within the depletion layer. The quick return to baseline indicates that the photochemical charge separation in this system is reversible and does not involve significant charge trapping. A turn on light intensity of 0.010 mW/cm^2 was needed for a ΔCPD to form, indicating that the recombination rate of photogenerated charge carriers is 2.0 × 10^{13} carriers/s·cm^2. At 47 mW/cm^2, the V_{ph}(SPV) reaches 530 mV, less than half of the photovoltage measured from PEC. This difference

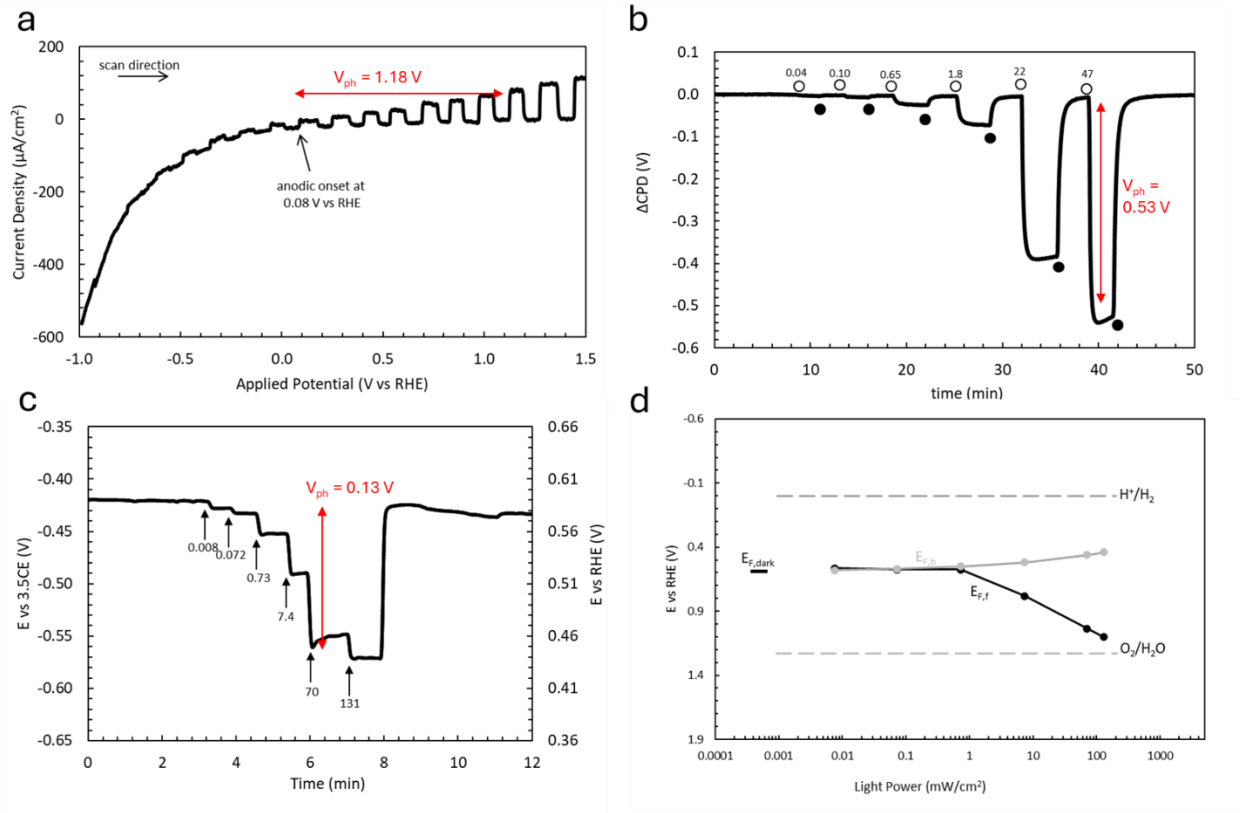

Figure 4.6 CN in 0.1 M KOH at pH 12.8 under N_2 flow. (a) Linear sweep voltammetry scans under chopped simulated 1 sun illumination and a scan rate of 20 mV/s. (b) SPV under intermittent illumination from 405 nm LED (irradiance in mW/cm^2). (c) Open circuit potential under intermittent illumination from 400 nm LED (irradiance in mW/cm^2). (d) Fermi level diagrams constructed by using the OCP as the $E_{F,b}$ and the max ΔCPD as the difference between $E_{F,b}$ and $E_{F,f}$.

Open-circuit potential (OCP) measurements were conducted for the CN film to obtain the electrochemical potential at the back side.[10] In the dark the OCP was 0.59 V vs RHE for the CN3 in 0.1 M KOH with N_2 purging. Because the water redox potential is not defined in the absence of O_2, this value is attributed to the energy of CN surface states. From Fig. 4.6 it can be seen that the ΔOCP increases with the light intensity, as expected according to the Shockley diode equation. Reference. Using the OCP values, combined with the light intensity dependent SPV, a Fermi level plot can be constructed (Fig. 4.6d). Because the change in OCP is small, the $E_{F,b}$ remains relatively constant while the $E_{F,f}$ moves to more oxidizing potential as the light intensity increases. It can be seen that $E_{F,f}$ does not reach the OER potential in 0.1 M KOH with N_2 purging. That means without applied potential a CN film immersed in water at basic pH is not able to generate O_2 through water oxidation.

Table 4.3: Summary of liquid SPV and electrochemistry results.

Electrolyte (gas)	pH	J @ 1.23 V under 1 sun (μA/cm^2)	V_{ph}(PEC) under 1 sun (mV)	R (e^-/cm^{2}s)	V_{ph}(SPV) under 405 nm (mV)	$E_{F,dark}$ (V vs RHE)	V_{ph}(OCP) under 400 nm (mV)

KOH (N_2)	12.8	80	1180	2.0×10^{13}	530	0.59	130
KOH (O_2)	12.8	200	830	$<1.0 \times 10^{13}$	1100	0.72	260
TEOA (N_2)	13.5	40	1220	$<8.1 \times 10^{12}$	520	0.72	610
ClO^- (N_2)	13.1	-	-	$<<1.4 \times 10^{13}$	700	0.76	-
ClO_2^-/ClO_3^- (N_2)	13.1	20	670	1.4×10^{13}	760	1.66	1200
IO_4^- (N_2)	13.2	-	-	$<1.4 \times 10^{13}$	540	1.06	530

From PEC theory it is well established that effective photoelectrodes require a depletion layer to form at the semiconductor liquid interface.[11] This requires the redox potential of the electrolyte to be more oxidizing than the flat band potential of the semiconductor. The absence of a discrete redox level in the electrolyte may have been responsible for the low photocurrents revealed for the CN electrode in H_2O in N_2 atmosphere. To check this hypothesis, measurements of CN3 in 0.1 M KOH were repeated in the presence of O_2 gas. The added O_2 establishes a discrete redox level in the electrolyte, at the O_2/H_2O standard reduction potential of 1.23 V. Redox PEC scans in this electrolyte are shown in Fig 4.7a. It can be seen that they yield anodic photocurrents, reaching up to 200 μA/cm^2 at 1.23 V vs RHE. This is 2.5× of the photocurrent achieved in N_2 (Fig. 4.6a). This shows that oxygen improves the CN-liquid junction. On the other hand, O_2 also induces a shift of the photocurrent onset to 0.40 V, more oxidizing potential (0.08 V), compared to N_2 atmosphere. It corresponds to a reduced photovoltage of 830 mV. Transient SPV shows a recombination rate of photogenerated charge carriers is less than 1.0×10^{13} carriers/s·cm^2 roughly half that compared to in N_2, At 79 mW/cm^2, the V_{ph}(SPV) reaches 1.1 V, double that of in N_2. The ΔCPD appears almost immediately upon light exposure, however, the return to baseline (τ_{off} = 300 s) is much slower. The slow return to baseline indicates that the photochemical charge

separation in this system involves significant trapping of photoholes, as required for water oxidation.

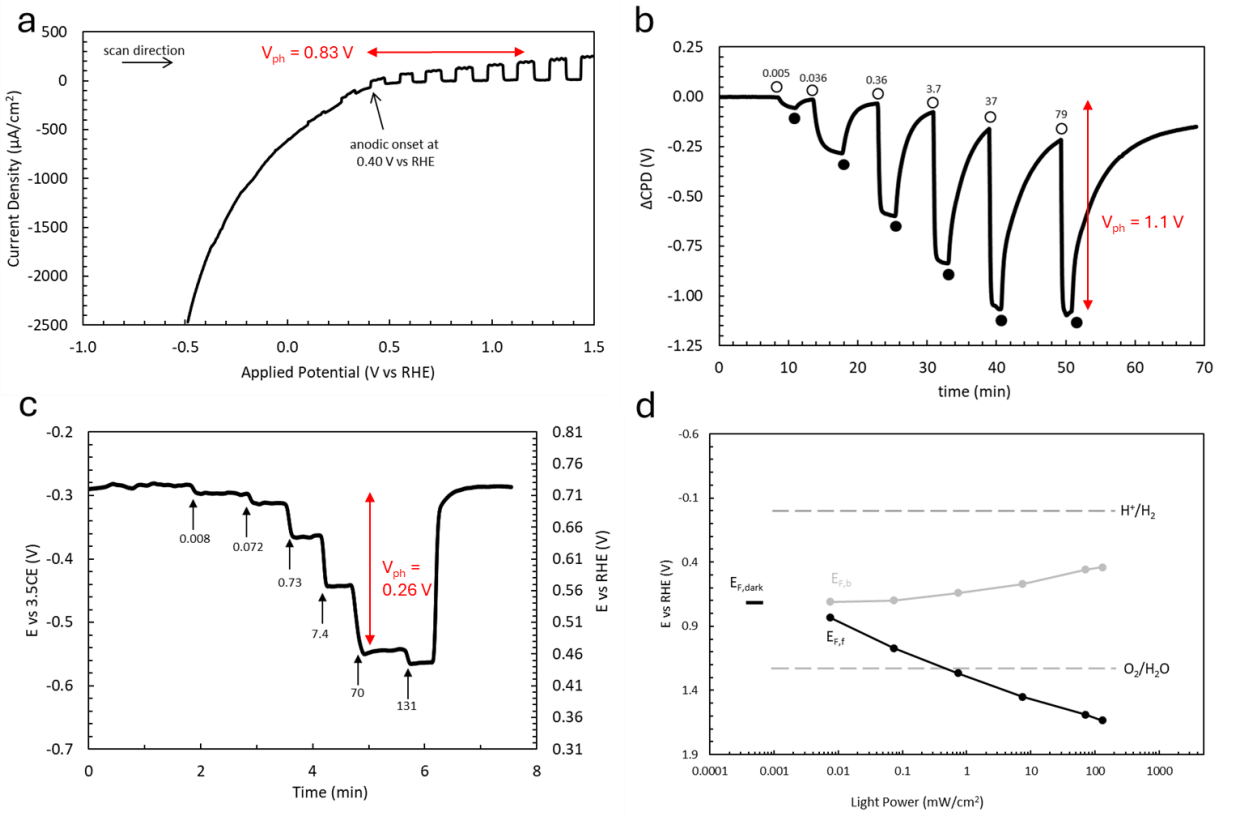

Figure 4.7 CN in 0.1 M KOH at pH 12.8 under O_2 flow. (a) Linear sweep voltammetry scans under chopped simulated 1 sun illumination and a scan rate of 20 mV/s. (b) SPV under intermittent illumination from 405 nm LED (irradiance in mW/cm^2). (c) Open circuit potential under intermittent illumination from 400 nm LED (irradiance in mW/cm^2). (d) Fermi level diagrams constructed by using the OCP as the $E_{F,b}$ and the max ΔCPD as the difference between $E_{F,b}$ and $E_{F,f}$.

OCP measurements (Fig 4.7c) reveal a $E_{f,dark}$ of 0.72, more oxidizing than in N_2 atmosphere. That shows the O_2 is accepting electrons from CN, forming a depletion layer. The ΔOCP reaches 270 mV, roughly double that of in N_2. This shows an improved photodiode behavior. After

combining the intensity dependent SPV and OCP results, the Fermi level diagram in Fig. 4.7d is obtained. It shows that illumination moves the $E_{F,b}$ to slightly more reducing values, as expected for a photoanode. Meanwhile the $E_{F,f}$ moves to more oxidizing values and reaching the water oxidation potential when the light intensity is above 0.5 mW/cm^2. That suggests that oxygen evolution should be possible thermodynamically in this system, in the presence of O_2 and an open circuit. This agrees well with the claim of water oxidation for CN electrodes under applied bias.[6]

Triethanolamine (TEOA) is a commonly used hole scavenger in the literature due to its electron transfer kinetics being much faster than for the OER.[2,12–14] This promotes hydrogen evolution.[12,15,16]It is added here to evaluate its effect on the photovoltage of CN films. The PEC scan for CN in contact with 10% (v/v) TEOA in aqueous KOH (Fig. 4.8a) shows the oxidation peak for TEOA at 1.3 V vs RHE and an increase in the dark current compared to KOH. A photocurrent density of 40 μA/cm^2 was achieved at 1.23 V. Using the tabulated E^0 of TEOA of 1.2 V, a photovoltage of 1.19 V was calculated from the measured photocurrent onset potential 0.01 V.[15] Transient SPV data are shown in Fig. 4.8b. At low light intensity, the timescale for τ_{on} and τ_{off} is on the order of minutes. This shows significant charge trapping and detrapping in surface states.[17] Additionally, at low light intensity the ΔCPD readily forms indicating less recombination at the solid-liquid junction. Above 0.36 mW/cm^2 the signal rises (τ_{on} = 10 s) and falls (τ_{off} = 20s) with complete reversibility, similar to KOH in N_2. The maximum SPV is 0.52 V at 79 mW/cm^2. This is comparable to the results in KOH (N_2). However, V_{ph}(SPV) is less than half of the V_{ph}(PEC), possible from the oxidation of $TEOA^+$ and its decomposition reactions. Finally, the OCP measurement gave $E_{F,dark}$ of 0.72 V vs RHE, slightly more oxidizing than in aqueous KOH. This might indicate that the TEAO absorbs to the CN surface. The Fermi level diagram is shown in Figure 4.8d. It is

characterized by large and non-uniform variations of $E_{F,b}$ that were not seen in KOH solution, and must be the result of the presence of TEAO. We speculate this is a result of the multistep oxidation chemistry of this reagent, which involves various radical intermediates.[17]These charged radicals built up at the CN surface and modify its electrochemical potential. At the highest light intensity, this allows the $E_{F,b}$ to reach the proton reduction potential. This agrees with the fact that TEOA boosts photocatalytic hydrogen evolution with CN.

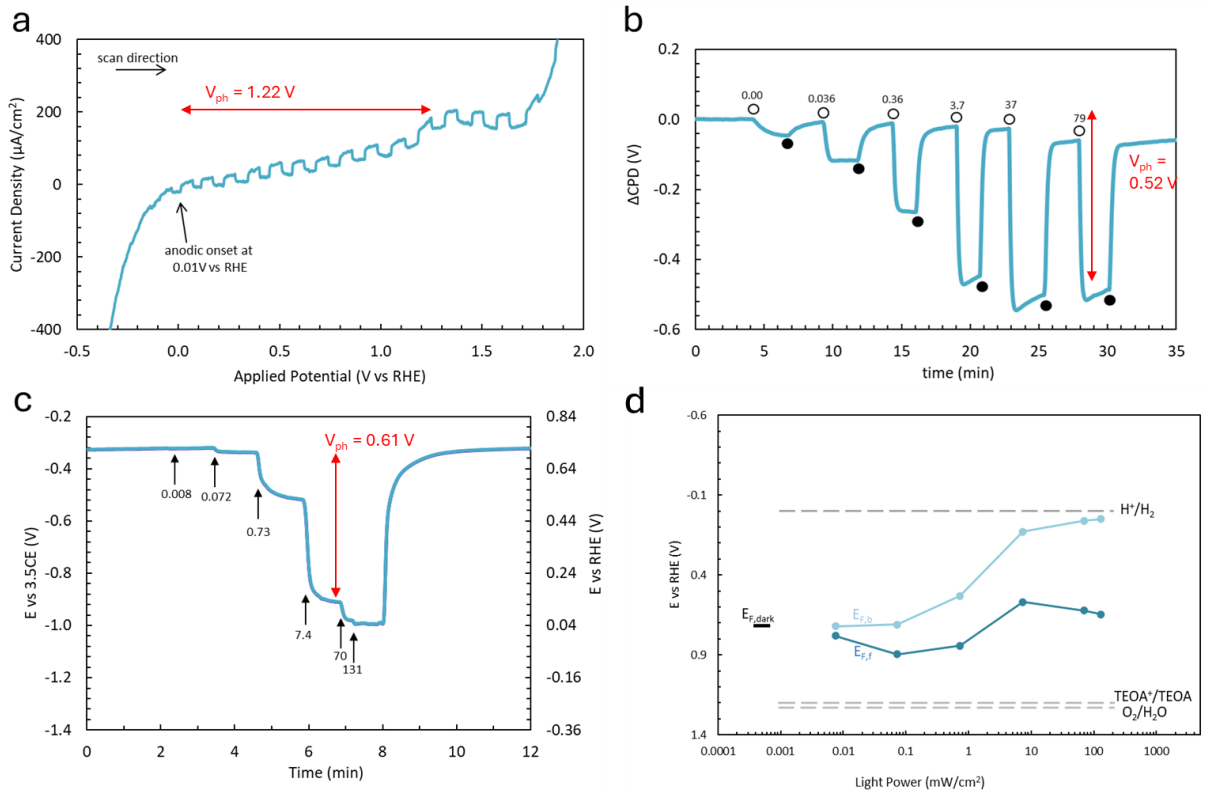

Figure 4.8 Photoelectrochemical behavior of FTO/CN electrodes exposed to 10 % (v/v) triethanolamine in aqueous KOH at pH 13.5 under N_2 flow. (a) Linear sweep voltammetry scans under chopped simulated 1 sun illumination and a scan rate of 20 mV/s (b) SPV under intermittent illumination from 405 nm LED (irradiance in mW/cm^2). (c) Open circuit potential under

intermittent illumination from 400 nm LED (irradiance in mW/cm^2). (d) Fermi level diagrams constructed by using the OCP as the $E_{F,b}$ and the max ΔCPD as the difference between $E_{F,b}$ and $E_{F,f}$.

Next, the PEC of CN in contact with a solution of 0.1 M NaClO in aqueous KOH was studied. Sodium hypochlorite is a known 2 electron oxidizing agent with an electrochemical potential of 1.48 V RHE.[9] This oxidizing potential is expected to induce a depletion layer in the n-CN film and generate a near ideal semiconductor-liquid junction. Photoelectrochemical scans with are shown in Fig. 4.9a. Interestingly, no photocurrent is seen for the CN3 film, only a strong a reduction current below ~0.4 V vs RHE. This potential is much more reducing that the standard reduction potential of common oxychlorite ions. Instead, as it is similar to the reduction current seen for CN electrodes in contact with O_2 containing electrolytes (Fig. 4.7), it is assigned to the reduction of O_2. The absence of a photocurrent suggests an ill-defined CN-liquid junction in this case. It is also possible that the reduction reaction kinetics of the ClO^-/Cl^- redox couple allow back electron transfer from the FTO substrate. This indicates a shunted photoelectrode. The OCP data in Fig. 4.9c agrees with this interpretation, as no photovoltage is observed even at the highest light intensities, and the potential at the backside remains unchanged. SPV scans in Fig. 4.9b show a different behavior. Large and reversible SPV signals are formed on the 140 s (τ_{on}) to 315 (τ_{off}) timescales, which reach up to 0.70 V under 52 mW/cm^2 illumination from the 405 nm LED. The ΔCPD readily forms at low light intensity indicating low recombination at the solid-liquid junction. The large SPV signals in combination with the absence of any changes in the open circuit potential indicates that all photochemical charge separation takes place at the CN-liquid interfaces and does not involve any electron transport to the FTO support. The corresponding Fermi level diagram is shown in Fig. 4.9d. It shows that while $E_{F,b}$ remains unchanged, the $E_{F,f}$ increases with

light intensity and eventually surpasses both the water oxidation potential and the hypochlorite oxidation potential. This is very similar to what is observed for the CN/KOH/O_2 system. It indicates that an illuminated CN electrode in NaClO solution should be able to evolve oxygen photocatalytically. No photocurrent is generated because of rapid back electron transfer from CN to OCl^-.

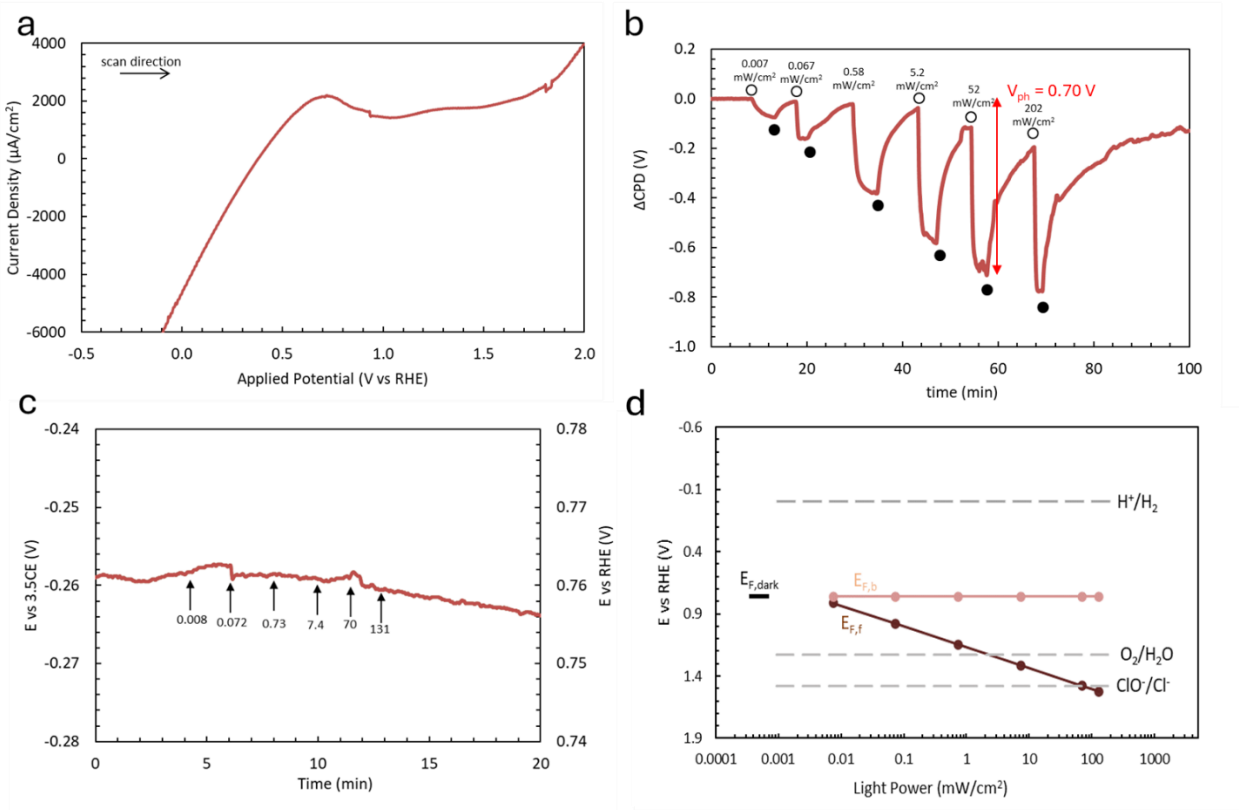

Figure 4.9 CN in a solution containing 0.1 M NaClO in aqueous KOH at pH 13.1 under N_2 flow. (a) Linear sweep voltammetry scans under chopped simulated 1 sun illumination and a scan rate of 20 mV/s. (b) SPV under intermittent illumination from 405 nm LED (irradiance in mW/cm^2). (c) Open circuit potential under intermittent illumination from 400 nm LED (irradiance in mW/cm^2).

(d) Fermi level diagrams constructed by using the OCP as the $E_{F,b}$ and the max ΔCPD as the difference between $E_{F,b}$ and $E_{F,f}$.

To further study the behavior of CN with strongly oxidizing electrolytes, that can induce a strong depletion layer in CN, experiments were repeated with an electrolyte containing 0.1 M $NaClO_2$ and 0.1 M $NaClO_3$ in aqueous KOH. The standard redox potential of this couple is 1.21 V vs RHE.[9] The data is shown in Figure 4.10. This time, PEC scans do yield a non-zero photocurrent density, but the current is fairly small (20 μA/cm^2 at 1.23 V). Assuming water oxidation is occurring, a photovoltage of 670 mV can be calculated from the photocurrent onset potential (0.56 V).

An SPV signal (Fig. 4.10b) is also readily formed and reaches up to 0.76 V at 52 mW/cm^2 LED illumination. Photovoltages from OCP (Fig. 4.10c) are even higher and reach up to 1.2 V at 70 mW/cm^2 illumination. Notably, the $E_{F,dark}$ (1.66 V vs RHE), is significantly higher in this system and clearly controlled by the standard reduction potential of the ClO_2^-/ClO^- redox couple (1.64 V). Under these conditions the CN is expected to be fully depleted and act as a photodiode. This is reflected in the Fermi level diagram in Figure 4.10d. It shows that under illumination, the $E_{F,b}$ can produce electrons at potentials significantly reducing relative to the redox level of the electrolyte. However, this potential remains below the proton reduction potential, meaning this CN film cannot generate H_2. The diagram also reveals a $E_{F,f}$ level that ends near the ClO_3^-/ClO_2^- and O_2/H_2O potentials. This shows that the electrode is able to oxidize chlorite ions (ClO_2^-) and evolve oxygen from water under strong illumination. Under weak illumination or in the dark, the CN Fermi level is controlled by charge transfer with the ClO_2^-/ClO^- redox couple instead. That characterizes the CN/ $ClO_3^-/ClO_2^-(H_2O)$ junction as a multi-redox photodiode.

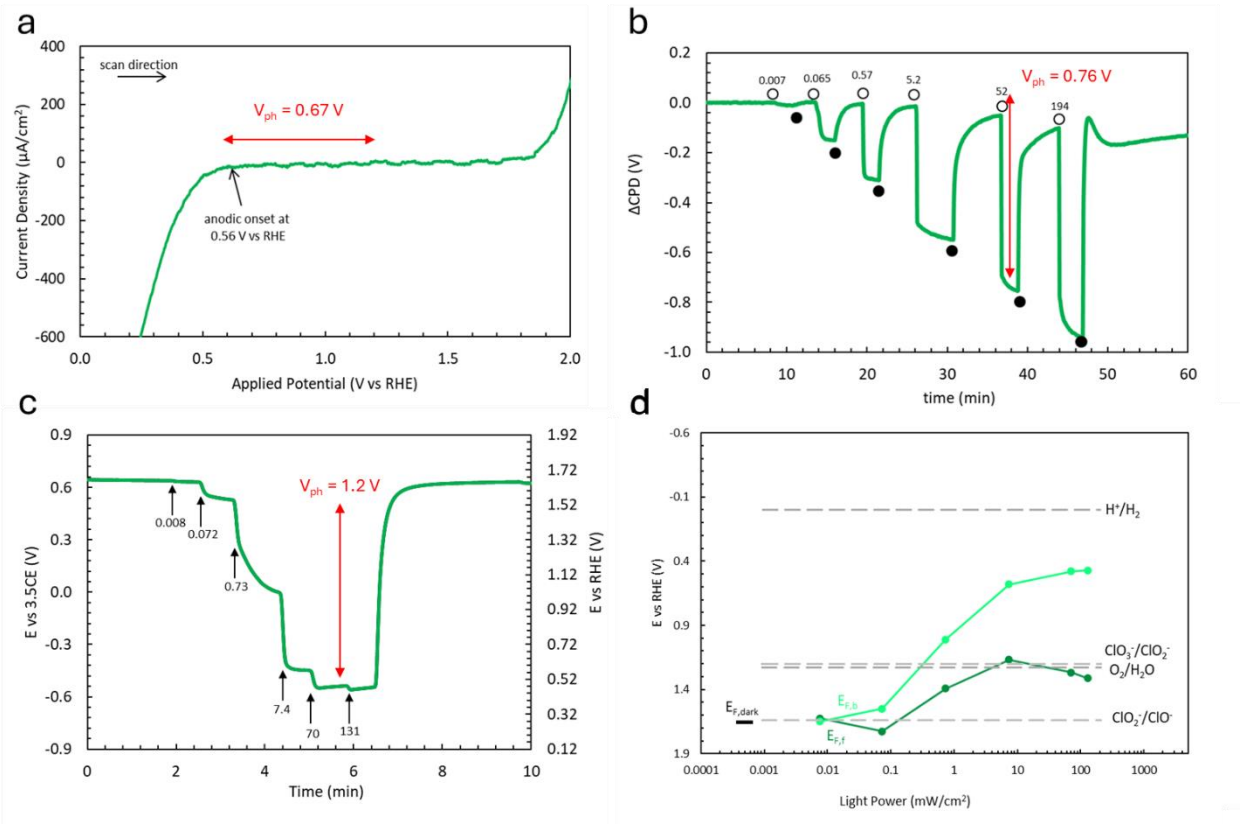

Figure 4.10 CN in a solution containing 0.1 M $NaClO_2$ and 0.1 M $NaClO_3$ in aqueous KOH at pH 13.1 under N_2 flow. (a) Linear sweep voltammetry scans under chopped simulated 1 sun illumination. (b) SPV under intermittent illumination from 405 nm LED (irradiance in mW/cm^2). (c) Open circuit potential under intermittent illumination from 400 nm LED (irradiance in mW/cm^2). (d) Fermi level diagrams constructed by using the OCP as the $E_{F,b}$ and the max ΔCPD as the difference between $E_{F,b}$ and $E_{F,f}$.

As the last redox couple capable of inducing strong depletion layer in CN, periodate was tested in KOH solution at pH = 13.2. The IO_4^-/IO_3^- couple has a potential of 1.6 V vs RHE.[9] Similar to what was seen with hypochlorite, the CN3 anode does not produce any photocurrent under AM 1.5 illumination (Fig. 4.11a). However, OCP data in Fig. 4.9c reveals a well behaved

photoanode capable of generating up to 550 mV photovoltage under 131 mW/cm^2 400 nm LED light. The SPV signal is unique, in that it contains spikes under most irradiance conditions. This shape suggests a fast charge transfer process followed by a slower one. The magnitude of the ΔCPD reaches 540 mV at 52 mW/cm^2, almost identical to the ΔOCP. Th results in a Fermi level diagram in Fig. 4.11d where $E_{F,f}$ remains constant near the potential for OER and the $E_{f,b}$ moves to more reducing values as light intensity gets stronger. This suggests that the CN electrode in IO_4^- is able to oxidize water to O_2 under even weak illumination conditions. However, because the IO_4^- reduction potential is more positive than the O_2/H_2O potential, the energy conversion efficiency under these conditions is zero. Tentatively, the saw-sooth shape in the SPV scans is due to the generation of O_2 at the CN surface, leading to temporary electrolyte displacement.

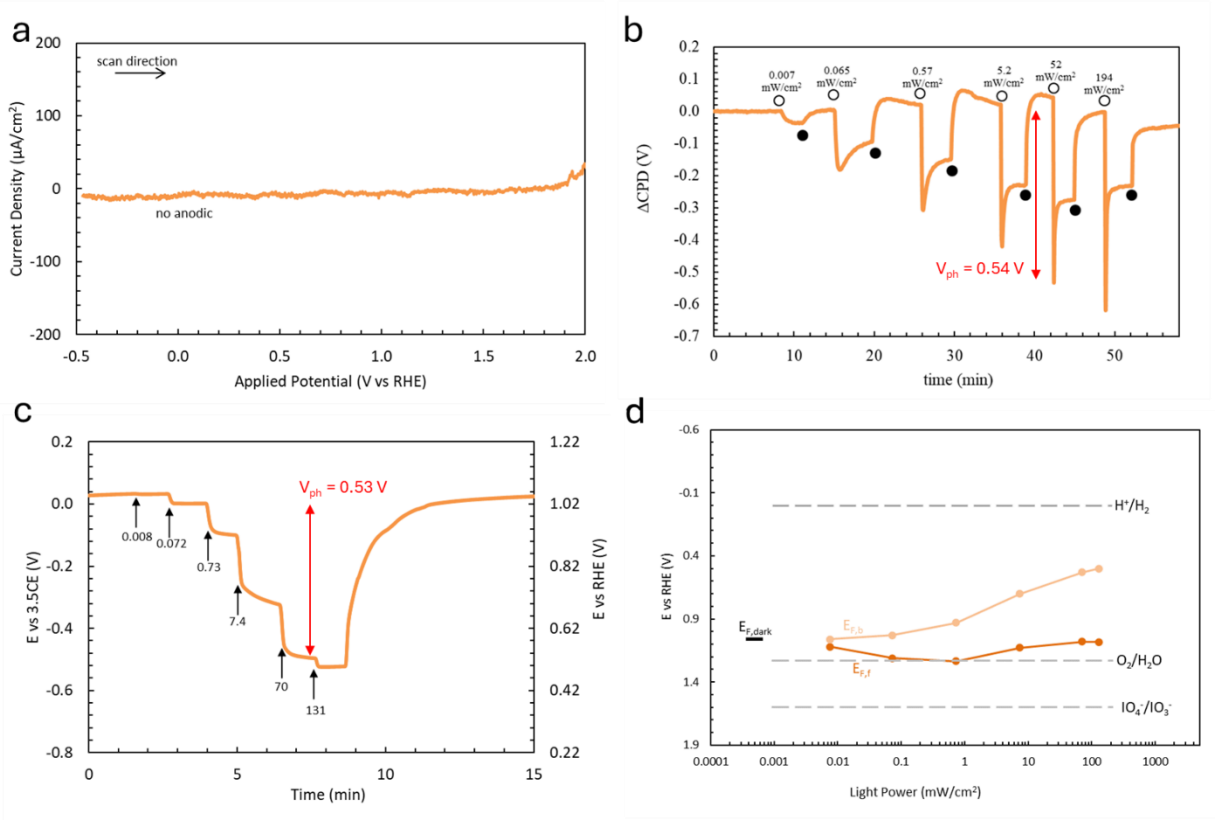

Figure 4.11: CN in a solution containing 0.1 M $NaIO_4$ in aqueous KOH at pH 13.2 under N_2 flow. (a) Linear sweep voltammetry scans under chopped simulated 1 sun illumination and a scan rate of 20 mV/s. (b) SPV under intermittent illumination from 405 nm LED (irradiance in mW/cm^2). (c) Open circuit potential under intermittent illumination from 400 nm LED (irradiance in mW/cm^2). (d) Fermi level diagrams constructed by using the OCP as the $E_{F,b}$ and the max ΔCPD as the difference between $E_{F,b}$ and $E_{F,f}$.

Lastly, to confirm the expected correlation between the photovoltage and the band bending in CN and to compare photovoltages from different methods, a plot of experimental $E_{F,dark}$ versus V_{ph} was constructed in Fig 4.12. The larger $E_{F,dark}$, the larger the expected band bending in CN. It can be seen that photovoltage values V_{Ph} from OCP, PEC, and SPV are quite different in size and in their dependence on $E_{F,dark}$. Only V_{ph}(OCP) shows the expected linear correlation with $E_{F,dark}$ and can be taken as a reliable indicator of the photovoltage. V_{ph}(PEC) values do not depend on the band bending, and thus are not a reliable indicator of V_{Ph} due to the measurement limitations, as discussed in chapter 3. The V_{ph}(SPV) values are found in-between V_{ph}(OCP) and V_{ph}(PEC). V_{ph}(SPV) is larger than V_{ph}(OCP) because SPV also factors in the change in the hole Fermi level $E_{F,front}$ to the photovoltage. This contribution is not captured by V_{ph}(OCP), which relies solely on the change of the fermi level $E_{F,back}$ of the majority carrier level at the back contact.

Combined, the V_{ph}(SPV) and V_{ph}(OCP) data provide a reasonable picture of how CN turns light energy into electrochemical energy. The lowest photovoltage is achieved in aqueous KOH in N_2 atmosphere because the band bending is insufficient to separate charge carriers at the CN-liquid interface. As a consequence, most charge carriers recombine. Higher photovoltage

becomes possible as the band bending increases after addition of O_2. Irradiation then produces considerable buildup of photoholes at the CN front contact based on the higher V_{ph}(SPV) signal. This allows water oxidation to proceed. Water oxidation also appears possible with $NaIO_4$ and with the $NaClO_3/NaClO_2$ redox couple. These oxidizing reagents maintain a strong band bending in CN, so that the carriers can separate efficiently. Based on its large V_{ph}(SPV) and V_{ph}(OCP) values at relatively small band bending (low $E_{F,dark}$ value), the CN/TEOA/H_2O junction is an exception to the trend. It is attributed to the formation of highly reducing radicals produced by the oxidative decomposition of TEOA. The decomposition is entirely irreversible and floods the electrode with electrons. Therefore, the observed photovoltage in this case is not a product or solar energy conversion with CN at all.

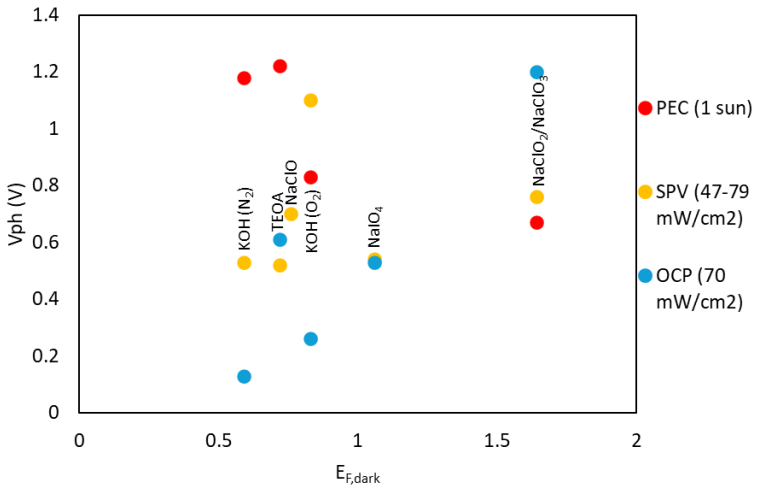

Figure 4.12: Plot of the photovoltage versus E_F(dark). E_F(dark) value were obtained from OCP measurements. Photovoltage values were obtained from PEC under simulated sunlight (100 mW/cm^2), from SPV under 405 nm LED illumination (47-79 mW/cm^2), or OCP under 400 nm LED illumination (70 mW/cm^2).

4.4 Conclusion

In summary we provide an assessment of the optical and photovoltage properties of carbon nitride samples. CN films prepared via doctor blading using melamine as the precursor are the most stable, allowing measurement of their photovoltage by several methods and in different electrolytes. The addition of the electrolyte improves the conductivity of the porous CN electrodes and controls their photovoltage. V_{ph}(SPV) values reach up to 1.1 V under 79 mW/cm^2 illumination from a 405 nm LED in 0.1 M aqueous KOH (O_2). This confirms that unbiased photochemical water oxidation is possible with carbon nitride. Under 1 sun illumination the material reaches a photocurrent of 200 μA/cm^2 at 1.23 V vs RHE. In contrast, no unbiased water oxidation is possible for a CN electrode immersed in aqueous KOH under N_2 atmosphere. This is because the band bending is not sufficient for charge separation. For most redox couples (O_2/H_2O, $TEOA^+$/TEOA, ClO^-/ClO_2^-), the $E_{F,dark}$ of CN appears to be pinned by surface states (0.7 V vs RHE), but ClO_2^-/ ClO_3^- and IO_4^- unpin the Fermi level. Future tests with both halves of the redox couples or use of applied potential SPV to investigate this hypothesis further. Those studies should also assess the effect of poor carrier mobility via front versus back illumination. The Shalom group has seen an enhancement of approximately 33 % in PEC for CN using back illumination.[5,6] To study the effect of back illumination in SPV will require modifications of the measurement setup.

4.5 Experimental

All C_3N_4 on FTO films were prepared by Sanjit Mondal at Ben-Gurion University of the Negev in the Menny Shalom Lab following previously published procedures.[5,6] Reagents:

Potassium hydroxide (Sigma-Aldrich, >85%), Triethanolamine (TEOA) (Fisher Scientific, >99%), sodium metaperiodate, sodium chlorite (Thermo, 80%), sodium chlorate (spectrum, technical), and sodium hypochlorite pentahydrate (TCL, 99%). For cleaning: Acetone (99.9%) and Ethanol (200 proof), water used to prepare solutions was purified to >16 MΩcm resistivity using a Nano-pure system.

Measurements: Measurements were done in duplicate on two separate samples. If the results differed, a third (or more) measurement was conducted. Representative data has been used in the above chapter and significant differences between identical samples is discussed.

SPV spectra and intensity dependent SPV data were obtained with the vibrating Kelvin probe technique, using a 60 % transparent 2.5 mm diameter Au Kelvin probe (Kelvin Probe S, Delta PHI Besocke) and a Besocke Kelvin Control unit. Measurements were conducted in a custom-made chamber under vacuum (≤ 1.6×10^{-3} mbar) or in continuous gas flow (wet N_2 or O_2) after >20 minutes of purging. Samples were coated with 10 µL of liquid electrolytes using a micropipette and covered with a glass cover slip (Fisher Scientific, 0.17 to 0.25 mm thickness). For the acquisition of full spectra, samples were illuminated through the Kelvin probe using light from a 300 W Xenon lamp filtered through an Oriel Cornerstone 130 monochromator (1-10 mW/cm^2). intensity is probably less, please check. Scans were performed from 3,390 cm^{-1} to 32,090 cm^{-1} by stepping the photon energy by 100 cm^{-1} each 5 s and by measuring the contact potential difference (CPD) value at each step. Depending on the wavelength, and an average intensity of 2.5 mW/cm^2 in the 2.0 eV–3.6 eV interval. The contact potential difference data were corrected for drift effects by subtracting a fitted logarithmic curve of a dark scan from the spectral scan

resulting in the ΔCPD results presented. In spectral figures, red region is baseline, yellow region is sub bandgap excitation, and green region is super bandgap excitation.

Intensity-dependent measurements were performed with an air-cooled 4 cell 405 nm LED array connected to a DC power supply not exceeding 1.20 A. The voltage was regulated to produce 0.005 to 202 mW/cm^2 at the sample surface, as measured by a photometer equipped with a GaAsP UV-Vis detector (International Light Technologies, Inc), and after correction using a 60% transmission value for the Kelvin probe. The contact potential difference data were corrected for drift effects by subtracting a fitted logarithmic curve of a dark scan.

Photoelectrochemical measurements were conducted in a three-electrode set up with a Pt counter electrode and a 3.5 M calomel reference electrode (3.5CE) connected via 3 M KCl salt bridge. The CN working electrode had excess FTO substrate masked with polyester tape and was connected via a stainless-steel alligator clip. The exposed area was measured using imageJ software to calculate the current density. The solution and enclosed head space was purged with N_2 gas or O_2 gas to remove air for >15 min. The potential was calibrated versus RHE using $Fe(CN)_6^{3-}$ /$Fe(CN)_6^{4-}$ at +0.358 V vs. RHE. A Xe lamp was used as the light source and the distance was adjusted to have an intensity of 100 mW/cm^2 (1 sun) at the working electrode.

Open circuit potential (OCP) measurements were performed in a two-electrode set up with a 3.5 M calomel reference electrode (3.5CE) connected via 3 M KCl salt bridge. The CN working electrode was prepared as described above. Illumination came from an air cooled 400 nm LED with power regulated between 0.008 mW/cm^2 and 131 mW/cm^2. Several light on/off cycles were used to determine the true fermi level in the dark once it stabilized.

4.6 References

(1) Li, X.; Xiong, J.; Gao, X.; Huang, J.; Feng, Z.; Chen, Z.; Zhu, Y. Recent Advances in 3D G-C_3N_4 Composite Photocatalysts for Photocatalytic Water Splitting, Degradation of Pollutants and CO_2 Reduction. *J. Alloys Compd.* **2019**, *802*, 196–209. https://doi.org/10.1016/j.jallcom.2019.06.185.

(2) Xiong, W.; Huang, F.; Zhang, R. Q. Recent Developments in Carbon Nitride Based Films for Photoelectrochemical Water Splitting. *Sustain. Energy Fuels* **2020**, *4* (2), 485–503. https://doi.org/10.1039/c9se00785g.

(3) Wang, X.; Maeda, K.; Thomas, A.; Takanabe, K.; Xin, G.; Carlsson, J. M.; Domen, K.; Antonietti, M. A Metal-Free Polymeric Photocatalyst for Hydrogen Production from Water under Visible Light. *Nat. Mater.* **2009**, *8* (1), 76–80. https://doi.org/10.1038/nmat2317.

(4) Wang, Q.; Hisatomi, T.; Jia, Q.; Tokudome, H.; Zhong, M.; Wang, C.; Pan, Z.; Takata, T.; Nakabayashi, M.; Shibata, N.; Li, Y.; Sharp, I. D.; Kudo, A.; Yamada, T.; Domen, K. Scalable Water Splitting on Particulate Photocatalyst Sheets with a Solar-to-Hydrogen Energy Conversion Efficiency Exceeding 1%. *Nat. Mater.* **2016**, *15* (6), 611–615. https://doi.org/10.1038/nmat4589.

(5) Qin, J.; Barrio, J.; Peng, G.; Tzadikov, J.; Abisdris, L.; Volokh, M.; Shalom, M. Direct Growth of Uniform Carbon Nitride Layers with Extended Optical Absorption towards Efficient Water-Splitting Photoanodes. *Nat. Commun.* **2020**, *11* (1), 1–9. https://doi.org/10.1038/s41467-020-18535-0.

(6) Peng, G.; Qin, J.; Volokh, M.; Liu, C.; Shalom, M. Graphene Oxide in Carbon Nitride: From Easily Processed Precursors to a Composite Material with Enhanced Photoelectrochemical Activity and Long-Term Stability. *J. Mater. Chem. A* **2019**, *7* (19), 11718–11723. https://doi.org/10.1039/c9ta02880c.

(7) Wu, P.; Wang, J.; Zhao, J.; Guo, L.; Osterloh, F. E. Structure Defects in G-C_3N_4 Limit Visible Light Driven Hydrogen Evolution and Photovoltage. *J. Mater. Chem. A* **2014**, *2* (47), 20338–20344. https://doi.org/10.1039/c4ta04100c.

(8) Wu, P.; Wang, J.; Zhao, J.; Guo, L.; Osterloh, F. E. High Alkalinity Boosts Visible Light Driven H_2 Evolution Activity of G-C3N4 in Aqueous Methanol. *Chem. Commun.* **2014**, *50* (98), 15521–15524. https://doi.org/10.1039/c4cc08063g.

(9) Vanysek, P. Electrochemical Series. *Comput. Sci. Commun. Dict.* **2000**, 489–489. https://doi.org/10.1007/1-4020-0613-6_5901.

(10) Memming, R. *Semiconductor Electrochemistry*; 2015. https://doi.org/10.1002/9783527688685.ch7.

(11) Gerischer, H. Electrochemical Photo and Solar Cells Principles and Some Experiments. *J. Electroanal. Chem.* **1975**, *58* (1), 263–274. https://doi.org/10.1016/S0022-0728(75)80359-7.

(12) Hua, S.; Qu, D.; An, L.; Jiang, W.; Wen, Y.; Wang, X.; Sun, Z. Highly Efficient P-Type Cu3P/n-Type g-C_3N_4 Photocatalyst through Z-Scheme Charge Transfer Route. *Appl. Catal. B Environ.* **2019**, *240* (September 2018), 253–261.

https://doi.org/10.1016/j.apcatb.2018.09.010.

(13) Yang, J.; Wang, D.; Han, H.; Li, C. Roles of Cocatalysts in Photocatalysis and Photoelectrocatalysis. *Acc. Chem. Res.* **2013**, *46* (8), 1900–1909. https://doi.org/10.1021/ar300227e.

(14) Ng, B. J.; Putri, L. K.; Kong, X. Y.; Teh, Y. W.; Pasbakhsh, P.; Chai, S. P. Z-Scheme Photocatalytic Systems for Solar Water Splitting. *Adv. Sci.* **2020**, *7* (7). https://doi.org/10.1002/advs.201903171.

(15) Zhu, Q.; Xu, Z.; Qiu, B.; Xing, M.; Zhang, J. Emerging Cocatalysts on G-C_3N_4 for Photocatalytic Hydrogen Evolution. *Small* **2021**, *17* (40), 1–25. https://doi.org/10.1002/smll.202101070.

(16) Ran, J.; Zhang, J.; Yu, J.; Jaroniec, M.; Qiao, S. Z. Earth-Abundant Cocatalysts for Semiconductor-Based Photocatalytic Water Splitting. *Chem. Soc. Rev.* **2014**, *43* (22), 7787–7812. https://doi.org/10.1039/c3cs60425j.

(17) Savateev, O.; Zou, Y. Identification of the Structure of Triethanolamine Oxygenation Products in Carbon Nitride Photocatalysis. *ChemistryOpen* **2022**, *11* (7). https://doi.org/10.1002/open.202200095.